AFGL-TR-82-0041

COHERENCE BANDWIDTH AND PULSE DISTORTION THROUGH NATURALLY AND ARTIFICIALLY MODIFIED IONOSPHERES

K. C. Yeh and C. H. Liu

Department of Electrical Engineering
University of Illinois at Urbana-Champaign
Urbana, Illinois 61801

August 1982

Final Report
October 16, 1978 through August 15, 1982

Approved for public release; distribution unlimited.

AIR FORCE GEOPHYSICS LABORATORY
AIR FORCE SYSTEMS COMMAND
UNITED STATES AIR FORCE
HANSCOM AFB, MASSACHUSETTS 01731

Unclassified

SECURITY CLASSIFICATION OF THIS PAGE (When Data Entered)

REPORT DOCUMENTATION PAGE		READ INSTRUCTIONS BEFORE COMPLETING FORM
1. REPORT NUMBER AFGL-TR-82-0041	2. GOVT ACCESSION NO. AD-A123864	3. RECIPIENT'S CATALOG NUMBER
4. TITLE (and Subtitle) Coherence Bandwidth and Pulse Distortion Through Naturally and Artificially Modified Ionospheres		5. TYPE OF REPORT & PERIOD COVERED Final Report Oct. 16, 1978 - Aug. 15, 1982 6. PERFORMING ORG. REPORT NUMBER TR No. 68, UILU-ENG-82-2549
7. AUTHOR(s) K. C. Yeh and C. H. Liu		8. CONTRACT OR GRANT NUMBER(s) F19628-78-C-0195
9. PERFORMING ORGANIZATION NAME AND ADDRESS Department of Electrical Engineering University of Illinois at Urbana-Champaign Urbana, Illinois 61801		10. PROGRAM ELEMENT, PROJECT, TASK AREA & WORK UNIT NUMBERS 63431F 464305AA
11. CONTROLLING OFFICE NAME AND ADDRESS Air Force Geophysics Laboratory (PHP) Hanscom AFB, Massachusetts 01731 Monitor/Herbert E. Whitney/PHP		12. REPORT DATE August 1982 13. NUMBER OF PAGES 180
14. MONITORING AGENCY NAME & ADDRESS(if different from Controlling Office)		15. SECURITY CLASS. (of this report) Unclassified 15a. DECLASSIFICATION/DOWNGRADING SCHEDULE

16. DISTRIBUTION STATEMENT (of this Report)

Approved for public release; distribution unlimited

17. DISTRIBUTION STATEMENT (of the abstract entered in Block 20, if different from Report)

18. SUPPLEMENTARY NOTES

Contract F19628-78-C-0195 is supported under Project 2029 by Hq. Space Division, YKX, Los Angeles, CA 90009.

19. KEY WORDS (Continue on reverse side if necessary and identify by block number)

Transionospheric radio propagation
Ionospheric scintillation
Pulse propagation and distortion
Ionospheric bubbles
Parabolic equation
Ionospheric irregularities

20. ABSTRACT (Continue on reverse side if necessary and identify by block number)

This project is concerned with the study of propagation of radio signals through a perturbed ionosphere. The problems investigated can be broadly classified into three areas: propagation effects through ionospheric bubbles, propagation effects through ionospheric irregularities and experimental observations of scintillation effects. Four-year work on these areas is summarized in this report.

DD FORM 1 JAN 73 1473 EDITION OF 1 NOV 65 IS OBSOLETE

Unclassified

SECURITY CLASSIFICATION OF THIS PAGE (When Data Entered)

Table of Contents

Coherence Bandwidth and Pulse Distortion through Naturally Occurring and Artificially Modified Ionosphere

1. Introduction

A contract with the above title was awarded to the University of Illinois to commence the investigations on July 16, 1978. This contract has since been extended twice to July 15, 1982. Therefore, in this final report we will summarize our work for a period of four years.

This project is concerned with the study of propagation of radio signals through a perturbed ionosphere. These ionospheric perturbations can be naturally occurring, probably caused by some plasma instability mechanisms; they can also be man-made, for example, by high power transmitters, chemical releases or nuclear detonations in the atmosphere. We are not concerned in this project with the exact physical mechanisms that produce these perturbations although investigations into these mechanisms are interesting research problems by themselves. What is concerned in this project are effects these ionospheric perturbations may have on radio signals propagating through them. In general, these perturbations are highly complicated and imprecisely known. We must then use whatever information that is available to model these perturbations either deterministically or stochastically. Such a modeling effort will depend on the interplay of experimental observations and theoretical suggestions and deductions. With accumulation of experimental data the models can be made more accurate. Of course better ionospheric models will enable us to simulate more closely the true propagation conditions.

2. Summary of Problems Investigated and Results

The problems investigated under the support of this project can be broadly classified into three areas: propagation effects through ionospheric bubbles, propagation effects through ionospheric irregularities and experimental observations of scintillation effects. These are described in the following.

2.1 Propagation Effects through Ionospheric Bubbles

One of the most intensely perturbed ionospheric regions by natural events is the region above the magnetic equator. Various observations have shown that large depletions in ionization, often called bubbles, are possible. Inside these bubbles, the ionization structure is extremely complex and have been variously described as ionization walls and protruding fingers. As far as their effects to radio propagation is concerned, the important realization is the fact that the ionization gradients can be very steep, much steeper than expected based on the usual random medium hypothesis. Because of this we cannot use the random medium approach to wave propagation studies; instead we must first model this bubble medium deterministically and then study the propagation effects through such a deterministic medium. The complexity of the bubble structure renders any analytical approach hopeless and the only recourse is then to use a numerical approach. Several problems have been investigated using this approach. We summarize our results briefly below.

To start the investigation through an ionospheric bubble we need to do two things: (1) A bubble model and (2) A numerical scheme in solving the wave equation. These two things are done in a report

(see section 4, publication 7). The bubble model is constructed using the in-situ data and numerical calculations based on plasma instabilities. The wave equation is converted into a parabolic equation under forward scatter approximation, which is then solved numerically by an implicit method generalized from the Crank-Nicholson scheme. Some preliminary results are also given in this report. These results obtained from additional computations are presented in a paper (see section 4, publication 3). Among other effects, these numerical computations show that the sharp wedgelike structures associated with bubbles may be responsible to scintillation outbursts at GHz frequencies that are not predicted by any statistical scintillation theory. Apparently, sharp gradients in electron density variations affect the field distributions in ways quite different from the way in which uniformly disturbed irregularities do. The effects seem to be most distinct at GHz frequencies.

Nuclear explosions in the atmosphere are known to create violent perturbations in the ionosphere. It is thus of interest to investigate the effects such violent ionospheric perturbations may have on waves propagating through them. Based on information accumulated in the open literature the gross ionospheric features after the nuclear explosion are known, but for wave propagation studies we need to have fine structures down to scales of ten meters or less. Since such fine details are unavailable it was suggested to us to use the equatorial bubble data as a basis for construction of a model. The horizontal structure is unchanged; it is still based on the in situ data. However, the important modifications have been made in two aspects: the vertical extent of the bubble and the vertical correlation distance of the spiky structures. To accomplish both of these aspects we have

effectively superposed three bubbles on top of each other. In this model, the background ionosphere has a maximum electron density of 2.8×10^{11} electrons/m^2 and an electron content value of 8.9×10^{16} electrons/m^2, corresponding to a slab thickness of 320 km. Superposed on this background ionosphere is a region of depleted electron densities with maximum depletion equal to 6.7×10^{16} electrons/m^2. Inside the depleted region there exist sharp gradients that have vertical correlation distances equal to 50 km to 100 km. Numerical computations show amplitude scintillations to be appreciable at 4 GHz (S_4=0.26) and clearly discernible even at a frequency as high as 15 GHz (S_4=0.0025). The dominating component of the phase fluctuation has its origin in the variation of the optical path which has the inverse frequency dependence. The phase departure from the optical path has a rough f^{-2} dependence. At 4 GHz, the standard deviation of phase departure is 0.09π radians or 16 degrees. These results and additional details have been published (see section 4, publication 6).

In a separate investigation we have also carried out computations that indicate how a pulse would distort while propagating through this bubble medium. To do this, the pulse is Fourier decomposed into discrete frequency components. The parabolic equation is then solved for each component, which recombines at the receiver location to form a pulse. The results are described in a thesis (see section 4, publication 10). Since it is attached as Appendix B, we shall not repeat it here.

2.2 Propagation Effects through Ionospheric Irregularities

Under the support of this project we have also worked on several problems using the random medium approach. These are described in the following.

When a pulse propagates through the random medium, the pulse is expected to be broadened. In general two distinct mechanisms may be responsible for the broadening of a temporal pulse. In the first mechanism the pulse arriving at the receiver essentially perserves its shape, but the arrival time fluctuates from realization to realization. This fluctuation in arrival time may be caused by pulse wandering. One can envision the presence of large irregularities which may be responsible for the pulse to travel along a different path and hence wander as a function of time as the irregularities move through the propagation path. In the second mechanism the pulse may be broadened due to scattering, especially multiple scattering. In this case each arriving pulse is spread, resulting in an broadened average pulse. To distinguish these two pulse broadening processes: wandering and spreading, one needs to work with four-frequency mutual coherence function, Γ_4. The equation for Γ_4 is derived and solved for two special cases in a paper (see section 4, publication 1). The results show that pulse wandering is the important mechanism under weak scattering conditions and pulse spreading is the important mechanism under the strong scattering conditions.

The arrival time of a radio pulse as observed by a fixed observer can be defined by the first temporal moment or the "time centroid" of the pulse. When this concept is applied to wave propagation in a random medium, the pulse arrival time becomes a random variable and will fluctuate about some mean value, giving rise to the phenomenon commonly called pulse jitters. It is then of interest to investigate the statistical properties of this pulse jitter, which can be done by using the multifrequency mutual coherence functions. This problem is

the subject of a paper (see section 4, publication 2) where, among other things, the statistical moments for the pulse arrival time are derived in the fully saturated regime. Under this extreme limit, the mean arrival time can exceed the free space time delay by an appreciable value. At the same time, calculations indicate that fluctuations about the mean arrival time are very small when compared with the excess time delay. This suggests that the excess delay time is caused mainly by pulse spreading and not by pulse wandering, in agreement with calculations carried out in publication 1 (see section 4).

In applications it has been found convenient to describe the pulse by its beginning several temporal moments. Using such an approach, the zeroth moment is related to the total energy in the pulse, the first moment is related to the mean arrival time, the second moment is related to the mean square pulse width, the third moment is related to the skewness of the pulse and the fourth moment is related to the kurtosis of the pulse. For propagation in an ionosphere expressions for these five moments have been derived (see section 4, publications 4 and 9). In addition to the physical significance of these temporal moments, they can also be applied to digital communications. An ideal pulse in such a case may become distorted and stretched owing to propagation effects. When the pulsewidth is stretched to occupy an interval longer than one communication bit inter-symbol interference is expected. Using the temporal moments an upper bound of the energy content outside of one chip can be estimated. Readers interested in details should consult the original publications, one of which is attached as Appendix A.

2.3 Experimental Observations of Scintillation Effects

In addition to theoretical investigations of the scintillation problems we have also collected some experimental data for evaluation.

Earlier multifrequency scintillation data received at various stations around the globe by SRI International have been analyzed and the results have been reported in our Scientific Report No. 2 (see section 4, publication 8). These early results will not be repeated here. More lately a joint effort was made in collecting scintillation data at Ascension Island. These more recent data have been partially analyzed and some of the results are reported here.

In the course of analyzing the GHz scintillation data from Ascension Island, it became clear to us that there exist time shifts up to one second or so between similar fades of the L- and C-band signals. Initial efforts were concentrated on eliminating possible causes of equipment origin. Several possibilities were considered and finally with the test tape provided to us by AFGL, it was concluded that the shifts are real physical phenomenon rather than the artifact of the data recording process. The data have been analyzed and a physical model has been proposed to interprete the phenomenon. The results have been written up as a paper to be published in Geophysical Research Letters (see section 4, publication 6). It is also included as Appendix C.

The Ascension Island data are still being analyzed. We report their preliminary findings in the following.

Statistics of Multi-Frequency Scintillation Signals

The UHF, L- and C-band data from Marisat collected at Ascension Island provide us with multi-frequency data to study the statistical behavior of the signals. Segments of these multi-frequency data were selected for detailed analysis. Fig. 1 shows such an example where scintillation indices (S_4) for every minute are presented for L- and

C-band signals during a ten hour period on Jan. 27, 1981. Five segments of data with varying degrees of scintillation activities were chosen to study the power spectra, the frequency dependence of S_4, and the coherence time of the scintillating signals.

Multifrequency Power Spectra of Intensity Scintillation

In Figs. 2-8, spectra for UHF, L-band and C-band scintillation signals are presented for seven cases. In all cases, the UHF scintillations were saturated while the C-band scintillations varied from very weak to moderate. The L-band scintillations varied from strong to saturation. The spectrum for weak C-band scintillation (Fig. 2) follows the prediction of weak scintillation theory: a flat low frequency part followed by a roll-off at the fresnel frequency with a high frequency asymptote sloping at ν=p-1, where p is the power index of the three dimensional power-law spectrum of the form κ^{-p} for the irregularities. The spectra for strong scintillations at UHF or L-band are quite different from that for the weak scintillation case. In general, the spectra are broadened with the roll-off frequency pushed further to the high frequency end. There is also evidence that the low frequency part of the spectrum is enhanced. Table 1 summarizes the important features of the spectra for the seven cases.

It is interesting to note that the slopes of the high frequency asymptotes are consistently higher than most of the previously measured values.

Frequency Dependence of S_4

If we assume the frequency dependence of the scintillation index to be of the form

Table 1

	case	S_4	ν	Other features
	UHF	9.6	4.5	Broadening, low frequency enhancement
I	L	.35	4	
	C	.08	4	
	UHF	.98	6	B, LFE
II	L	.77	6	B
	C	.13	6	
	UHF	1.1	6	B, LFE
III	L	.94	6.5	B
	C	.15	6.5	
	UHF	1.0	6	B, LFE
IV	L	.92	6	B
	C	.17	5.5	
	UHF	.95	6.5	B, LFE
V	L	.96	6	
	C	.18	6	
	UHF	1.0	6	B, LFE
VI	L	1.1	6	B, LFE
	C	.24	6	
	UHF	1.1	5.5	B, LFE
VII	L	1.0	5.5	B, LFE
	C	.31	5	B, LFE

$$S_4 \propto f^{-n} \tag{1}$$

then the spectral index n can be computed from the data. Between L- and C-bands signal,

$$n = -2.45 \log \frac{S_4(C)}{S_4(L)} \tag{2}$$

Figs. 9 and 10 show two cases of the spectral index n plotted as a function of the scintillation index of C-band signal. We note that n remains approximately constant for $S_4(C)<0.2$, predicted by the weak scintillation theory. As the scintillation gets stronger, n decreases due to the saturation effects on the L-band signal. This manifestation of the multiple scattering effect is more apparent when one computes the spectral index between UHF and C-band signals.

According to the weak scintillation theory, the spectral index n is related to the power index p of the irregularity spectrum by

$$n = \frac{p+2}{4} \tag{3}$$

Therefore, it is possible to deduce the power index p from the scintillation indices of L- and C-bands,

$$p = 4n-2 = -9.8 \log \frac{S_4(C)}{S_4(L)} - 2 \tag{4}$$

Figure 11 shows a plot of spectral index n as a function of time for the event on the 27th of January (Figure 1). From the six hours of data, we selected those periods when $S_4(C)$ was between 0.05 and 0.25 for computing n such that the weak scintillation theory may be valid. We note the definite trend of increasing value of n after midnight indicating the steepening of the irregularity power spectrum. This

may correspond to the dissipation of the small size irregularities after midnight. The values of n and hence p from these computations may be somewhat lower than the real values for the irregularities since some saturation effects may already be important in the L-band signal even though only weak C-band signals have been chosen in the computation.

Since the power index p of the irregularity spectrum can be obtained from the slope ν of the high frequency asymptote of the intensity power spectrum as well as the spectral index n for the frequency dependence of S_4, it is interesting to compare the estimated values of p from both methods. Table II shows such a comparison.

Table II

Data Set	$S_4(C)/S_4(L)$	n	p	$\nu(L)$	$\nu(C)$	p
Jan. 26 2135-2240	.15/.70	1.64	4.56	4.34	4.8	5.34-5.8
Jan. 26 2310-2400	.09/.47	1.76	5.04	5.0	4.9	6-5.9
Jan. 27 2125-2152	.15/.67	1.59	4.36	4.2	4.1	5.2-5.1
Jan. 30 2213-2258	.17/.85	1.71	4.84	5.6	5.4	6.6-6.4

The values used in the Table are averaged values for the whole period of each data set. We note that the p values estimated from the high frequency slopes of the power spectra are consistently higher than the p values obtained from the spectral index n. This as explained above, may be due to the fact that L-band scintillations were too strong for weak scintillation theory to be valid.

Coherence time of the UHF signal and the strength of scintillation

In strong scintillation theory when the multiple scattering effects are important, it is known that the signal becomes decorrelated, resulting in decreasing coherence time. Indeed, when the scintillation is well into the saturation regime, the S_4 index is no longer an accurate measure of the strength of scintillation. On the other hand, the signal coherence time becomes a good indicator of how strong the irregular structures are. Figure 12 demonstrates this point as we compare the coherence time τ_c of the UHF signal against the S_4 index of the C-band signal. We note that the decrease of τ_s tracks well the increase of $S_4(C)$ and vice versa.

3. Conclusion

We have investigated three aspects of the scintillation problem in this project. They are: propagation effects through ionospheric bubbles, propagation effects through ionospheric irregularities and experimental observations of scintillation effects. In the first aspect the propagation medium is simulated by using in-situ data obtained while traversing an ionospheric bubble. These bubbles have been observed to have highly complex structures with very steep gradients. Because of the peculiar nature of the bubble medium a deterministic approach rather a stochastic approach to solving the wave equation is used. The results show scintillation bursts especially at GHz frequencies when the ray paths intersect the sharp gradient. These calculations are further extended to a simulated ionosphere under nuclear perturbations. Severe scintillations at frequencies as high as 15 GHz are possible.

In the second aspect we are mainly concerned with the temporal behavior of radio signals. In this vein we have investigated the statistics of the pulse arrival time (commonly called pulse jitters), the pulsewidth and their effects to digital communication. Even though our study is theoretical in nature, its results have applications to satellite based communication and navigation.

The third aspect of this project is concerned with investigations of scintillation effects on transionospheric experimental data. The experimental data re recordings made at various ground stations of radio transmissions from the orbiting DNA Wideband and also recordings made at Ascension Island during a special campaign. Both sets of data are of high quality, digitized on magnetic tape for computer processing. These data possess multi-channels on several frequencies and phase

coherence so that both amplitude and phase fluctuations can be studied. The results show agreement with theoretical expectations and also some new phenomena which require explanation that only additional investigations and experimentations can provide.

4. Publications

4.1 Journal and Symposium Articles

1. C. H. Liu and K. C. Yeh, Pulse spreading and wandering in random media. Radio Sci., 14(5), 925-931, 1979.

2. C. H. Liu and K. C. Yeh, Statistics of pulse arrival time in turbulent media. J. Opt. Soc. Am., 70(2), 168-172, 1980.

3. A. W. Wernik, C. H. Liu and K. C. Yeh, Model computations of radio wave scintillation caused by equatorial ionospheric bubbles. Radio Sci., 15(3), 559-572, 1980.

4. C. C. Yang and K. C. Yeh, Temporal behavior of pulses after propagating through a turbulent ionosphere. In "Effect of the ionosphere on radiowave systems" edited by John M. Goodman, pp.525-533, U.S. Government Printing Office, Washington, D.C., 1981.

5. K. C. Yeh and C. H. Liu, Simulated propagation effects on trans-ionospheric radio waves. In "Effect of the ionosphere on radio-wave systems" edited by John M. Goodman, pp.591-598, U.S. Government Printing Office, Washington, D.C., 1981.

6. S. Franke, J. Austen, A. W. Wernik and C. H. Liu, Systematic refraction caused by equatorial plasma bubbles observed in micro-wave scintillations. To appear in Geophys. Res. Letters, 1982.

4.2 Scientific Reports

7. A. W. Wernik, Model computations of radio wave scintillation caused by equatorial bubbles. Scientific Report No. 1, AFGL-TR-79-0165, July 1979.

8. S. B. Quinn, Jr., Studies of transionospheric scintillations using orbiting satellite data. Scientific Report No. 2, AFGL-TR-80-0092, April 1980.

4.3 Theses

9. C. C. Yang, Temporal behavior of pulses after propagating through a turbulent ionosphere. M.S. thesis, 1981. Attached as Appendix A.

10. M. R. Tucker, A deterministic study of pulse propagation in an electron bubble medium. M.S. thesis, 1981. Attached as Appendix B.

Figure Captions

Figure 1. Example of L-band (a) and C-band (b) scintillation data.

Figure 2. Intensity power spectrum for UHF, L-band and C-band signal--Case I.

Figure 3. Intensity power spectra for UHF, L-band and C-band signal--Case II.

Figure 4. Intensity power spectra for UHF, L-band and C-band signal--Case III.

Figure 5. Intensity power spectra for UHF, L-band and C-band signal--Case IV.

Figure 6. Intensity power spectra for UHF, L-band and C-band signal--Case V.

Figure 7. Intensity power spectra for UHF, L-band and C-band signal--Case VI.

Figure 8. Intensity power spectra for UHF, L-band and C-band signal--Case VII.

Figure 9. Spectral index n computed from L- and C-band data.

Figure 10. Spectral index n computed from L- and C-band data.

Figure 11. Evolution of the spectral index n as a function of time during the event on January 27, 1981.

Figure 12. (a) Coherence time for UHF signal (b) Simultaneous scintillation index for C-band signal.

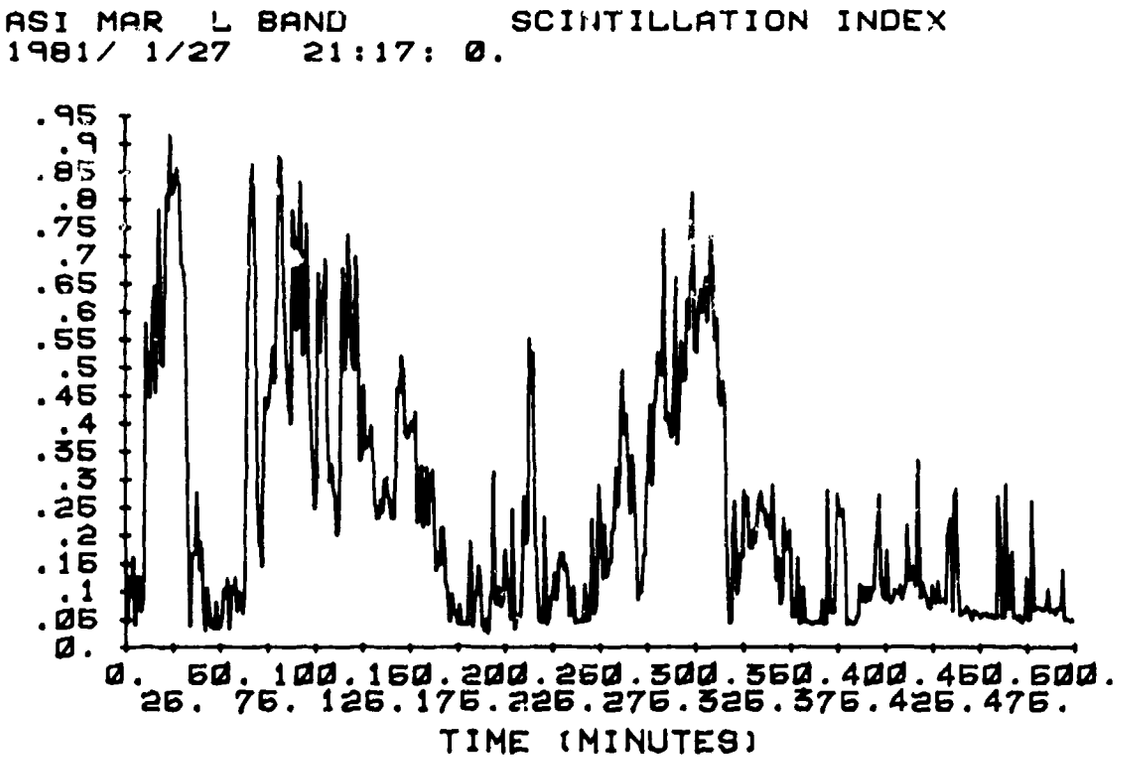

Figure 1A

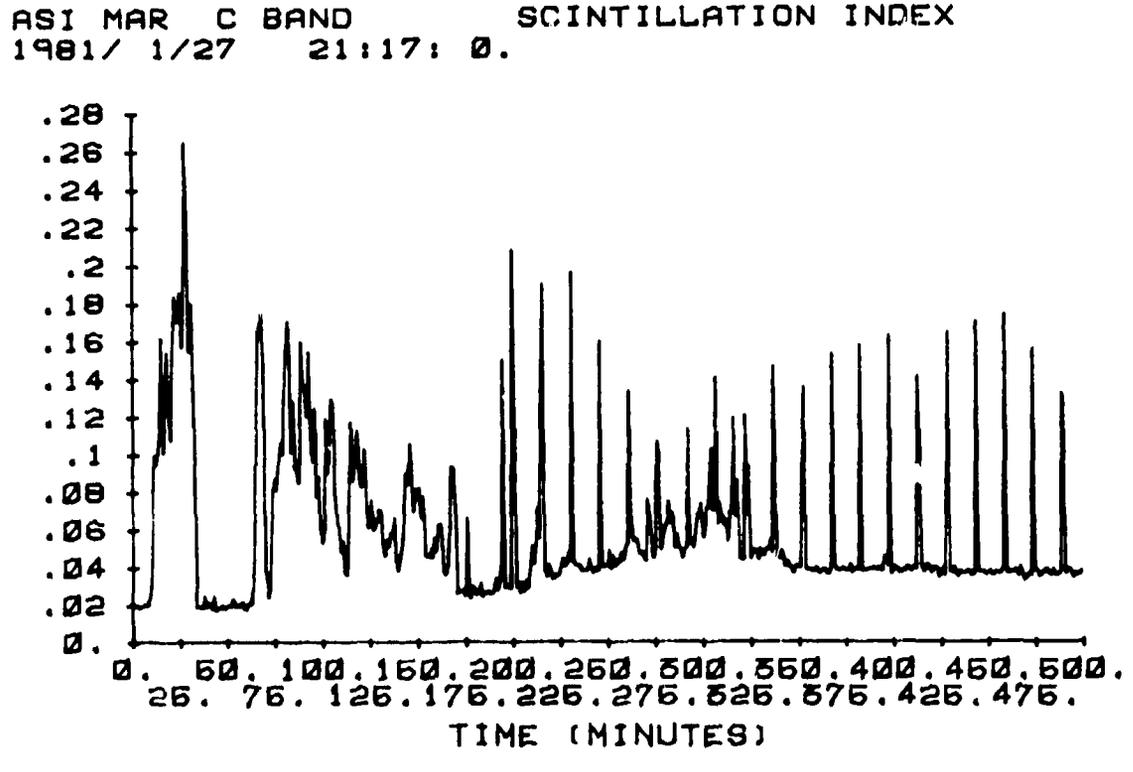

Figure 1B

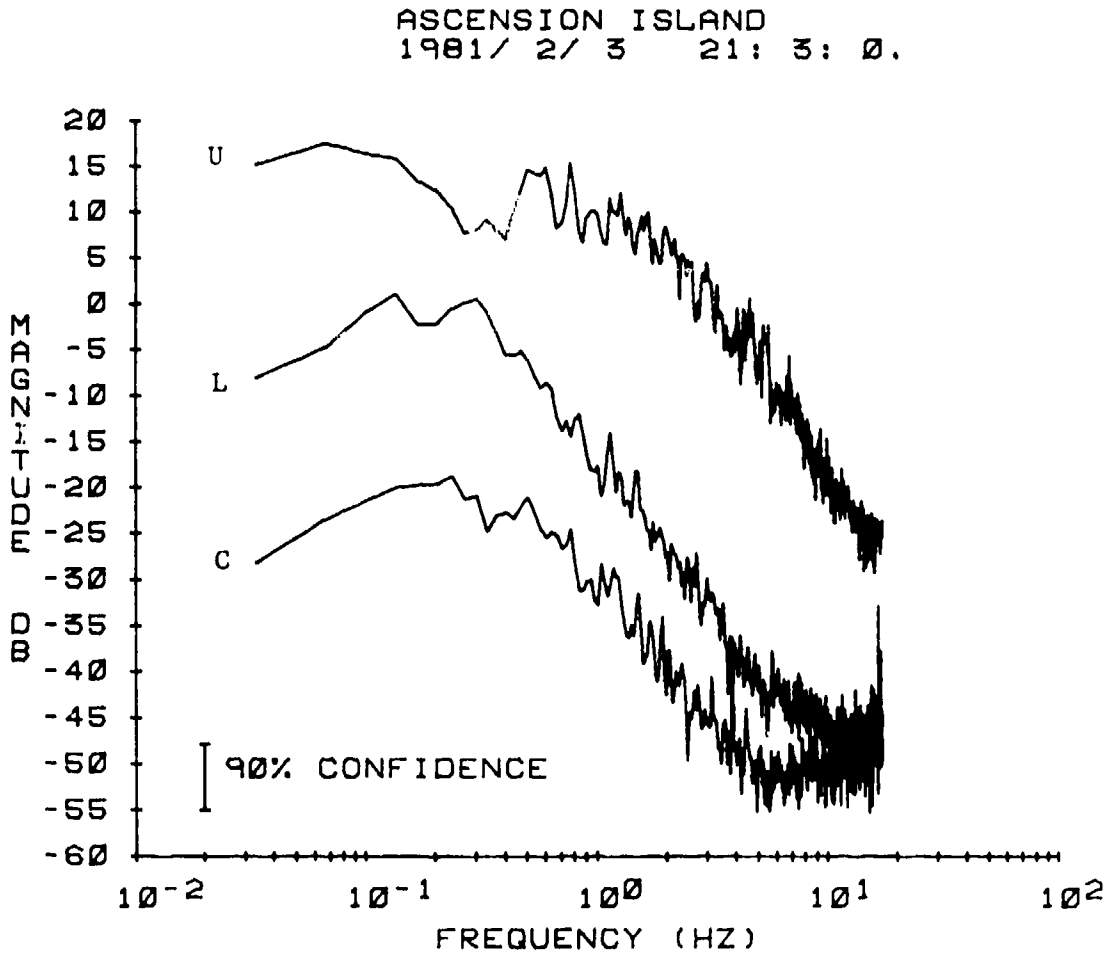
ASCENSION ISLAND
1981/ 2/ 3 21: 3: 0.
MAGNITUDE DB
20
15
10
5
0
-5
-10
-15
-20
-25
-30
-35
-40
-45
-50
-55
-60
U
L
C
90% CONFIDENCE
10-2
10-1
100
101
102
FREQUENCY (HZ)

Figure 2

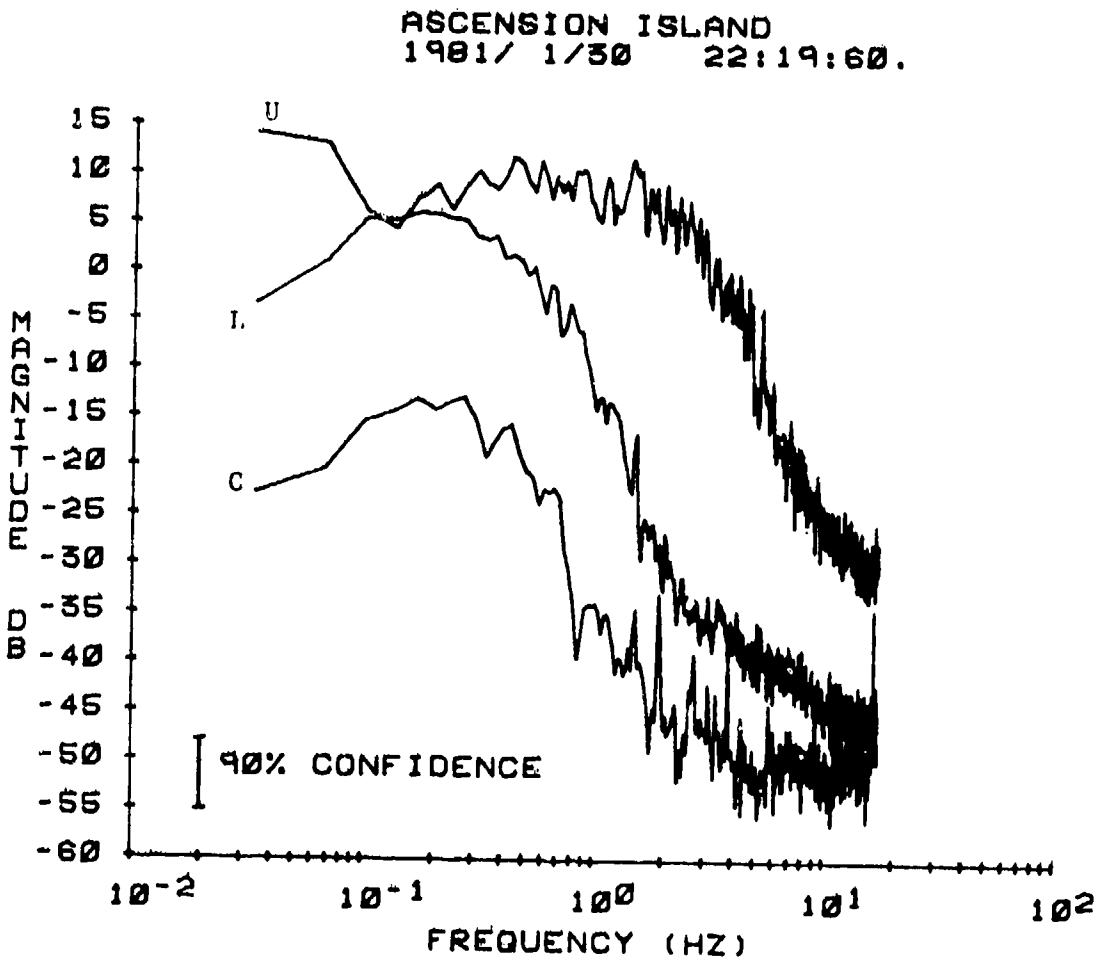
ASCENSION ISLAND
1981/ 1/30 22:19:60.
U
L
C
90% CONFIDENCE
MAGNITUDE DB
15
10
5
0
-5
-10
-15
-20
-25
-30
-35
-40
-45
-50
-55
-60
10-2
10-1
100
101
102
FREQUENCY (HZ)

Figure 3

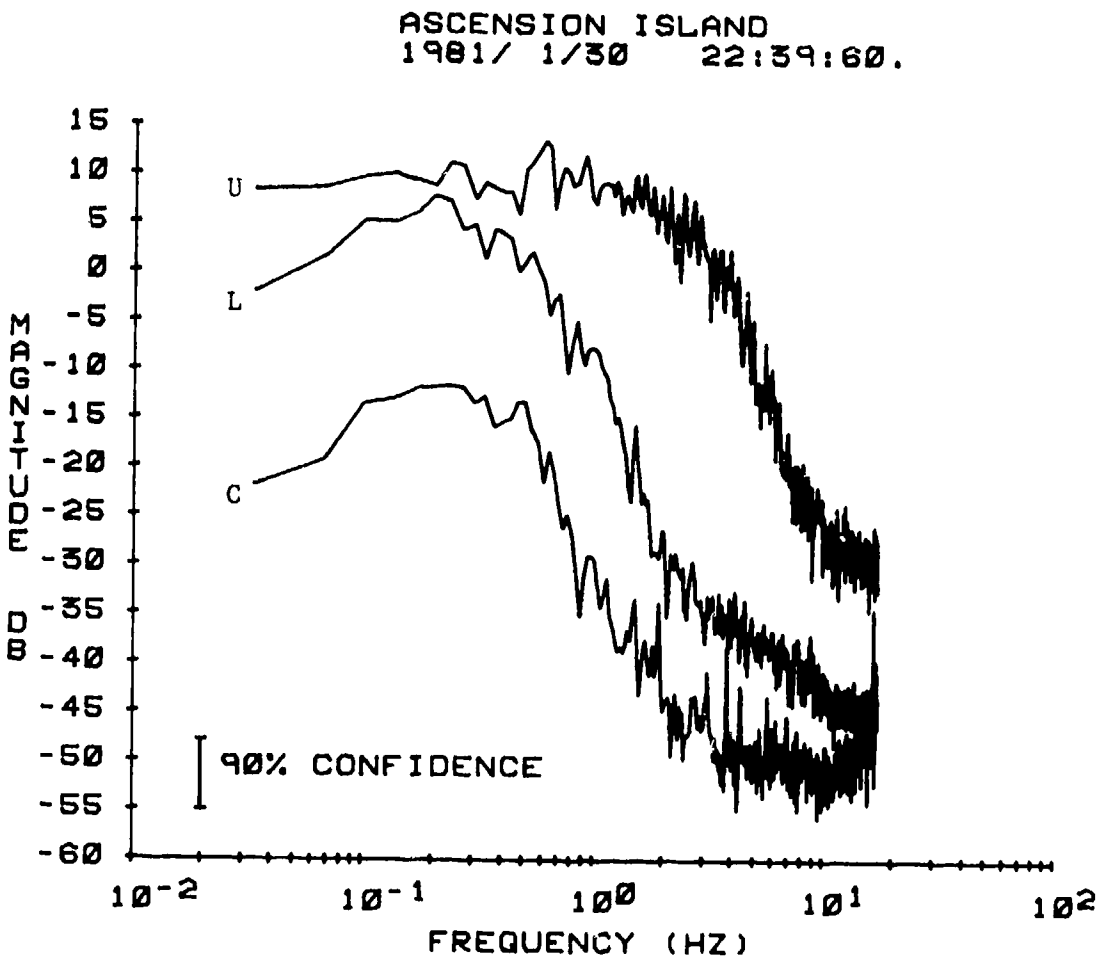
ASCENSION ISLAND
1981/ 1/30 22:39:60.
15
10
5
0
-5
-10
-15
-20
-25
-30
-35
-40
-45
-50
-55
-60
MAGNITUDE DB
U
L
C
90% CONFIDENCE
10-2
10-1
100
101
102
FREQUENCY (HZ)

Figure 4

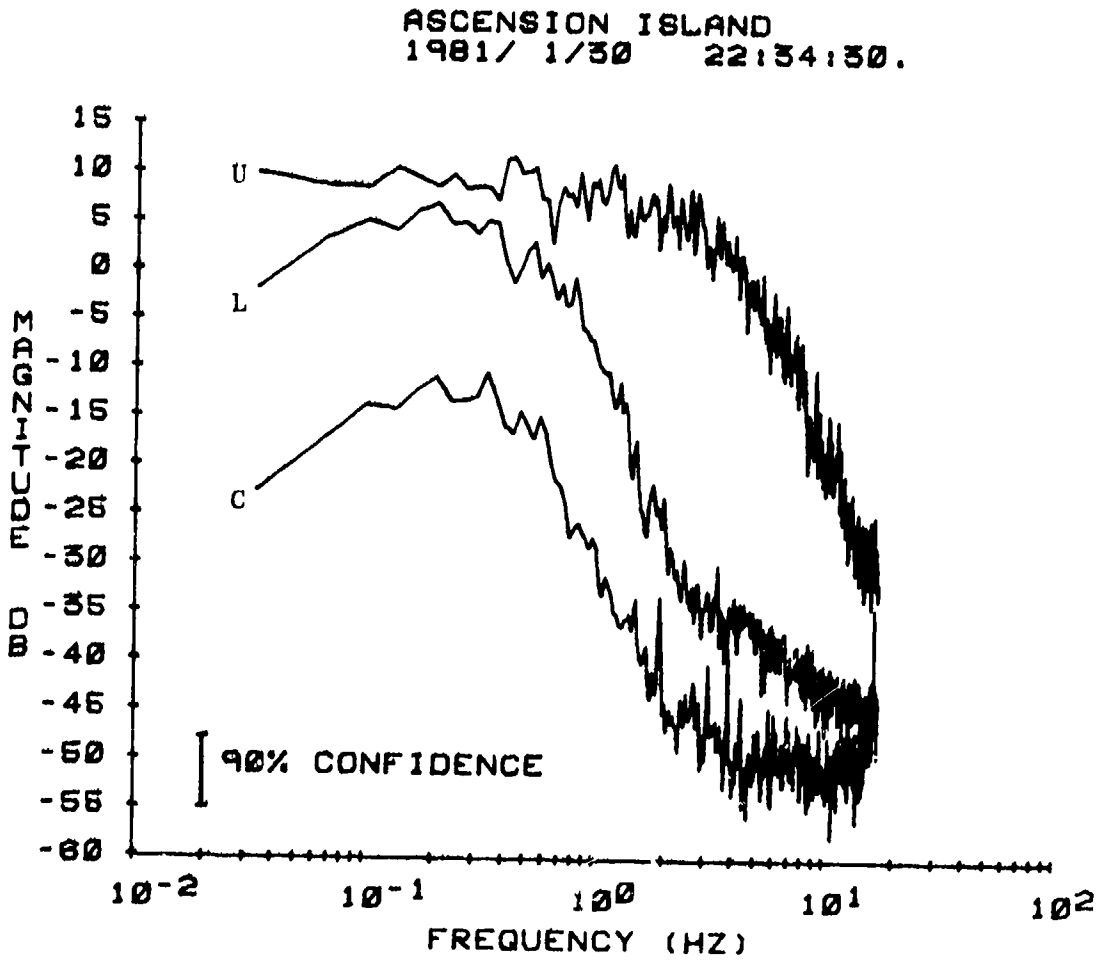
ASCENSION ISLAND
1981/ 1/30 22:34:30.
15
10
5
0
-5
-10
-15
-20
-25
-30
-35
-40
-45
-50
-55
-60
MAGNITUDE DB
U
L
C
90% CONFIDENCE
10-2
10-1
100
101
102
FREQUENCY (HZ)

Figure 5

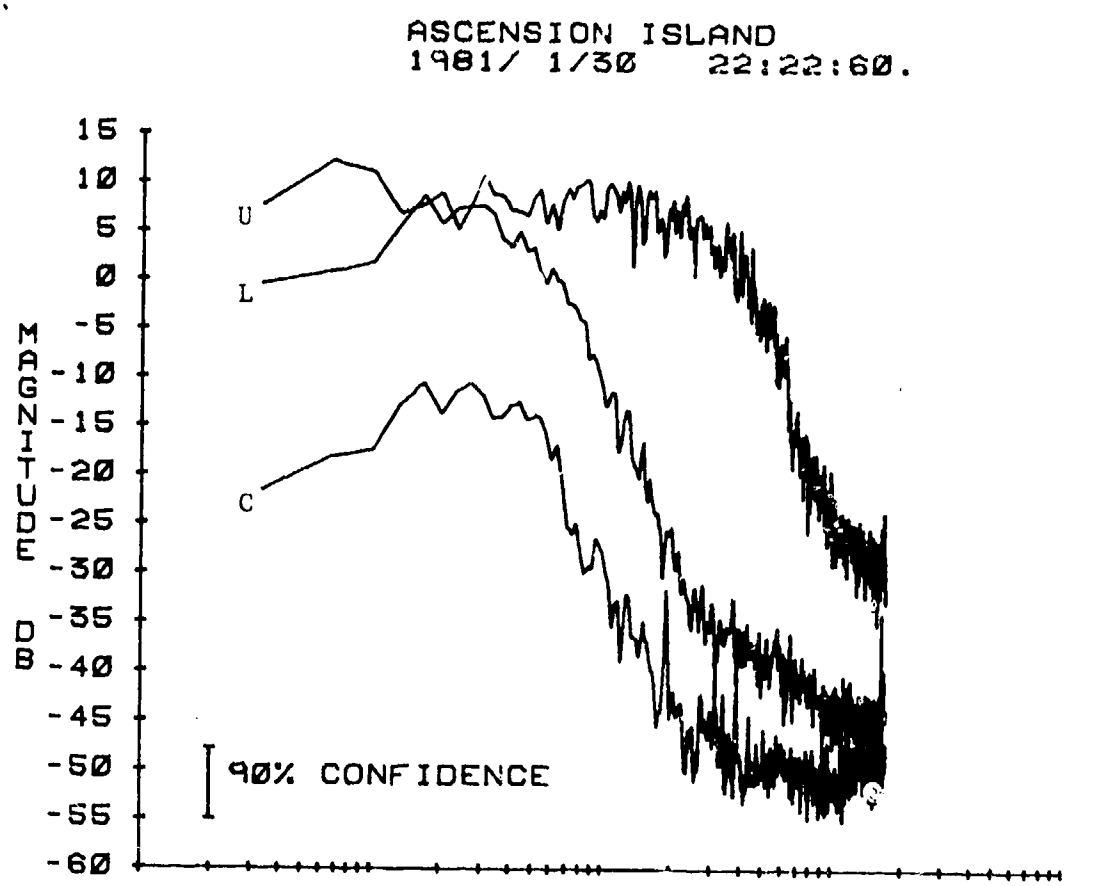
ASCENSION ISLAND
1981/ 1/30 22:22:60.
15
10
5
0
-5
-10
-15
-20
-25
-30
-35
-40
-45
-50
-55
-60
MAGNITUDE DB
U
L
C
90% CONFIDENCE
10-2
10-1
100
101
102
FREQUENCY (HZ)

Figure 6

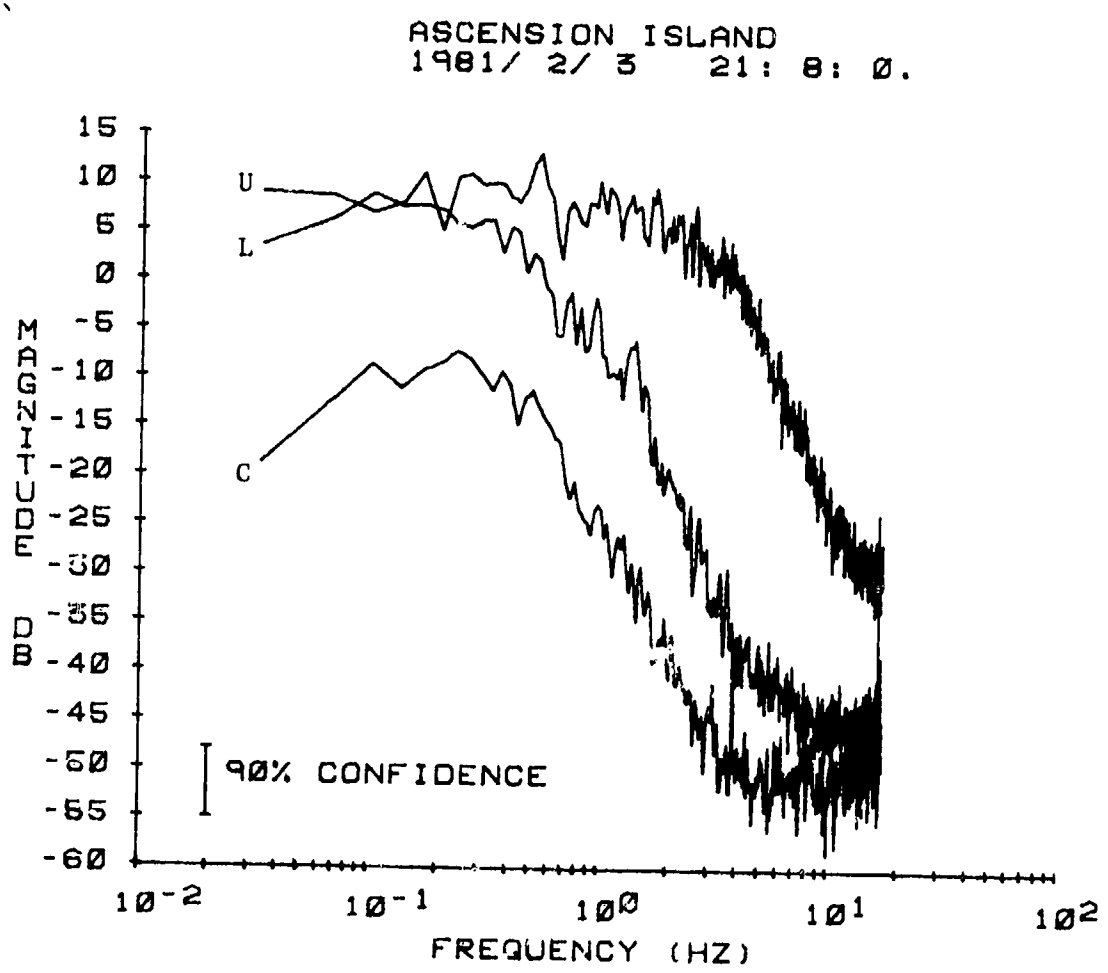
ASCENSION ISLAND
1981/ 2/ 3 21: 8: 0.
15
10
5
0
-5
-10
-15
-20
-25
-30
-35
-40
-45
-50
-55
-60
MAGNITUDE DB
U
L
C
90% CONFIDENCE
10-2
10-1
100
101
102
FREQUENCY (HZ)

Figure 7

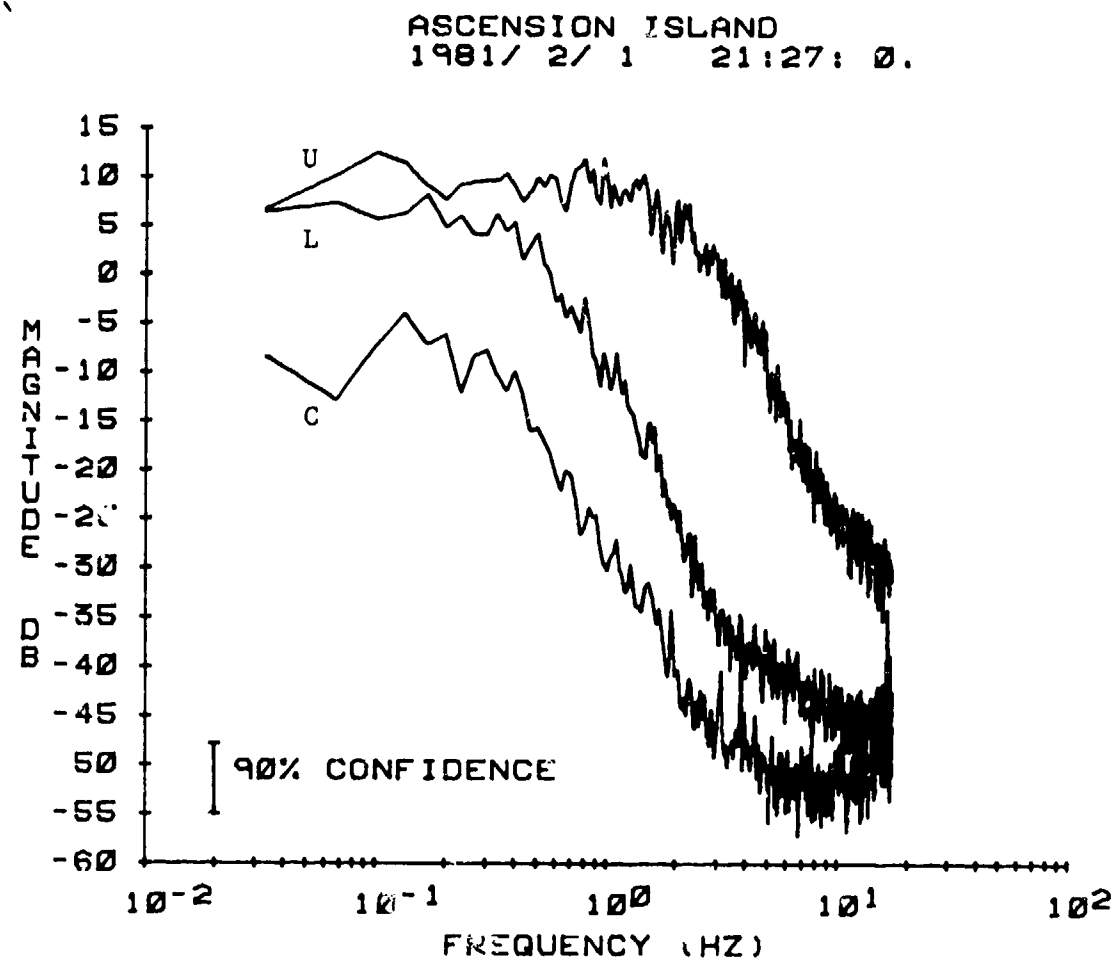
ASCENSION ISLAND
1981/ 2/ 1 21:27: 0.
15
10
5
0
-5
-10
-15
-20
-25
-30
-35
-40
-45
50
-55
-60
MAGNITUDE DB
U
L
C
90% CONFIDENCE
10-2
10-1
100
101
102
FREQUENCY (HZ)

Figure 8

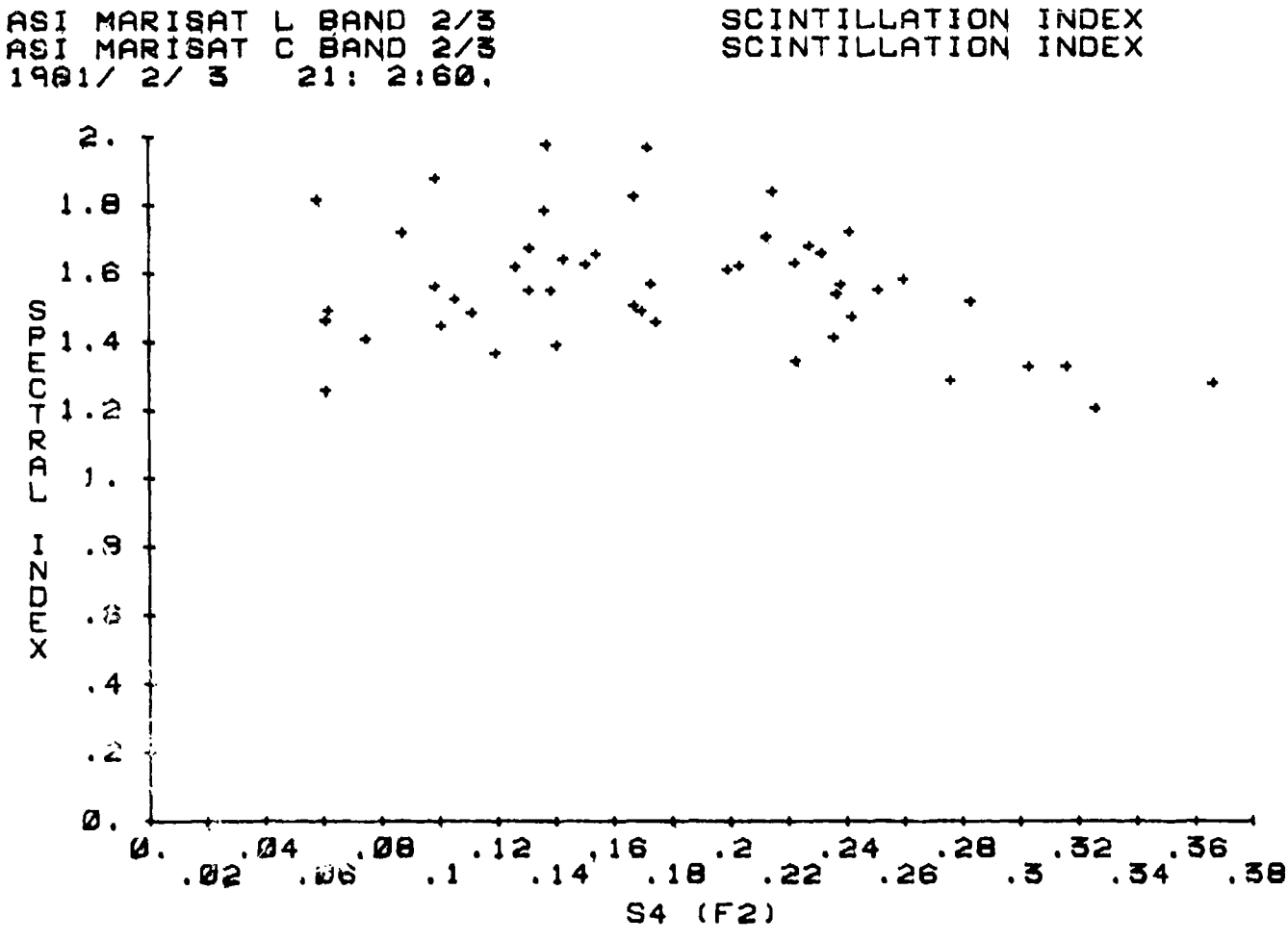
ASI MARISAT L BAND 2/3
ASI MARISAT C BAND 2/3
1981/ 2/ 3 21: 2:60.
SCINTILLATION INDEX
SCINTILLATION INDEX
SPECTRAL INDEX
2.
1.8
1.6
1.4
1.2
1.
.8
.6
.4
.2
0.
0. .02 .04 .06 .08 .1 .12 .14 .16 .18 .2 .22 .24 .26 .28 .3 .32 .34 .36 .38
S4 (F2)

Figure 9

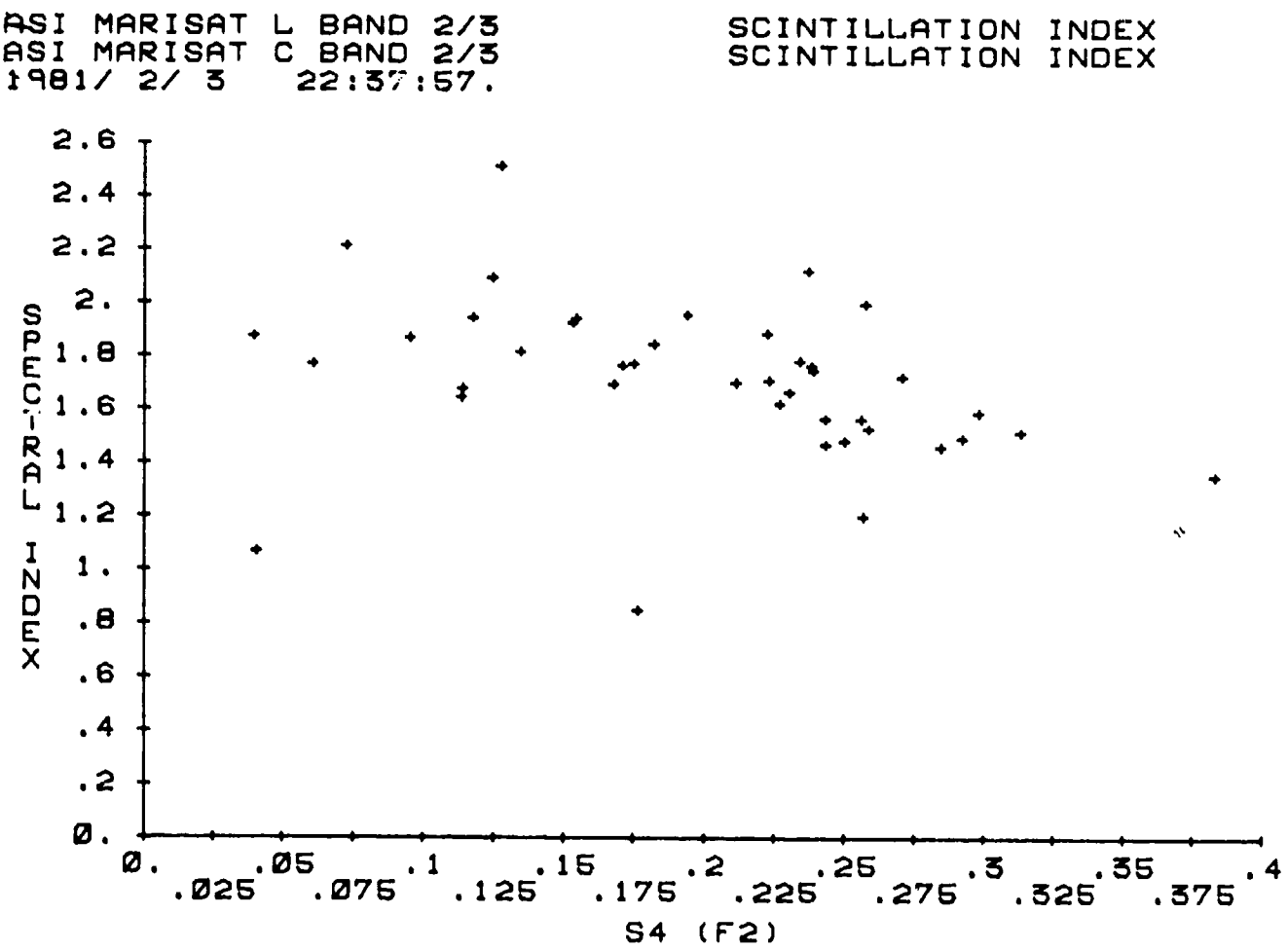
ASI MARISAT L BAND 2/3
ASI MARISAT C BAND 2/3
1981/ 2/ 3 22:37:57.
SCINTILLATION INDEX
SCINTILLATION INDEX
SPECTRAL INDEX
2.6
2.4
2.2
2.
1.8
1.6
1.4
1.2
1.
.8
.6
.4
.2
0.
0.
.025
.05
.075
.1
.125
.15
.175
.2
.225
.25
.275
.3
.325
.35
.375
.4
S4 (F2)

Figure 10

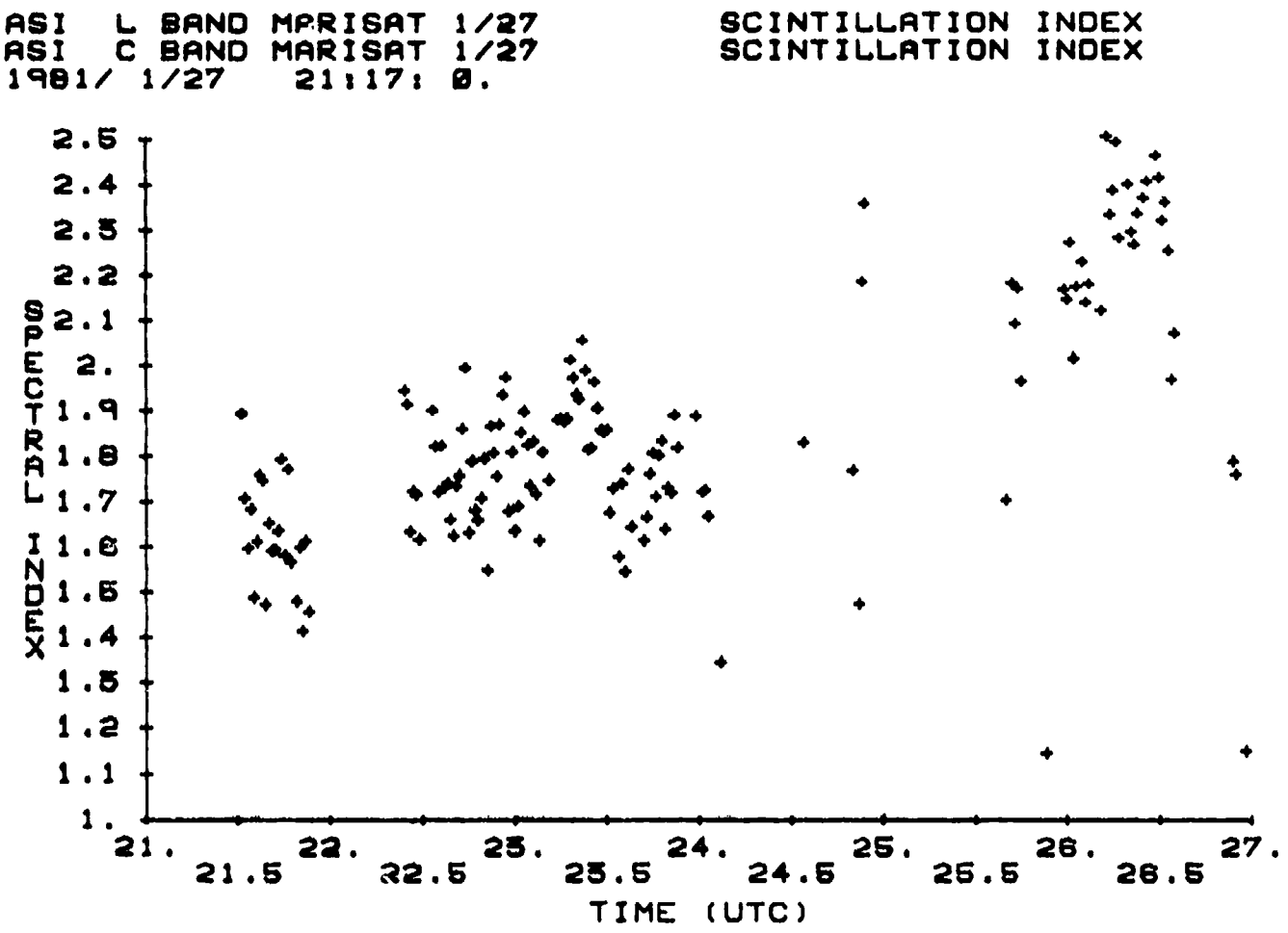
ASI L BAND MARISAT 1/27
ASI C BAND MARISAT 1/27
1981/ 1/27 21:17: 0.
SCINTILLATION INDEX
SCINTILLATION INDEX
SPECTRAL INDEX
2.5
2.4
2.3
2.2
2.1
2.
1.9
1.8
1.7
1.6
1.5
1.4
1.3
1.2
1.1
1.
21.
21.5
22.
22.5
23.
23.5
24.
24.5
25.
25.5
26.
26.5
27.
TIME (UTC)

Figure 11

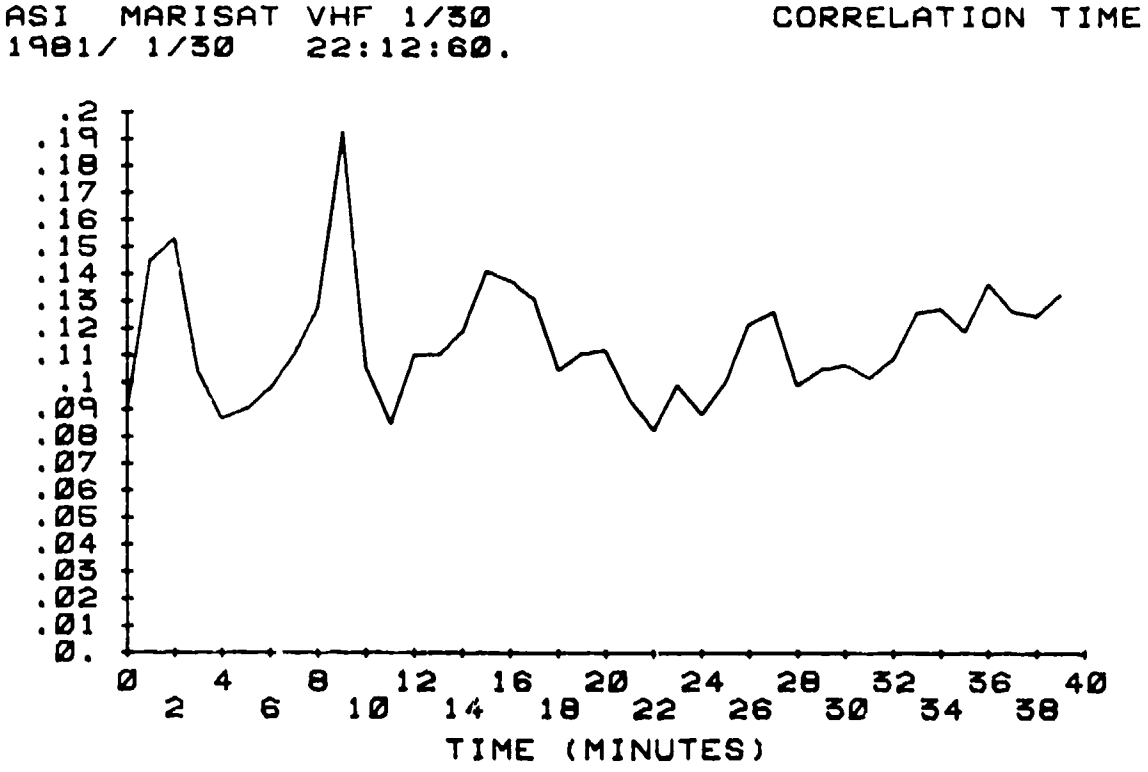

Figure 12a

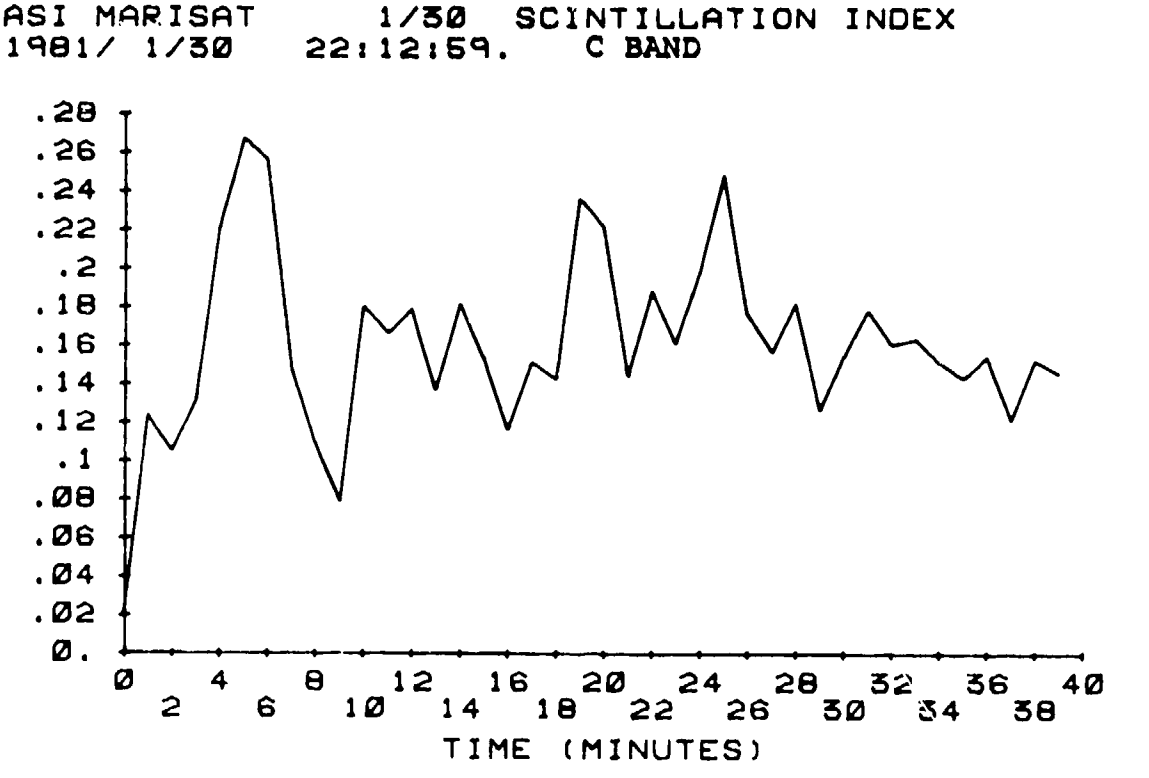

Figure 12b

Appendix A

TEMPORAL BEHAVIOR OF PULSES AFTER PROPAGATING THROUGH A TURBULENT IONOSPHERE

BY

CHIH-CHUNG YANG

B.S., National Taiwan University, 1976

THESIS

Submitted in partial fulfillment of the requirements
for the degree of Master of Science in Electrical Engineering
in the Graduate College of the
University of Illinois at Urbana-Champaign, 1981

Urbana, Illinois

Temporal Behavior of Pulses After Propagating through a Turbulent Ionosphere

Chih-Chung Yang
Department of Electrical Engineering
University of Illinois
Urbana, Illinois 61801

Abstract

A radio signal after propagating through a turbulent ionosphere will suffer distortion owing to dispersion and random scattering. For coarse description of a temporal signal, the temporal moments have been found to be convenient. Past studies have shown that the zeroth moment is related to the total energy in the pulse, the first moment is related to the mean arrival time, and the second moment is related to the mean square pulse width. In this report, we extend the analysis to the third and fourth moments which are shown to be related to the skewness and kurtosis of the pulse. The physical meanings of these quantities are explained. The numerical values of these quantities under typical ionospheric conditions are calculated.

For application to digital communications, it is desirable to know the energy content of the received pulse outside of the original pulse width. This is because an ideal pulse, due to propagation effects can be distorted and stretched to produce a long tail occupying an interval longer than one communication bit. Using the temporal moments the upper bound of the energy content outside of one chip can be estimated. The numerical values of these bounds are also computed.

Acknowledgment

The advice and suggestions of Dr. K. C. Yeh were most valuable and well-appreciated throughout this research. Spe-'al thanks go to Mrs. Linda Houston for typing the manuscript.

The research was supported by the Air Force Geophysics Laboratory and Headquarter Space Division through contract F19628-78-C-0195.

Appendix A

Table of Contents

1. Introduction

When signals propagate through a dispersive and random medium, they suffer distortion due to frequency dispersion and random scattering. The main feature of this distortion is the broadening of the signal. In binary communication, the broadened signal in one bit may extend into the neighboring bits. If it is of sufficient amplitude, this extension can produce serious errors in the decision making process. A practical example is the satellite-earth communication link. The signal in this case must traverse the ionosphere and may become broadened because of dispersive and scattering effects taking place in the ionosphere. In this report, it is proposed to describe the temporal distribution of the signal intensity in terms of its temporal moments and show how these temporal moments evolve as the signal propagates through a turbulent plasma medium. The results of this research may help to determine under what conditions the decision making errors can be considerably reduced.

The theory of using first few temporal moments to describe the temporal distribution of the received signal has been formulated by Yeh and Liu [1977a]. The works done before include the calculation of up to the third moment in a nondispersive medium [Liu et al., 1978] and up to the second moment in a dispersive medium [Yeh and Yang, 1977c; Liu and Yeh, 1977; Yeh and Liu, 1977b; Yeh and Liu, 1979]. In Chapter 2 of this report, the evaluation of temporal moments is extended to the fourth order. Meanwhile the medium will be assumed to be dispersive as well as turbulent. In this calculation, the two-frequency mutual coherence function, Γ, is expanded into a power series of the relative difference of the wave numbers. For the purpose of computing temporal moments it is sufficient

to evaluate the series coefficients only up to the desired order. The equation for Γ will be derived by using the Markov approximation under the assumption of forward scattering.

Chapter 3 contains a discussion of the physical significance of the moments formulated in Chapter 2. Quantities such as skewness and kurtosis will then be defined in terms of the temporal moments. These quantities are used to describe the temporal characteristics of the signal intensity distribution. The formulas will then be specified by two sets of parameters that describe the geometry and content of the medium. Numerical results will be presented as graphs.

Some properties of moments will be used in Chapter 4 to describe the trailing tail of the received signal. By using these properties, the upper bound for the fractional energy of the signal outside a time interval can be calculated. With binary communication application in mind, we calculate the upper bound of the fractional energy of the signal contained in the neighboring bits. Some numerical results will be shown.

The geometry of the problem is shown in Figure 1. We assume that there exists a plasma medium with a homogeneous background in the region $z \geq 0$ and that random irregularities exist only inside the slab between $z=0$ and $z=L$. The positions of the transmitter and the receiver are also shown in this figure. Note that the receiver is always at a position with $z \geq L$. Carrier plane waves with a Guassian envelope are assumed to be incident at $z=0$.

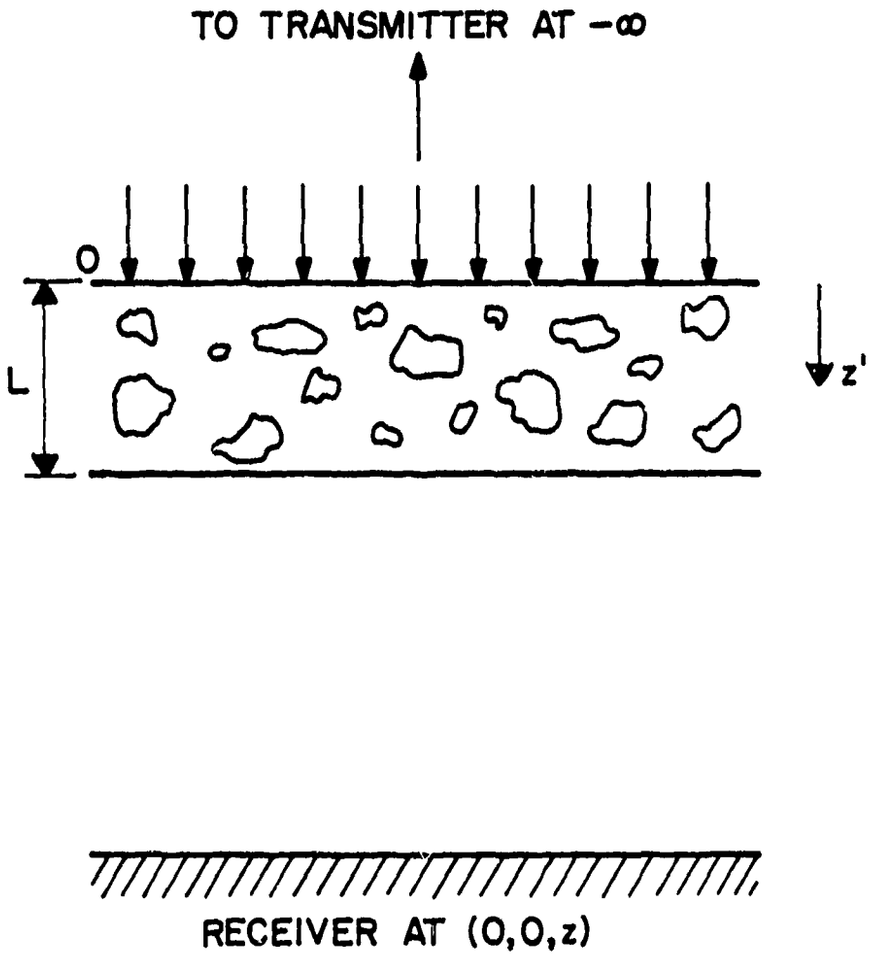

Figure 1. The geometry of the problem. Note that plasma occupies the whole region $0 \leq z' \leq z$, but only inside the slab $0 \leq z' \leq L$, there exists random irregularities.

2. Calculation of Temporal Moments

We give the definitions of the moments first. The equation for two-frequency mutual coherence function, Γ, is then derived under the forward scattering assumption and Markov approximation. Γ is expanded into a power series of the relative difference of wave numbers. The coefficients of this series up to fourth order are evaluated. Moments up to fourth order can then be computed. This method for calculation of temporal moments was introduced by Yeh and Liu [1977a].

The computations for the third and the fourth moment are quite tedious. We can imagine that the work of evaluating the fifth or any higher order moment will be more tedious and it will be easy for us to make mistakes. So we will stop at the fourth moment, although any higher order moment can give us more information about the signal shape.

2.1 Definition of the Moments

The problem of plane wave propagation in a random medium is usually formulated by the equation

$$P(z,t) = \int_{-\infty}^{\infty} f(\omega)u(z,\omega)e^{j[\omega t-k(\omega)z]}\,d\omega \qquad (1)$$

Here we assume that the wave propagates in the z direction. In this equation, $u(z,\omega)$ is the complex amplitude and is assumed to be unity at the boundary, i.e., $u(0,\omega)=1$ at $z=0$ in our geometry of the problem. $u(z,\omega)$ is used to describe the random effect on the signal component at circular frequency ω in the medium. In general u is a random function of transverse coordinate $\vec{\rho}$ as well as z and ω. When there is no cause of confusion, the explicit indication of such dependences will be suppressed. $f(\omega)$ is the

frequency spectrum of the signal impressed. $k(\omega)$ is the wave number and usually includes the dispersive characteristics of the medium. We note for real $P(z,t)$, both $f(\omega)$ and $u(z,\omega)$ are required to be even in ω, which we assume.

Rewrite equation (1) in the form

$$P(z,t) = \mathrm{Re}A(z,t)\ \exp[j(\omega_c t - k_c z)] \tag{2}$$

This represents a wave of carrier frequency ω_c, wave number $k_c = k(\omega_c)$, and slowly varying complex envelope A. A is given by

$$A(z,t) = \int_{-\infty}^{\infty} F(\Omega)U(z,\Omega)e^{j[\Omega t-(k-k_c)z]}\,d\Omega \tag{3}$$

where $F(\Omega)=f(\omega_c+\Omega)$, $U(z,\Omega)=u(z,\omega_c+\Omega)$ and $\Omega=\omega-\omega_c$. Note that $A(z,t)$ is random since $u(z,\omega)$ is random.

Define the nth temporal moment by the equation

$$M^{(n)}(z) \equiv \int_{-\infty}^{\infty} \langle A^*(z,t)t^n A(z,t)\rangle dt \qquad n=0,1,2,\ \ldots. \tag{4}$$

Here the notation $\langle\ \rangle$ denotes an ensemble average. Insertion of equation (3) in (4) leads to

$$M^{(n)}(z) = \iiint_{-\infty}^{\infty} F^*(\Omega_2)F(\Omega_1)\Gamma t^n \exp\{j[\Omega_1-\Omega_2)t-(k_1-k_2)z]\}d\Omega_2 d\Omega_2 dt \tag{5}$$

where $k_1 \equiv k(\omega_1)$ and $k_2 \equiv k(\omega_2)$ and Γ is the two-frequency one-position mutual coherence function given by

$$\Gamma \equiv \langle U'\vec{\rho},z,\Omega_1)U^*(\vec{\rho},z,\Omega_2)\rangle = \langle u(\vec{\rho},z,\omega_1)u^*(\vec{\rho},z,\omega_2)$$

In order to proceed further in equation (5), we need the relation

$$\int_{-\infty}^{\infty} t^n\, e^{j(\Omega_1-\Omega_2)t}\,dt = 2\pi(-j)^n\delta^{(n)}(\Omega_1-\Omega_2) \tag{6}$$

where $\delta^{(n)}(\Omega_1-\Omega_2)$ is the nth-order Dirac delta function. Using equation (6), equation (5) becomes

$$M^{(n)}(z) = 2\pi(j)^n \int_{-\infty}^{\infty} F^*(\Omega_2) e^{jk_2 z} \left. \frac{\partial^n [F(\Omega_1)\Gamma\, e^{-jk_1 z}]}{\partial \Omega_1^{\,n}} \right|_{\Omega_1=\Omega_2} d\Omega_2 \tag{7}$$

Further integration of (7) requires knowledge in Γ. The form of (7) suggests an expansion of Γ in the series

$$\Gamma(k_1,k_2) = \Gamma_0+\Gamma_1\eta+\Gamma_2\,\eta^2+ \ldots. \tag{8}$$

where $\eta=(k_2-k_1)/k_2$, and

$$\Gamma_n = \frac{1}{n!} \left. \frac{\partial \Gamma^n}{\partial \eta^n} \right|_{\eta=0} \tag{9}$$

As can be seen in (7), the nth temporal moment depends only on Γ_0, Γ_1, ... Γ_n and not on Γ_{n+1} and higher order terms.

Once Γ_0, Γ_1, ... Γ_n are calculated, we can obtain $M^{(n)}(z)$ quite straightforwardly although the operation can be very tedious as we shall find later on.

2.2 Equation for Two-Frequency Mutual Coherence Function

To derive the equation for Γ, let us start from the Helmholtz wave equation for the wave function Ψ

$$\nabla^2\Psi+k^2(1+\beta\xi)\Psi = 0 \tag{10}$$

where the time dependence $\exp(j\omega t)$ is understood. The random function ξ is assumed to be a homogeneous random field and is independent of frequency. The frequency dependence is included in the factor β. In a turbulent plasma medium

$$\beta = -\frac{\omega_p^2}{\omega^2-\omega_p^2}, \qquad \xi = \frac{\Delta N}{N} \tag{11}$$

where ω_p is the circular plasma frequency and N is the electron density of the background medium which is assumed to be homogeneous. ΔN is the fluctuating electron density. The validity of equation (10) for various waves has been discussed by Tatarskii [1971]. In general it requires that the typical turbulent scale be large compared with the wavelength, which we assume.

From equation (10) and under the forward scattering assumption we can obtain the parabolic equation for the complex amplitude u as

$$\nabla_T^2 u - 2jk\frac{\partial u}{\partial z} + k^2\beta(\omega)\xi(\vec{\rho},z)u = 0 \tag{12}$$

where u and Ψ are related by $\Psi = u\exp(-jkz)$ and $\nabla_T^2 = \frac{\partial^2}{\partial x^2} + \frac{\partial^2}{\partial y^2}$ and $\vec{\rho}=(x,y)$. From equation (12), under the Markov approximation, the equation for the two-frequency, two-position mutual coherence function

$$\Gamma(\vec{\rho}_1,\vec{\rho}_2) \equiv \langle u(\vec{\rho}_1,z,\omega_1)u^*(\vec{\rho}_2,z,\omega_2)\rangle$$

can be derived [Tatarskii, 1971]

$$\frac{\partial\Gamma(\vec{\rho}_1,\vec{\rho}_2)}{\partial z} + \frac{j}{2k_1k_2}(k_2\nabla_{T_1}^2 - k_1\nabla_{T_1}^2)\Gamma(\vec{\rho}_1,\vec{\rho}_2) - \frac{1}{2}A_p(\vec{\rho}_2-\vec{\rho}_1)\Gamma(\vec{\rho}_1,\vec{\rho}_2) = 0 \tag{13}$$

Here we denote this two-position function by $\Gamma(\vec{\rho}_1,\vec{\rho}_2)$, so that it can be distinguished from the one-position ($\vec{\rho}_1=\vec{\rho}_2$) function Γ in Section 2.1. The dependence on frequencies is suppressed when it is not explicitly needed. In the equation above $A_p(\vec{\rho}_2-\vec{\rho}_1)$ is given by

$$A_p(\vec{\rho}_2-\vec{\rho}_1) = \frac{-1}{4}[(k_1^2\beta_1^2+k_2^2\beta_2^2)A_\xi(0) - 2k_1\beta_1k_2\beta_2A_\xi(\vec{\rho}_2-\vec{\rho}_1)] \tag{14}$$

where $\beta_1\equiv\beta(\omega_1)$, $\beta_2=\beta(\omega_2)$ and $A_\xi(\vec{\rho})$ is defined by

$$A_\xi(\vec{\rho}) \equiv \int_{-\infty}^{\infty} B_\xi(\vec{\rho},z)dz \tag{15}$$

and

$$B_\xi(\vec{\rho},z) \equiv <\xi(\vec{\rho}_1',z')\xi(\vec{\rho}'+\vec{\rho},z'+z)> \tag{16}$$

where $\xi(\vec{\rho},z)$ is a homogeneous random field. If plane waves are impressed at z=0, $\Gamma(\vec{\rho}_1,\vec{\rho}_2)$ is a function of $\vec{\rho}_2-\vec{\rho}_1=\vec{\rho}$ and equation (13) becomes

$$\frac{\partial\Gamma(\vec{\rho})}{\partial z} + \frac{j\Delta k}{2k_1k_2}\nabla_T^2\Gamma(\vec{\rho}) - \frac{1}{2}A_p(\vec{\rho})\Gamma(\vec{\rho}) = 0 \tag{17}$$

where $\Delta k=k_2-k_1$. The boundary condition for (17) is $\Gamma(\vec{\rho})=1$ at z=0.

Since for the calculation of up to the fourth moment, only Γ_0, Γ_1, Γ_2, Γ_3, Γ_4 are required, it is not necessary to solve equation (17) for Γ itself, but its expression suggested in (18).

When $0\leq z\leq L$, let's assume

$$\Gamma(\vec{\rho}) = W(z)\exp\phi(z) \tag{18}$$

Where

$$\phi(z) = -(k_1^2\beta_1^2 + k_2^2\beta_2^2)A_\xi(0)z/8$$

Expand W(z) in the form

$$W = W_0+W_1\eta+W_2\eta^2+ \ldots\ldots \tag{19}$$

If equations (18) and (19) are substituted in (17), inside the turbulent slab, i.e., $0\leq z\leq L$, we obtain the following general equation:

$$\frac{\partial W_n}{\partial z} - \frac{1}{4}k_2^2\beta_2^2A_\xi(\vec{\rho})W_n = [-\frac{1}{2k_2}\nabla_T^2 + \frac{1}{4}k_2^2\beta_2^2A_\xi(\vec{\rho})]\ [W_{n-1}+W_{n-2}+ \ldots +W_1+W_0]$$

$$n = 1, 2, 3, \ldots. \tag{20}$$

and

$$\frac{\partial W_0}{\partial z} - \frac{1}{4} k_2^2 \beta_2^2 A_\xi(\vec{\rho}) W_0 = 0 \qquad (21)$$

The boundary conditions at z=0 are

$$W_0=1,\ W_1=W_2= \ldots = 0 \qquad (22)$$

Note that in the process above we have used the expansion of β_1

$$\beta_1 = \beta_2+2\beta_2\eta+3\beta_2\eta+ \ldots + (n+1)\beta_2\eta^n+ \ldots\ldots \qquad (23)$$

which can be shown to be valid by using (11). When z>L, i.e., outside the turbulence slab, we write

$$\Gamma(\vec{\rho}) = W'(z)\ \exp\phi(L) \qquad (24)$$

We also expand W'(z) into a power series

$$W'(z) = W_0'+W_1'\eta+W_2'\eta^2+ \ldots\ldots \qquad (25)$$

The corresponding equations of (20) and (21) can be written directly by setting $A_\xi(\vec{\rho})=0$ in equations (20) and (21), i.e.,

$$\frac{\partial W'_n}{\partial z} = -\frac{i}{2k_2} \nabla_T^2 (W'_{n-1}+W'_{n-2}+ \ldots +W'_0) \qquad n = 1,2,3, \ldots \qquad (26)$$

and

$$\frac{\partial W_0'}{\partial z} = 0 \qquad (27)$$

The boundary conditions at z=L are

$$W_0'(L) = W_0(L),\ W_1'(L)=W_1(L),\ \ldots\ldots \qquad (28)$$

From equation (20), we rewrite the same equation for W_{n-1}, i.e.

$$\frac{\partial W_{n-1}}{\partial z} - \frac{1}{4} k_2^2 \beta_2^2 A_\xi(\vec{\rho}) W_{n-1} = [\frac{-j}{2k_2} \nabla_T^2 + \frac{1}{4} k_2^2 \beta_2^2 A_\xi(\vec{\rho})] [W_{n-2}+W_{n-3}+....+W_1+W_0] \tag{29}$$

Subtracting (28) from (20) we obtain

$$\frac{\partial (W_n - W_{n-1})}{\partial z} - \frac{1}{4} k_2^2 \beta_2^2 A_\xi(\vec{\rho}) (W_n - W_{n-1}) = [\frac{-j}{2k_2} \nabla_T^2 + \frac{1}{4} k_2^2 \beta_2^2 A_\xi(\vec{\rho})] W_{n-1} \tag{30}$$

Then a set of recurrent formulas for W_n can be obtained for $0 \leq z \leq L$

$$W_n(z) = W_{n-1}(z) + \int_0^z e^{\frac{1}{4} k_2^2 \beta_2^2 A_\xi(\vec{\rho})(z-z')} [-\frac{j}{2k_2} \nabla_T^2 + \frac{1}{4} k_2^2 \beta_2^2 A_\xi(\vec{\rho})] W_{n-1}(z')dz' \tag{31}$$

$$n=2,3,4 .....$$

$$W_1(z) = W_0(z) + \int_0^z e^{\frac{1}{4} k_2^2 \beta_2^2 A_\xi(\vec{\rho})(z-z')} [-\frac{j}{2k_2} \nabla_T^2 + \frac{1}{4} k_2^2 \beta_2^2 A_\xi(\vec{\rho})] W_0(z')dz' - e^{\frac{1}{4} k_2^2 \beta_2^2 A_\xi(\vec{\rho}) z} \tag{32}$$

It is easy to obtain a similar set of recurrent formulas for W_n'

$$W_n'(z) - W_n'(L) = [W'_{n-1}(z) - W'_{n-1}(L)] - \frac{j}{2k_2} \int_L^z \nabla_T^2 W_{n-1}(z')dz' \tag{33}$$

$$n=1,2,3, ...$$

Note that in deriving equation (30), (31), and (32) we have used the boundary conditions in equations (22) and (28). From equations (21), (22), (26) and (27) we can evaluate W_0 and W_0'

$$W_0(z) = \exp [\frac{1}{4} k_2^2 \beta_2^2 A_\xi(\vec{\rho}) z] \tag{34}$$

and

$$W_0'(z) = W_0(L) = \exp\left[\frac{1}{4} k_2^2 \beta_2^2 A_\xi(\vec{\rho}) L\right] \tag{35}$$

Using equation (34) and (35) as the starting point, the recurrent formulas (31) and (33) will lead to $W_n(z)$ and then $W_n'(z)$ for any n=1,2,3, ... After we have these results, equations (23), (24) and the relation

$$\Gamma_n = \frac{1}{n!} \frac{\partial \Gamma^n(\vec{\rho})}{\partial \eta^n} \Big|_{\eta=0,\ \vec{\rho}=0} \qquad n=0,1,2, \ldots \tag{36}$$

can be used to obtain Γ_0, Γ_1, Γ_2, Γ_3 and Γ_4 for z>L.

2.3 The Formulas for Γ_0, Γ_1, Γ_2, Γ_3, Γ_4

If we assume the random field $\xi=\Delta N/N$ is isotropic as well as homogeneous, then $A_\xi(\vec{\rho})=A_\xi(\rho)$. Since $A_\xi(\rho)$ is an even function, we can expand $A_\xi(\rho)$

$$A_\xi(\vec{\rho}) = A_\xi(\rho) = A_0+A_2\rho^2+A_4\rho^4+A_6\rho^6+A_8\rho^8+ \ldots\ldots \tag{37}$$

So

$$A_\xi(\rho)\Big|_{\rho=0} = A_0$$

$$\nabla_T A_\xi(\rho)\Big|_{\rho=0} = 0$$

$$\nabla_T^2 A_\xi(\rho)\Big|_{\rho=0} = 4A_2$$

.....

Having these identities above, we are ready to calculate Γ_0, Γ_1, Γ_2, Γ_3, Γ_4. As stated in the last paragraph of Section 2.2, once W_0', W_1', W_2', W_3', W_4', are obtained, we can evaluate Γ_0, Γ_1, Γ_2, Γ_3, Γ_4 from equation (24) and (36). For the region $z \geq L$, the results are as follows:

$$\Gamma_0 = 1 \tag{38}$$

$$\Gamma_1 = -\frac{1}{4} k_2\beta_2^2 A_2(2Lz-L^2) \tag{39}$$

$$\Gamma_2 = -\frac{1}{8} k_2^2\beta_2^2 A_0 L - \frac{j}{2}k_2\beta_2^2 A_2(2Lz-L^2)$$
$$-\frac{2}{3}\beta_2^2 A_4(3Lz^2-3L^2z+L^3)-k_2^2\beta_2^4 A_2^2(\frac{1}{4} L^2z^2-\frac{7}{24} L^3z+\frac{3}{32} L^4) \tag{40}$$

$$\Gamma_3 = -\frac{1}{4} k_2^2\beta_2^2 A_0 L - \frac{3j}{4} k_2\beta_2^2 A_2(2Lz-L^2)$$
$$-2\beta_2^2 A_4(3Lz^2-3L^2z+L^3)+j\frac{\beta_2^2}{k_2} A_6(12Lz^3-18L^2z^2+12L^3z$$
$$-3L^4)-k_2^2\beta_2^4 A_2^2(L^2z^2-\frac{7}{6} L^3z+\frac{3}{8} L^4)$$
$$+\frac{j}{5760} k_2^3\beta_2^6 A_2^3(720L^3z^3-1320L^4z^2+846L^5z-185L^6)$$
$$+\frac{j}{32} k_2^3\beta_2^4 A_0A_2(2L^2z-L^3)+\frac{j}{6} k_2\beta_2^4 A_2A_4(18L^2z^3$$
$$-31L^3z^2+20L^4z-\frac{23}{5} L^5) \tag{41}$$

$$\Gamma_4 = \frac{1}{128} k_2^4\beta_2^4 A_0^2L^2 - \frac{3}{8} k_2^2\beta_2^2 A_0 L$$
$$+k_2^4\beta_2^8 A_2^4(\frac{1}{16} L^4z^4-\frac{5}{32} L^5z^3+\frac{871}{5760} L^6z^2-\frac{5363}{80640} L^7z+\frac{7217}{645120} L^8)$$
$$+jk_2^3\beta_2^6 A_2^3(\frac{3}{4} L^3z^3-\frac{11}{8} L^4z^2+\frac{141}{160} L^5z-\frac{37}{192} L^6)$$
$$-k_2^2\beta_2^4 A_2^2(\frac{5}{2} L^2z^2-\frac{35}{12} L^3z+\frac{15}{16} L^4)$$
$$-jk_2\beta_2^2 A_2(2Lz-L^2)$$
$$+k_2^4\beta_2^6 A_0A_2^2(\frac{1}{32} L^3z^2-\frac{7}{192} L^4z+\frac{3}{256} L^5)$$
$$+jk_2^3\beta_2^4 A_0A_2(\frac{1}{4} L^2z-\frac{1}{8} L^3)$$
$$+\beta_2^4 A_4^2(12L^2z^4-28L^3z^3+\frac{82}{3} L^4z^2-\frac{188}{15} L^5z+\frac{20}{9} L^6)$$

continued on next page

$$-\beta_2^2 A_4(12Lz^2-12L^2z+4L^3)$$

$$-jk_2\beta_2^4 A_2A_4(15L^2z^3-\frac{155}{6}L^3z^2+\frac{50}{3}L^4z-\frac{23}{6}L^5)$$

$$+k_2^2\beta_2^6 A_2^2A_4(3L^3z^4-\frac{29}{4}L^4z^3+\frac{337}{48}L^5z^2-\frac{2381}{720}L^6z+\frac{379}{560}L^7)$$

$$+k_2^2\beta_2^4 A_0A_4(\frac{1}{4}L^2z^2-\frac{1}{4}L^3z+\frac{1}{12}L^4)$$

$$+j\frac{\beta_2^2}{k_2}A_6(48Lz^3-72L^2z^2+48L^3z-12L^4)$$

$$+\beta_2^4 A_2A_6(\frac{45}{2}L^2z^4-51L^3z^3+\frac{201}{4}L^4z^2-\frac{243}{10}L^5z+\frac{19}{4}L^6)$$

$$+\frac{\beta_2^2}{k_2^2}A_8(96Lz^4-192L^2z^3+192L^3z^2-96L^4z+\frac{96}{5}L^5) \qquad (42)$$

where

$$k_2 = (\omega_2/c)(1-\omega_p^2/\omega_2^2)^{1/2} \qquad (43)$$

and

$$\beta_2 = -\omega_p^2/(\omega_2^2-\omega_p^2)$$

in a turbulent plasma.

2.4 Formulas for Temporal Moments

Now, we consider a plane wave Gaussian pulse at carrier frequency ω_c propagating through a turbulent plasma. The envelope of the original pulse is given by

$$A(t) = \exp(-t^2/T_0^2)$$

In other words, we have the frequency spectrum

$$f(\omega) = \frac{1}{2\pi}\int_{-\infty}^{\infty} e^{-t^2/T_0^2}\cos\omega_c t\, e^{j\omega t}\, dt = \frac{T_0}{4\sqrt{\pi}}\{\exp[-T_0^2(\omega+\omega_c)^2/4]$$

$$+\exp[-T_0^2(\omega-\omega_c)^2/4]\} \qquad (44)$$

From the relation $F(\Omega)=f(\omega_c+\Omega)$ and $\Omega=\omega-\omega_c$, we have

$$F(\Omega) = F_-(\Omega)+F_+(\Omega)$$

where

$$F_-(\Omega) \equiv \frac{T_0}{4\sqrt{\pi}} \{\exp[-T_0{}^2(\Omega+ 2\omega_c)^2/4]\}$$

$$F_+(\Omega) \equiv \frac{T_0}{4\sqrt{\pi}} \{\exp[-T_0{}^2\Omega^2/4]\}$$

Since the value of T_0 gives an order of magnitude for the original signal width, usually $T_0\omega_c$ is much greater than one, which we assume. This implies that $F_-(\Omega)$ and $\partial^n F_-(\Omega)/\partial\Omega^n$ for n=1,2,3,4 are nearly zero in the region $\Omega \gtrsim -\omega_c$, meanwhile $F_+(\Omega)$ and $\partial^n F_+(\Omega)/\partial\Omega^n$ for n=1,2,3,4 have negligible values in the region $\Omega \lesssim -\omega_c$.

Now let us divide the integration in equation (7) into two parts as:

$$M^{(n)}(z) = M_-{}^{(n)}(z)+M_+{}^{(n)}(z)$$

where

$$M_-{}^{(n)}(z) \equiv 2\pi(j)^n \int_{-\infty}^{-\omega_c} F^*(\Omega_2)e^{jk_2z}\, \partial^n[F(\Omega_1)\Gamma e^{-jk_1z}]/\partial\Omega_1{}^n\Big|_{\Omega_1=\Omega_2} d\Omega_2$$

and

$$M_+{}^{(n)}(z) \equiv 2\pi(j)^n \int_{-\omega_c}^{\infty} F^*(\Omega_2)e^{jk_2z}\, \partial^n[F(\Omega_1)\Gamma e^{jk_1z}]/\partial\Omega_1{}^n\Big|_{\Omega_1=\Omega_2} d\Omega_2$$

Then for the reasons stated in the last paragraph, we can approximate $M_-{}^{(n)}(z)$ and $M_+{}^{(n)}(z)$ as

$$M_-^{(n)}(z) \approx 2\pi(j)^n \int_{-\infty}^{\infty} F^*_-(\Omega_2) e^{jk_2 z} \, \partial^n [F_-(\Omega_1) \Gamma e^{-jk_1 z}]/\partial \Omega_1^n \Big|_{\Omega_1=\Omega_2} d\Omega_2 \tag{45}$$

and

$$M_+^{(n)}(z) \approx 2\pi(j)^n \int_{-\infty}^{\infty} F^*_+(\Omega_2) e^{jk_2 z} \, \partial^n [F_-(\Omega_1) \Gamma e^{-jk_1 z}]/\partial \Omega_1^n \Big|_{\Omega_1=\Omega_2} d\Omega_2 \tag{46}$$

If we calculate the partial derivative inside the integrand in equation (45) and use the results in equation (38) through (42) for Γ_0, Γ_1, Γ_2, Γ_3, Γ_4, we can express $M_-^{(n)}(z)$ as a summation of terms which have the general form

$$\int_{-\infty}^{\infty} F^*_-(\Omega_2) (\partial^m F_-(\Omega_2)/\partial \Omega_2^m) g(z,\Omega_2) d\Omega_2 \tag{47}$$

where m is one of 0, 1, 2, 3, 4. In the last integration, $g(z,\Omega_2)$ has the form as

$$g(z,\Omega_2) = B\beta_2{}^h k_2{}^i \left(\frac{\partial k_2}{\partial \Omega_2}\right)^j \left(\frac{\partial^2 k_2}{\partial \Omega_2{}^2}\right)^k \left(\frac{\partial^3 k_2}{\partial \Omega_2{}^3}\right)^\ell \left(\frac{\partial^4 k_2}{\partial \Omega_2{}^4}\right)^m$$

where B is some constant in terms of L, z, A_0, A_2, A_4, A_6 and A_8, and h, i, j, k, ℓ, m are some nonnegative integers. Note that from the expressions for β_2 in equation (11) and k_2 in equation (43), we can find that $g(z,\Omega_2)$ is either an even function or an odd function of ω_2, since $\Omega_2=\omega_2-\omega_c$.

Doing the same thing for $M_+^{(n)}(z)$ in equation (46), we can obtain an identical summation expression for $M_+^{(n)}(z)$ except that the corresponding general expression of (47) becomes

$$\int_{-\infty}^{\infty} F^*_+(\Omega_2) [\partial^m F_+(\Omega_2)/\partial \Omega_2^m] g(z,\Omega_2) d\Omega_2 \tag{48}$$

which just has different spectrum.

For the purpose of further calculation in expressions (47) and (48), we expand $g(z,\Omega_2)$ into a power series in two ways as

$$g(z,\Omega_2) = g_0+g_1\Omega_2+g_2\Omega_2{}^2+ \ldots\ldots \tag{49a}$$

and

$$g(z,\Omega_2) = g_0'+g_1'(\Omega_2+2\omega_c)+g_2'(\Omega_2+2\omega_c)^2+ \ldots \tag{49b}$$

where

$$g_\ell = \frac{1}{\ell!}\frac{\partial^\ell g(z,\Omega_2)}{\partial\Omega_2{}^\ell}\Big|_{\Omega_2=0} \qquad \ell=0,1,2,3, \ldots.$$

and

$$g_\ell' = \frac{1}{\ell!}\frac{\partial^\ell g(z,\Omega_2)}{\partial\Omega_2{}^\ell}\Big|_{\Omega_2=-2\omega_c} \qquad \ell=0,1,2,3, \ldots.$$

note that if $g(z,\Omega_2)$ is even with respect to $\Omega_2=-\omega_c(\omega_2=0)$, $g_\ell=(-1)^\ell g_\ell'$ and if $g(z,\Omega_2)$ is odd with respect to $\Omega_2=-\omega_c$, $g_\ell=(-1)^{\ell+1}g_\ell'$. Having these results, we can rewrite expression (47) as

$$\int_{-\infty}^{\infty} F_-^*(\Omega_2)[\partial^m F_-(\Omega_2)/\partial\Omega_2{}^m]g(z,\Omega_2)d\Omega_2$$

$$= \int_{-\infty}^{\infty} F_-^*(\Omega_2)[\partial^m F_-(\Omega_2)/\partial\Omega_2{}^m][g_0'+g_1'(\Omega_2+2\omega_c)+g_2'(\Omega_2+2\omega_c)^2+ \ldots.]d\Omega_2$$

$$= \int_{-\infty}^{\infty} F_+^*(\Omega_2')[\partial^m F_+(\Omega_2')/\partial\Omega_2'{}^m][g_0'+g_1'\Omega_2'+g_2'\Omega_2'^2 + \ldots.]d\Omega_2' \tag{50}$$

where we have replaced the variable Ω_2 by $\Omega_2'=\Omega_2+2\omega_c$.

On the other hand, using equation (49a) we can also rewrite expression (48) as

$$\int_{-\infty}^{\infty} F_+^*(\Omega_2)(\partial^m F_+(\Omega_2)/\partial\Omega_2^m)g(z,\Omega_2)d\Omega_2$$

$$= \int_{-\infty}^{\infty} F_+^*(\Omega_2)(\partial^m F_+(\Omega_2)/\partial\Omega_2^m)[g_0+g_1\Omega_2+g_2\Omega_2^2+\ldots]d\Omega_2 \tag{51}$$

In the first order calculation, we neglect $g_2'\Omega_2'^2$ term and all higher order terms in equation (50) and neglect $g_2\Omega_2^2$ term and all higher order terms in equation (51). Now, if we change the dummy variable Ω_2' into Ω_2 in equation (50) and add it to equation (51) in both sides, we can conclude that $M^{(n)}(z)=M_-^{(n)}(z)+M_+^{(n)}(z)$ can be approximated by a summation of terms with a general form

$$\int_{-\infty}^{\infty} F_-^*(\Omega_2)(\partial^m F_-(\Omega_2)/\partial\Omega_2^m)g(z,\Omega_2)d\Omega_2 + \int_{-\infty}^{\infty} F_+^*(\Omega_2)(\partial^m F_+(\Omega_2)/\partial\Omega_2^m)g(z,\Omega_2)d\Omega_2$$

$$\triangleq \begin{cases} 2g_0 \int_{-\infty}^{\infty} F_+^*(\Omega_2)(\partial^m F_+(\Omega_2)/\partial\Omega_2^m)d\Omega_2 & \text{if } g(z,\Omega_2) \text{ is even with respect to } \omega_2=0 \text{ and } m \text{ is even} \\ 0 & \text{if } g(z,\Omega_2) \text{ is even with respect to } \omega_2=0 \text{ but } m \text{ is odd} \\ 2g_1 \int_{-\infty}^{\infty} F_+^*(\Omega_2)[\partial^m F_+(\Omega_2)/\partial\Omega_2^m]\Omega_2 d\Omega_2 & \text{if } g(z,\Omega_2) \text{ is odd with respect to } \omega_2=0 \text{ and } m \text{ is odd.} \\ 0 & \text{if } g(z,\Omega_2) \text{ is odd with respect to } \omega_2=0 \text{ but } m \text{ is even} \end{cases}$$

So, in summary, for the purpose of obtaining the formula for the nth moment, we first expand equation (45) and (46) to get summations of terms with general forms in expression (47) and (48) respectively. Then

equation (52) is used to reduce each term into a simple integration form like that given by the right hand side of equation (52). After finishing those simple integrations, we add them up to obtain the formula for the nth moment. In order to shorten those lengthy formulas, we use the notations $X=\omega_p^2/\omega_c 2$ and $Z=1-X$. Those formulas are

$$M^{(0)} = \frac{\sqrt{2\pi}\, T_0}{4} \tag{3}$$

$$M^{(1)}(z)/M^{(0)} = [\frac{z}{c} - \frac{A_2}{4c}(2Lz-L^2)X^2Z^{-2}]Z^{-1/2} \tag{54}$$

$$M^{(2)}(z)/M^{(0)} = \frac{T_0^2}{4} + \frac{z^2}{c^2}Z^{-1} + \frac{A_0 L}{4c^2}X^2Z^{-3} - \frac{A_2}{2c^2}(2Lz^2-L^2z)X^2Z^{-3}$$

$$+ \frac{4A_4}{3\omega_c^2}(3Lz^2-3L^2z+L^3)X^2Z^{-4} + \frac{2A_2^2}{c^2}(\frac{1}{4}L^2z^2 - \frac{7}{24}L^3z + \frac{3}{32}L^4)X^4Z^{-5} \tag{55}$$

$$M^{(3)}(z)/M^{(0)} = \frac{3}{4}\frac{z}{c}T_0^2Z^{-1/2} + \frac{3}{2}\frac{z}{c\omega_c^2}XZ^{-5/2} + \frac{z^3}{c^3}Z^{-3/2}$$

$$+ \frac{3}{4}\frac{Lz}{c^3}A_0X^2Z^{-7/2} - \frac{3T_0^2}{16c}A_2(2Lz-L^2)X^2Z^{-5/2}$$

$$- \frac{3}{4}\frac{z^2}{c^3}A_2(2Lz-L^2)X^2Z^{-7/2} - \frac{A_2}{c\omega_c^2}(2Lz-L^2)X^2(3+\frac{15}{8}X)Z^{-9/2}$$

$$+ \frac{4z}{c\omega_c^2}A_4(3Lz^2-3L^2z+L^3)X^2Z^{-9/2}$$

$$+ \frac{6c}{\omega_c^4}A_6(3L^4-12Lz^3+18L^2z^2-12L^3z)X^2Z^{-11/2}$$

$$+ \frac{6}{c^3}A_2^2(\frac{1}{4}L^2z^3 - \frac{7}{24}L^3z^2 + \frac{3}{32}L^4z)X^4Z^{-11/2}$$

$$- \frac{1}{960c^3}A_2^3(720L^3z^3-1320L^4z^2+846L^5z-185L^6)X^6Z^{-15/2}$$

$$+ \frac{3}{16c^3}A_0A_2(L^3-2L^2z)X^4Z^{-11/2}$$

continued on next page

$$- \frac{1}{c\omega_c^2} A_2A_4(18L^2z^3-31L^3z^2+20L^4z - \frac{23}{5} L^5)X^4Z^{-13/2} \tag{56}$$

$$M^{(4)}(z)/M^{(0)} = \frac{3}{16} T_0^4 + \frac{3z^2}{2c^2} T_0^2 Z^{-1} + \frac{3z^2}{c^2\omega_c^2} X(2+X)Z^{-3}$$

$$+ \frac{z^4}{c^4} Z^{-2} + \frac{3T_0^2}{8c^2} A_0L\, X^2Z^{-3} + \frac{3z^2}{2c^4} A_0L\, X^2Z^{-4}$$

$$+ \frac{A_0L}{c^2\omega_c^2} (6X^2 + \frac{15}{2} X^3 + \frac{3}{4} X^4)Z^{-5}$$

$$+ \frac{3}{16c^4} A_0^2L^2\, X^4Z^{-6} - \frac{3T_0^2}{4c^2} A_2(2Lz^2-L^2z)X^2Z^{-3}$$

$$- \frac{A_2}{c^2\omega_c^2} (2Lz^2-L^2z)(\frac{3}{2} X^4+15X^3+12X^2)\, Z^{-5}$$

$$- \frac{z^3}{c^4} A_2(2Lz-L^2)X^2Z^{-4}$$

$$+ \frac{2T_0^2}{\omega_c^2} A_4(3Lz^2-3L^2z+L^3)X^2Z^{-4}$$

$$+ \frac{8z^2}{c^2\omega_c^2} A_4(3Lz^2-3L^2z+L^3)X^2Z^{-5}$$

$$+ \frac{A_4}{\omega_c^4} (3Lz^2-3L^2z+L^3)Y^2(4X^2+56X+72)Z^{-6}$$

$$+ \frac{3T_0^2}{c^2} A_2^2(\frac{1}{4} L^2z^2 - \frac{7}{24} L^3z + \frac{3}{32} L^4)X^4Z^{-5}$$

$$+ \frac{12z^2}{c^4} A_2^2(\frac{1}{4} L^2z^2 - \frac{7}{24} L^3z + \frac{3}{32} L^4)\, X^4Z^{-6}$$

$$+ \frac{A_2^2}{c^2\omega_c^2} (\frac{3}{8} L^4 - \frac{7}{6} L^3z + L^2z^2)X^4(\frac{3}{2} X^2+27X+48)Z^{-7}$$

$$+\frac{A_2^4}{c^4}\left(\frac{3}{2}L^4z^4-\frac{15}{4}L^5z^3+\frac{871}{240}L^6z^2-\frac{5363}{3360}L^7z+\frac{7217}{26880}L^8\right)X^8Z^{-10}$$

$$-\frac{A_2^3}{c^4}\left(3L^3z^4-\frac{11}{2}L^4z^3+\frac{141}{40}L^5z^2-\frac{37}{48}L^6z\right)X^6Z^{-8}$$

$$+\frac{A_0A_2^2}{c^4}\left(\frac{3}{4}L^3z^2-\frac{7}{8}L^4z+\frac{9}{32}L^5\right)X^6Z^{-8}$$

$$+\frac{24A_4^2}{\omega_c^4}\left(12L^2z^4-28L^3z^3+\frac{82}{3}L^4z^2-\frac{188}{15}L^5z+\frac{20}{9}L^6\right)X^4Z^{-8}$$

$$+\frac{24}{c^2\omega_c^2}A_2^2A_4\left(3L^3z^4-\frac{29}{4}L^4z^3+\frac{337}{48}L^5z^2-\frac{2381}{720}L^6z+\frac{379}{560}L^7\right)X^6Z^{-9}$$

$$+\frac{A_0A_4}{c^2\omega_c^2}\left(6L^2z^2-6L^3z+2L^4\right)X^4Z^{-7}$$

$$+\frac{24}{\omega_c^4}A_2A_6\left(\frac{45}{2}L^2z^4-51L^3z^3+\frac{201}{4}L^4z^2-\frac{243}{10}L^5z+\frac{19}{4}L^6\right)X^4Z^{-8}$$

$$+\frac{24c^2}{\omega_c^6}A_8\left(96Lz^4-192L^2z^3+192L^3z^2-96L^4z+\frac{96}{5}L^5\right)X^2Z^{-7}$$

$$-\frac{24}{\omega_c^4}A_6\left(12Lz^4-18L^2z^3+12L^3z^2-3L^4z\right)X^2Z^{-6}$$

$$-\frac{3}{4c^4}A_0A_2\left(2L^2z^2-L^3z\right)X^4Z^{-6}$$

$$-\frac{4}{\omega_c^2c^2}A_2A_4\left(18L^2z^4-31L^3z^3+20L^4z^2-\frac{23}{5}L^5z\right)X^4Z^{-7} \qquad (57)$$

In order to understand the physical significance to these moments, we shift the origin of time to $M^{(1)}/M^{(0)}$, which will be defined to be the arrival time of the signal in Chapter 3. We call the new moments the central moments. They are denoted by $\bar{M}^{(n)}$ and are given by

$$\bar{M}^{(n)}(z) = \int_{-\infty}^{\infty} \left(t - \frac{M^{(1)}}{M^{(0)}}\right)^n \langle A^*(z,t)A(z,t)\rangle dt = \sum_{j=0}^{n} \frac{n!}{j!(n-j)!} \left(-\frac{M^{(1)}}{M^{(0)}}\right)^{n-j} M^{(j)}$$

$$n=0,1,2, \ldots.$$

(58)

We note $\bar{M}^{(0)}=M^{(0)}$ and $\bar{M}^{(1)}=0$. The calculations of higher order central moments follow in a straightforward manner by using (58) to give

$$\bar{M}^{(2)}(z)/M^{(0)} = \frac{T_0^2}{4} + \frac{A_0 L}{4c^2} X^2 Z^{-3} + \frac{4A_4}{3\omega_c^2} (3Lz^2 - 3L^2 z + L^3) X^2 Z^{-4}$$

$$+ \frac{A_2^2}{c^2} \left(\frac{1}{4} L^2 z^2 - \frac{1}{3} L^3 z + \frac{1}{8} L^4\right) X^4 Z^{-5} \tag{59}$$

$$\bar{M}^{(3)}(z)/M^{(0)} = \frac{3z}{2c\omega_c^2} X Z^{-5/2} - \frac{A_2}{8c\omega_c^2} (2Lz - L^2) X^2 (24+15X) Z^{-9/2}$$

$$- \frac{6cA_6}{\omega_c^4} (12Lz^3 - 18L^2 z^2 + 12L^3 z - 3L^4) X^2 Z^{-11/2}$$

$$- \frac{A_2 A_4}{c\omega_c^2} \left(12L^2 z^3 - 22L^3 z^2 + 15L^4 z - \frac{18}{5} L^5\right) X^4 Z^{-13/2}$$

$$- \frac{A_2^3}{c^3} \left(\frac{1}{4} L^3 z^3 - \frac{1}{2} L^4 z^2 + \frac{7}{20} L^5 z - \frac{1}{12} L^6\right) X^3 Z^{-15/2} \tag{60}$$

$$\bar{M}^{(4)}(z)/M^{(0)} = \frac{3}{16} T_0^4 + \frac{3z^2}{c^2\omega_c^2} X^2 Z^{-3} + \frac{3T_0^2}{8c^2} A_0 L X^2 Z^{-3}$$

$$+ \frac{A_0 L}{c^2\omega_c^2} \left(6X^2 + \frac{15}{2} X^3 + \frac{3}{4} X^4\right) Z^{-5}$$

$$+ \frac{3}{16c^2} A_0^2 L^2 X^4 Z^{-6} - \frac{A_2}{c^2\omega_c^2} (2Lz^2 - L^2 z) \left(\frac{3}{2} X^4 + 6X^3\right) Z^{-5}$$

continued on next page

$$+\frac{A_0A_2^2}{c^4}\left(\frac{3}{8}L^3z^2-\frac{1}{2}L^4z+\frac{3}{16}L^5\right)X^6Z^{-8}$$

$$+\frac{2T_0^2}{\omega_c^2}A_4(3Lz^2-3L^2z+L^3)X^2Z^{-4}$$

$$+\frac{A_4}{\omega_c^4}(3Lz^2-3L^2z+L^3)X^2(4X^2+56X+72)Z^{-6}$$

$$+\frac{T_0^2}{c^2}A_2^2\left(\frac{3}{8}L^2z^2-\frac{1}{2}L^3z+\frac{3}{16}L^4\right)X^4Z^{-5}$$

$$+\frac{A_2^2}{c^2\omega_c^2}\left[\left(\frac{3}{8}L^4-\frac{7}{6}L^3z+L^2z^2\right)\left(\frac{3}{2}X^2-3X\right)\right.$$

$$\left.+\left(\frac{5}{8}L^4-\frac{11}{6}L^3z+\frac{3}{2}L^2z^2\right)(24+15X)\right]X^4Z^{-7}$$

$$+\frac{A_2^4}{c^4}\left(\frac{15}{16}L^4z^4-\frac{3}{2}L^5z^3+\frac{373}{240}L^6z^2-\frac{217}{210}L^7z+\frac{301}{2240}L^8\right)X^8Z^{-10}$$

$$+\frac{24A_4^2}{\omega_c^4}\left(12L^2z^4-28L^3z^3+\frac{82}{3}L^4z^2-\frac{188}{15}L^5z+\frac{20}{9}L^6\right)X^4Z^{-8}$$

$$+\frac{A_0A_4}{c^2\omega_c^2}(6L^2z^2-6L^3z+2L^4)X^4Z^{-7}$$

$$+\frac{A_2^2A_4}{c^2\omega_c^2}\left(42L^3z^4-106L^4z^3+107L^5z^2-\frac{161}{3}L^6z+\frac{85}{7}L^7\right)X^6Z^{-9}$$

$$+\frac{24c^2}{\omega_c^6}A_8\left(96Lz^4-192L^2z^3+192L^3z^2-96L^4z+\frac{96}{5}L^5\right)X^2Z^{-7}$$

$$+\frac{A_2A_6}{\omega_c^4}\left(396L^2z^4-936L^3z^3+954L^4z^2-\frac{2376}{5}L^5z+96L^6\right)X^4Z^{-8}$$

(61)

3. Temporal Moments and Numerical Results

In this chapter, we give the physical meanings to those moments. The first moment and the second central moment have the physical significance as the mean arrival time and the mean square width of the received signal. Then the skewness and kurtosis are defined in terms of the second, third and fourth central moments. These quantities are used to describe the rough shape of the signal. In order to get more concrete understanding, we assume that the turbulence has the power spectrum introduced by Shkarofsky. Then two sets of parameters are used to obtain the numerical results. These parameters describe the geometry and content of the medium. All of them are stated in Section 3.1.

3.1 Mean Arrival Time and Mean Pulse Width

The first moment and second central moment have been evaluated and discussed by many papers in the past [Mark, 1972; Yeh and Yang, 1977c; Liu and Yeh, 1977; Yeh and Liu, 1977b; Yeh and Liu, 1979]. The first moment represents the time position of the energy weighted by the intensity distribution. Therefore it is just the arrival time of the signal. Here we rewrite the first moment expression in equation (54) and denote t_a as the arrival time of the signal. So we have

$$t_a \equiv M^{(1)}(z)/M^{(0)} = z/v_g - \frac{A_2}{4c}(2Lz-L^2)X^2Z^{-5/2} \qquad (62)$$

where we have replaced $cZ^{1/2}$ by v_g, the group velocity. Obviously the first term in the equation above represents the arrival time if there were no random irregularities in the medium. The second term is the excess time due to dispersion and random scattering. Here we have to note that A_2 is always negative, then the excess time is always positive.

Since the second term depends on X^2, the excess time decreases rapidly as the carrier frequency increases.

Now for further calculation, we introduce a power spectrum for the random turbulence which was presented first by Shkarofsky [1968]:

$$\Phi_\xi(\kappa) = \frac{(\kappa_0 \ell_0)^{(p-3)/2} \ell_0^3}{(2\pi)^{3/2} K_{(p-3)/2}(\kappa_0 \ell_0)} \cdot \frac{K_{p/2}(\ell_0 \sqrt{\kappa^2+\kappa_0^2})}{(\ell_0 \sqrt{\kappa^2+\kappa_0^2})^{p/2}} \cdot \sigma_\xi^2 \tag{63}$$

where K is the Hankel function of imaginary argument and $\kappa_0 = 1/L_0$. The quantities L_0 and ℓ_0 are the outer and inner scales, respectively. σ_ξ^2 is the variance of the relative electron density fluctuation. The two-dimensional correlation function corresponding to the three dimensional spectrum defined by (63) is given by

$$A_\xi(\rho) = \frac{2\pi(\kappa_0 \sqrt{\rho^2+\ell_0^2})^{(p-2)/2} K_{(p-2)/2}(\kappa_0 \sqrt{\rho^2+\ell_0^2}) \sigma_\xi^2}{\kappa_0 (\kappa_0 \ell_0)^{(p-3)/2} K_{(p-3)/2}(\kappa_0 \ell_0)} \tag{64}$$

When $A_\xi(\rho)$ is expanded as in equation (37), the coefficient A_n, n=0,2,4, ... etc., can be easily obtained from the relation $A_n = \frac{1}{n!} \frac{\partial^n A(\rho)}{\partial \rho^n} \Big|_{\rho=0}$, yielding

$$A_0 = \sqrt{2\pi \ell_0/\kappa_0}\, \sigma_\xi^2\, K_{(p-2)/2}(\kappa_0 \ell_0)/K_{(p-3)/2}(\kappa_0 \ell_0) \tag{65}$$

$$A_2 = -\sqrt{\pi \kappa_0/2\ell_0}\, \sigma_\xi^2\, K_{(p-4)/2}(\kappa_0 \ell_0)/K_{(p-3)/2}(\kappa_0 \ell_0) \tag{66}$$

$$A_4 = \sqrt{\pi \kappa_0^3/2^5 \ell_0^3}\, \sigma_\xi^2\, K_{(p-6)/2}(\kappa_0 \ell_0)/K_{(p-3)/2} \tag{67}$$

$$A_6 = -\sqrt{\pi\kappa_0^5/9\cdot 2^7\ell_0^5}\ \sigma_\xi^2\ K_{(p-8)/2}(\kappa_0\ell_0)/K_{(p-3)/2}(\kappa_0\ell_0) \tag{68}$$

$$A_8 = \sqrt{\pi\kappa_0^7/9\cdot 2^{13}\ell_0^7}\ \sigma_\xi^2\ K_{(p-10)/2}(\kappa_0\ell_0)/K_{(p-3)/2}(\kappa_0\ell_0) \tag{69}$$

.....

For numerical results, we take L_0=10 kilometers and ℓ_0=10 meters and σ_ξ^2=0.1. Furthermore we use two sets of parameters which are listed as follows:

		Model 1	Model 2
Plasma frequency	f_p	10 MHz	50 MHz
Distance	z	500 km	1000 km
Width of random irregularity slab	L	200 km	500 km

where Model 1 corresponds to conditions that can occur naturally in the equatorial ionosphere and Model 2 corresponds to conditions of an ionosphere disturbed by nuclear explosions. In our calculations the carrier frequency f_c will be varied. The width of the impressed pulse is T_0 and is also varied such that $f_c T_0$ =100, which is consistent with the assumption made in the derivation of the temporal moments in Section 2.4.

In Figure 2 we present the numerical results for the arrival time. The excess time, $t_a - z/v_g$, is plotted as a function of the carrier frequency for both Model 1 and Model 2. Except in the region $f_c \lesssim 300$ MHz in Model 2, these two straight lines in this figure show that the excess times are proportional to f_c^{-4} in both models. The little digression at low carrier frequency end in Model 2 comes from the failure of the approximation $Z \gg 1$.

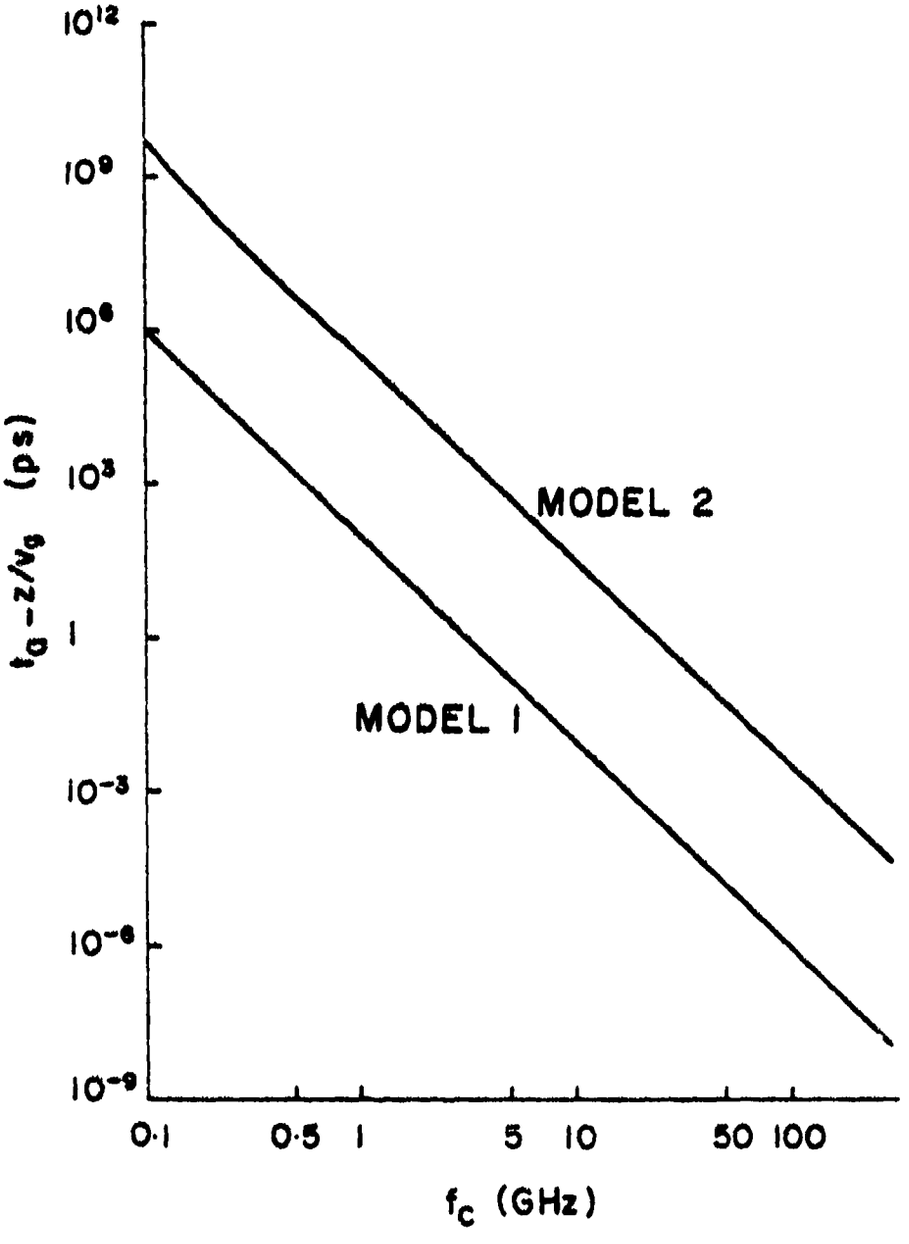

Figure 2. Excess time $t_a - z/v_g$ as a function of the carrier frequency. Except a small portion of the curve at the low frequency end in Model 2, the two parallel straight lines indicate a f_c^{-4} dependence.

Now let's look at the second central moment given by equation (59). It has been identified earlier as the mean square pulse width of the signal. Denote the square root of it by τ. So we have

$$\tau^2 \equiv \bar{M}^{(2)}(z)/M^{(0)} = \frac{T_0^2}{4} + \frac{A_0 L}{4c^2} X^2 Z^{-3} + \frac{4A_4}{3\omega_c^2} (3Lz^2 - 3L^2 z + L^3) X^2 Z^{-4}$$

$$+ \frac{A_2^2}{c^2} (\frac{1}{4} L^2 z^2 - \frac{1}{3} L^3 z + \frac{1}{8} L^4) X^4 Z^{-5} \qquad (70)$$

It is easy to recognize that the first term of the expression above is the original square width. The other terms contribute to the broadening of the signal due to random scattering and dispersion. But in equation (70) the distortion terms that come from the high order dispersion are absent. The reason for this is that we have neglected $g_2\Omega^2$ term and all higher ones in equation (49). Actually, the general expressions (47) and (48) contains the effects due to higher order dispersion. If in those terms we take Ω_2^2 term in equation (49) into account for the calculations of $M^{(1)}$ and $M^{(2)}$, an extra term $(z^2/c^2\omega_c^2 T_0^2)X^2Z^{-3}$ must be added to the right hand side of equation (70). This quantity describes the signal broadening if there are no random irregularities in the medium. Using the numerical values in either Model 1 or Model 2, we find this quantity is much smaller than any distortion term in equation (70) due to scattering and hence the higher order dispersion term can be ignored.

The dependence of the normalized mean pulse width $\tau/(T_0/2)$ on the carrier frequency is shown in Figure 3. In the frequency range we consider, when the carrier frequency is larger than 500 MHz for Model 1 and that is larger than 10 GHz for Model 2, the first term in equation (70) dominates and we can neglect all the broadening effects.

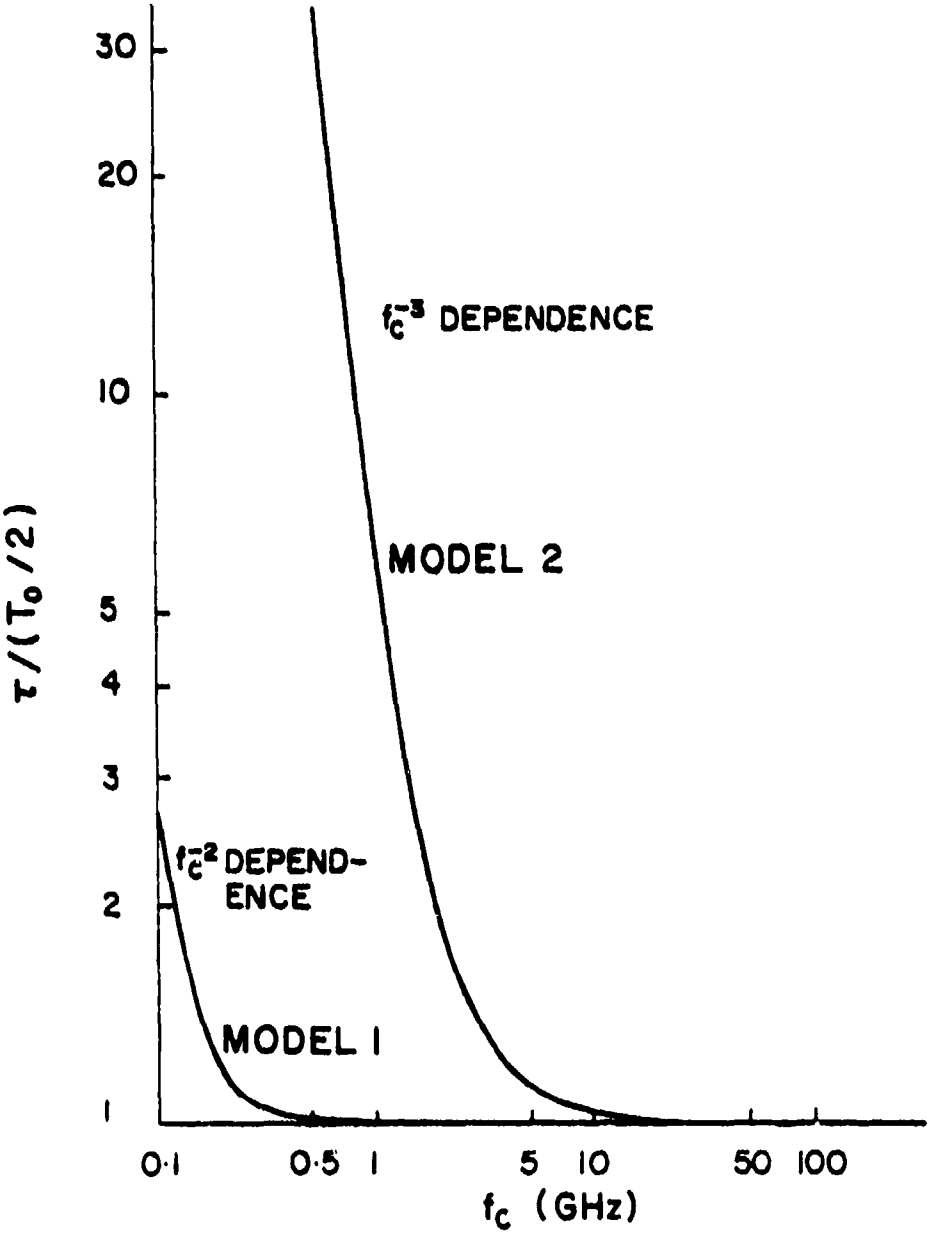

Figure 3. Normalized mean pulse width $\tau/(T_0/2)$ as a function of the carrier frequency.

In Model 1, on the other hand, if the carrier frequency is between 100 MHz and 140 MHz, the term containing A_4, which has f_c^{-6} dependence, is most important. In some earlier papers [Sreenivasiah, 1976; Leader, 1979; etc.] $A_\xi(\vec{\rho})$ in equation (37) is approximated by $A_0+A_2\rho^2$. With this approximation, they would miss the A_4 term which happens to be dominating under the condition above. Then their results will be in error when applied to our problem. In Model 2, when the carrier frequency f_c is such that 100 MHz $\leq f_c \leq$ 1 GHz, the last term in equation (70) is most important and we can approximate τ^2 as

$$\tau^2 \simeq \frac{A_2^2}{c^2}\left(\frac{1}{4}L^2z^2-\frac{1}{3}L^3z+\frac{1}{8}L^4\right)X^4Z^{-5} \tag{71}$$

which has f_c^{-8} dependence. Note that under this condition, the normalized mean pulse width $\tau/(T_0/2)$, is proportional to f_c^{-3} since in all computations we assume $\omega_c T_0=100$.

3.2 The Third Moment and Skewness

Let us rewrite the third central moment given by equation (60) as

$$\begin{aligned}\bar{M}^{(3)}(z)/M^{(0)} = {} & \frac{3z}{2c\omega_c^2}XZ^{-5/2}-\frac{A_2}{8c\omega_c^2}(2Lz-L^2)X^2(24+15X)Z^{-9/2} \\ & -\frac{6cA_6}{\omega_c^4}(12Lz^3-18L^2z^2+12L^3z-3L^4)X^2Z^{-1/2} \\ & -\frac{A_2A_4}{c\omega_c^2}\left(12L^2z^3-22L^3z^2+15L^4z-\frac{18}{5}L^5\right)X^4Z^{-13/2} \\ & -\frac{A_2^3}{c^3}\left(\frac{1}{4}L^3z^3-\frac{1}{2}L^4z^2+\frac{7}{20}L^5z-\frac{1}{12}L^6\right)X^6Z^{-15/2}\end{aligned} \tag{72}$$

The first term on the right hand side of (72) comes from dispersion and all the remaining terms from random scattering. Note that A_2 and A_4

are always negative and A_4 is positive. This implies that the third central moment is always positive. Physically, this means that due to propagation effects the pulse becomes asymmetrical with a trailing edge longer than the leading edge. If under certain conditions the third central moment becomes large, the received pulse must be then stretched to give a long tail. Therefore, the value of the third central moment is a measure of asymmetry of the pulse relative to the arrival time.

In Figure 4, we present the dependence of the third central moment on carrier frequency for two models. In Model 1, when the carrier frequency f_c is larger than 3 GHz, the first term in equation (72) dominates, so that

$$\bar{M}^{(3)}(z)/M^{(0)} \simeq \frac{3z}{2c\omega_c^2} X Z^{-5/2}$$

indicating that the dispersion is more important and the third moment has f_c^{-4} dependence. When $f_c \leq 1$ GHz, the third term dominates,

$$\bar{M}^{(3)}(z)/M^{(0)} \simeq \frac{-6cA_6}{\omega_c^4} (12Lz^3-18L^2z^2+12L^3z-3L^4)X^2Z^{-11/2}$$

indicating that the random scattering is more important and this moment is proportional to f_c^{-8}. In Model 2, when the carrier frequency is above 10 GHz, the term owing to dispersion effect dominates again. But when f_c is below 10 GHz, no term can always dominate.

Let us now define the skewness, s, through the following relation:

$$\bar{M}^{(3)}(z)/M^{(0)} = s\tau^3 \tag{73}$$

The value of s is a measure of the extent of the signal asymmetry. If the signal intensity distribution is symmetric about the arrival time, s is

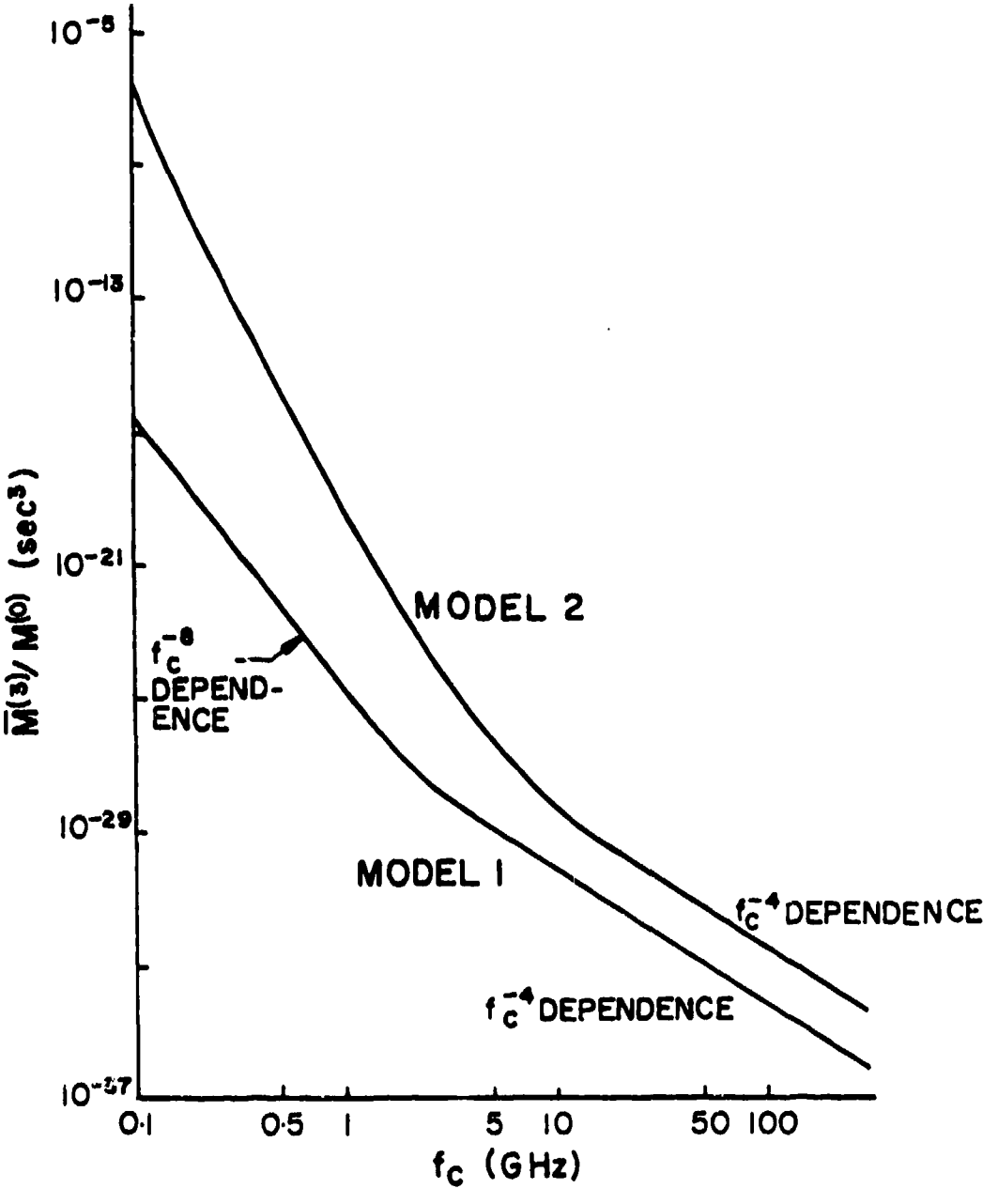

Figure 4. Normalized third central moment, $\bar{M}^{(3)}/M^{(0)}$, as a function of the carrier frequency f_c.

zero. Roughly speaking, larger s means bigger relative difference of the stretched lengths between the trailing edge and the leading edge. In Figure 5, we show a distribution with an exponential decay in trailing edge and a Gaussian decay in leading edge. This distribution has skewness s=1.03. If any distribution has s value much smaller than unity, we may conclude that any of the following three possibilities may happen: 1) the trailing edge decays faster than the exponential decay; 2) the leading edge decays slower than the Gaussian decay; 3) both of above. With the distribution shown in Figure 5, this comparison of the s values will give us a coarse idea about the shape of the received signal.

The dependence of skewness on the carrier frequency is shown in Figure 6 for both models. In Model 2, when the carrier frequency f_c is below about 800 MHz, s has nearly a constant value of 2. When f_c is between 1.5 GHz and 10 GHz, s is proportional to f_c^{-5} and when f_c is above 15 GHz, s is a linear function of f_c^{-1}. In Model 1, except the horizontal part, the curve is roughly parallel to that of Model 2. When f_c is such that 200 MHz$\leq f_c \leq$2 GHz, s is proportional to f_c^{-5} and when f_c is above 4 GHz, s is inversely proportional to f_c again. Note that if the carrier frequency is above 500 MHz for Model 1 and is above 3 GHz for Model 2, the values of s are much smaller than 1. So we can say in those frequency ranges the received signals must be less asymmetric than the distribution shown in Figure 5, if by some other means we can make sure that the signal is in a single clump.

3.3 The Fourth Moment and Kurtosis

The formula of the fourth central moment is given in equation (61). Note that since every term in the right hand side is nonnegative, the fourth central moment is nonnegative as it should be. Again, the first

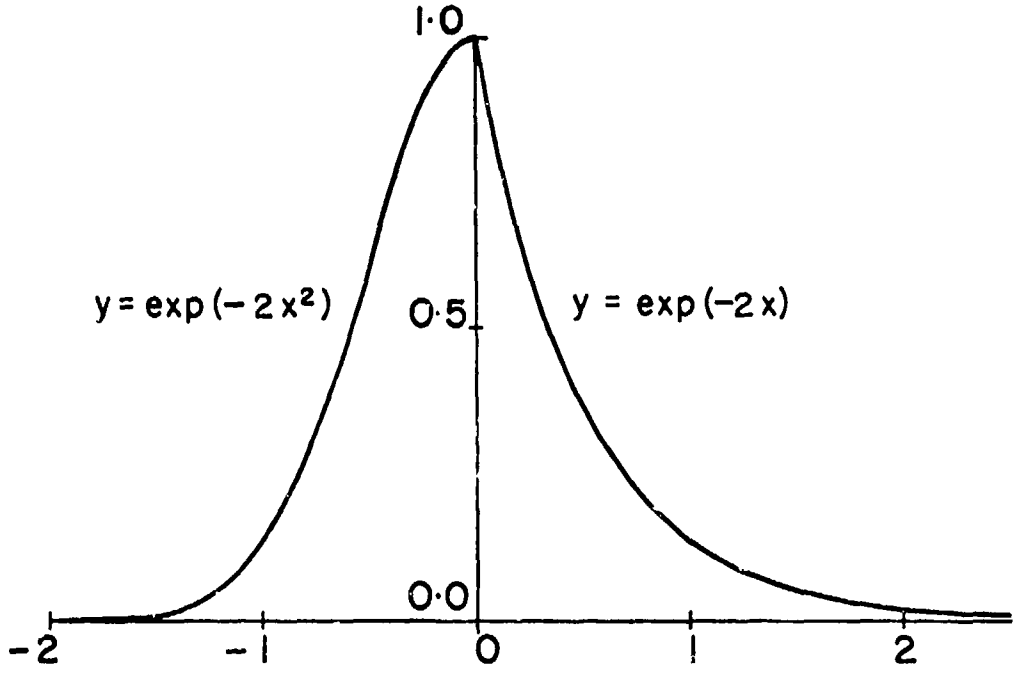

Figure 5. A distribution with an exponential decay in the trailing edge and an Gaussian decay in the leading edge. It has skewness 1.03 and kurtosis 2.94. Note that we have chosen the origin of the horizontal axis to make $\overline{M}^{(1)}=0$.

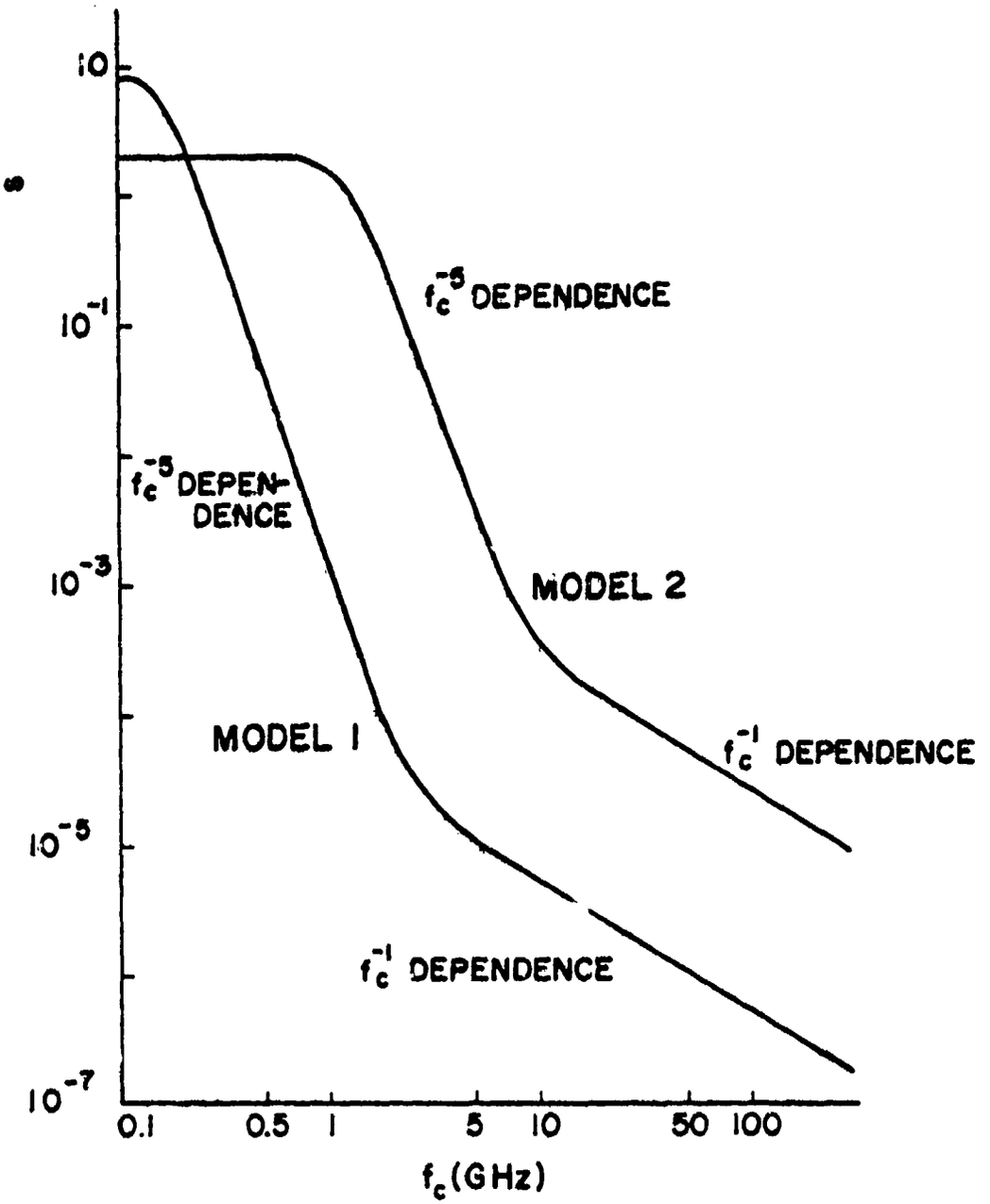

Figure 6. Skewness s as a function of the carrier frequency f_c. For a definition of s, see equation (73) in the text.

term is the original fourth central moment and all the others come from the propagation effects due to dispersion and random scattering. We plot $\bar{M}^{(4)}(z)/M^{(0)}$ as a function of carrier frequency in Figure 7. Quite similar to the situation of the second central moment, when f_c is above 1 GHz in Model 1 and is above 10 GHz in model 2, the first term in equation (61) dominates and we can omit all the propagation effects. On the other hand, in Model 1 when f_c is below 500 MHz, the fourth central moment is proportional to f_c^{-10} and it can be approximated by the single term containing A_8. In model 2, when the carrier frequency is between 200 MHz and 1 GHz, this moment is roughly proportional to f_c^{-16}, i.e., the term including A_2^4 is most important.

Now we define the kurtosis, denoted by K, from the following relation:

$$\bar{M}^{(4)}(z)/M^{(0)} = \tau^4(K+3) \tag{74}$$

where τ is the mean pulse width defined before. The kurtosis is a dimensionless measure of the distribution concentration extent. For the distribution shown in Figure 5, the value of K is 2.94. If any other one clump distribution has kurtosis value less than 2.94, it must be more concentrated than the distribution shown in Figure 5.

In Figure 8, we show the dependences of K on the carrier frequency for both models. Note that both curves have the same shapes as the corresponding ones in Figure 6. Notice also that K is always larger than 0, which is the case without any propagation effect. In Model 2, when the carrier frequency is below 3 GHz, K has nearly a constant value of 30. When the carrier frequency is above 700 MHz for Model 1 and is above 4 GHz for Model 2, the values of kurtosis are less than 2.94. This

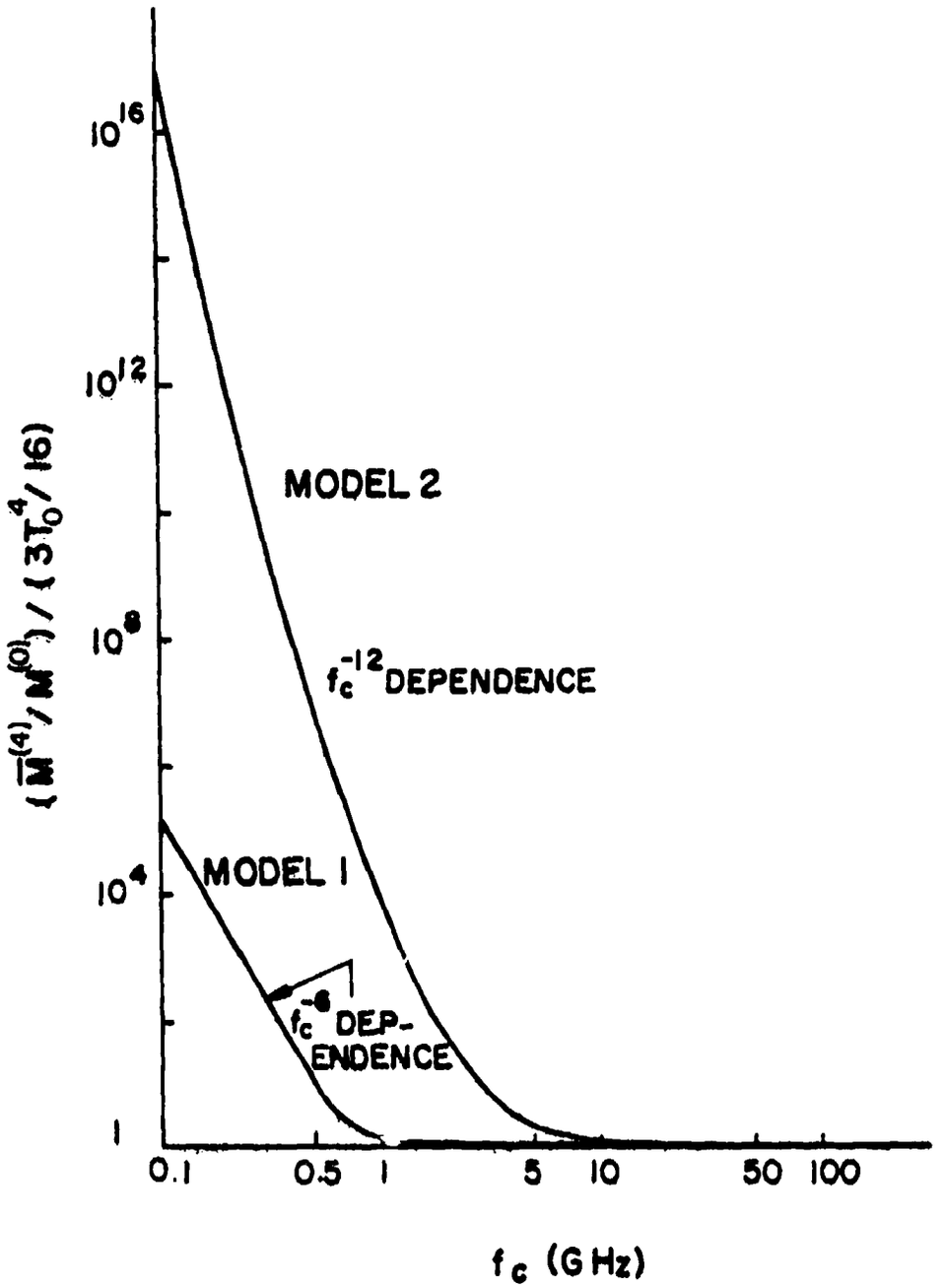

Figure 7. Normalized fourth central moment $(\bar{M}^{(4)}/M^{(0)})/(3T_0^4/16)$ as a function of the carrier frequency f_c.

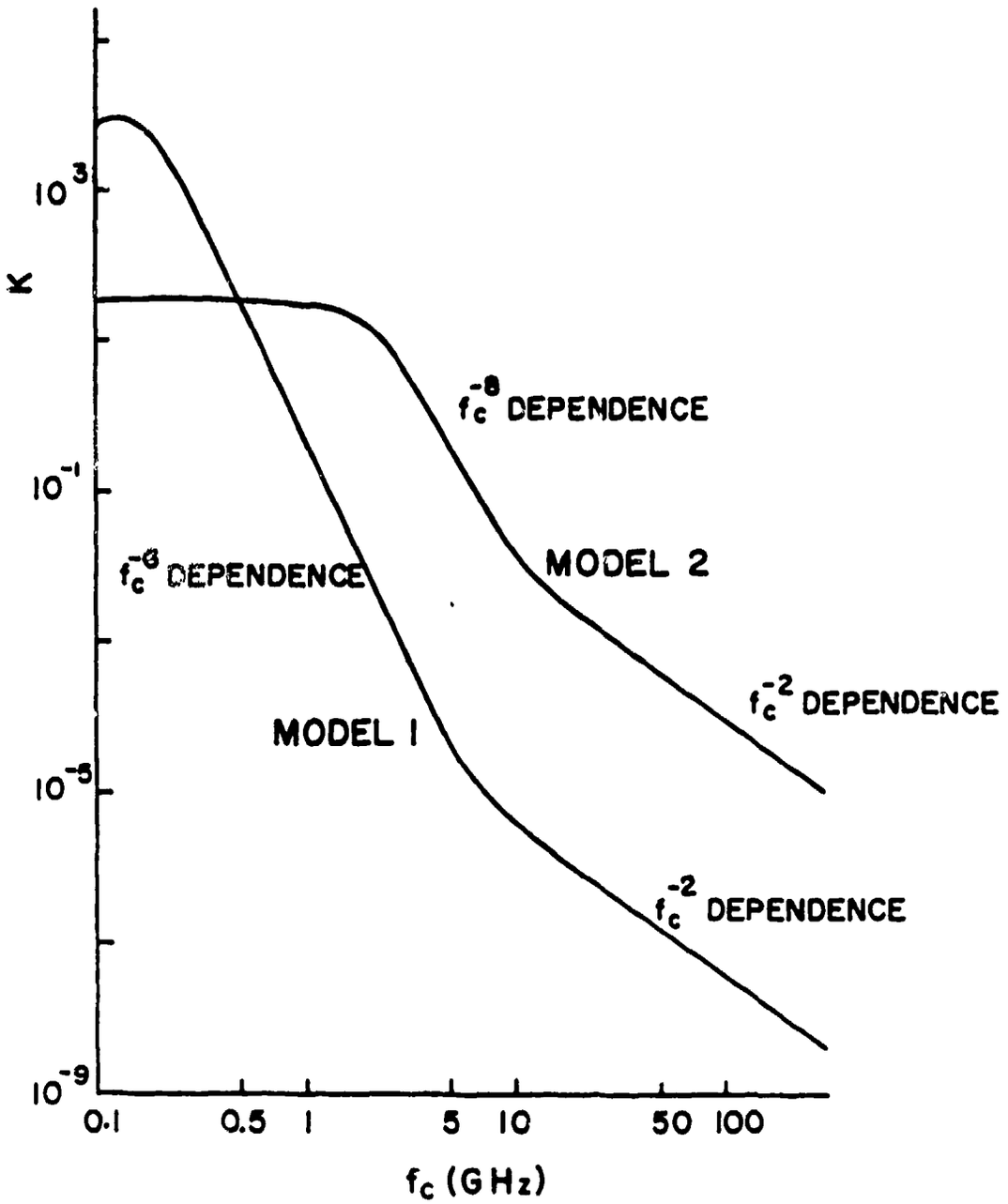

Figure 8. Kurtosis K as a function of the carrier frequency f_c. For a definition K, see equation (74) in the text.

implies that in those frequency ranges the received signal intensity must be more concentrated. So we can conclude that in those frequency ranges the signal must decay faster than the exponential decay on both sides if we assume the received signal is just in a single clump.

4. Description of the Signal Tail

In many applications we are not concerned with the detailed and exact shape of a propagating signal, such as in binary communication. The important thing we like to know is whether an error will be committed in the decoding process owing to the distortion of the signal. From the results in previous chapters, we know the distortions due to propagation effects can be described in two separate ways. One of them is the broadening of a pulse. The other is the asymmetry of this pulse, which when transmitted was originally symmetric. In this latter aspect, we find the distorted signal always has a longer trailing edge. When serious, the received signal cannot be contained in its original bit, it will extend its energy into the next bit or even the third bit. This may produce errors in the decision making process for the neighboring bits. Since in a binary communication link, we mainly worry about the possibility of committing the errors, it is important to estimate the energy quantity which is extended outside of the original bit itself, especially in the trailing edge.

We introduce two theorems about moments first in this chapter. Then these two theorems will be used tc give an upper bound for the signal energy outside some time interval from the arrival time in the trailing edge. The parameter values of those two models in the last chapter will be used again for the numerical results.

4.1 Two Theorems About Moments

Since we are dealing with the normalized signal intensity distribution, this distribution density as a function of time is always positive and the total distribution can be normalized to unity. These properties

satisfy the conditions for a function to be a probability distribution density function. So, any theorem about the moments of the probability distribution as a function of random variable can be cited in our research, if these moments are defined in the same ways as the temporal moments. Here let us introduce two theorems about the moments of the probability distribution. These two theorems can be found in books on statistics, for example, the book written by Mises [1964]. In the following statements, we will not distinguish the probability distribution from the signal intensity distribution, since the results have no difference.

Theorem 1: If two distributions with distribution density function $I(\chi)$ and $I'(\chi)$ have the same moments up to the nth order, the graphs of the corresponding cumulative distribution functions $\varepsilon(\chi)$ and $\varepsilon'(\chi)$ must have at least n "points of intersection".

Note that the cumulative distribution functions and the distribution density functions are related by

$$\varepsilon(\chi) = \int_{-\infty}^{\chi} I(\chi')\, d\chi'$$

Here we have to give a definition to "a point of intersection". We define "a point of intersection" as that inside some closed interval of χ where $\varepsilon(\chi)=\varepsilon'(\chi)$ and just outside this interval $\varepsilon(\chi)-\varepsilon'(\chi)$ has opposite signs in the positive side and negative side.

In this report, we will not try to prove this theorem. But from Theorem 1, it is easy to derive the following Theorem 2.

Theorem 2: Suppose there exists a distribution $I(\chi)$ which has an m-step increasing cumulative distribution function $\varepsilon(\chi)$ and has first 2m order moments $\bar{M}^{(0)}$, $\bar{M}^{(1)}$, $\bar{M}^{(2)}$, ..., $\bar{M}^{(2m-1)}$.

If $I'(\chi)$ is any other distribution with the same 2m moments as above, then the graph of its cumulative distribution function $\epsilon'(\chi)$ passes through each "step" and each "riser" of this m-step function $\epsilon(\chi)$.

As an example, we show a 3-step case in Figure 9. In this figure, for the purpose of our application we have replaced the variable χ by t and denote the positions of the "risers" by t_1, t_2, t_3 and the heights of the respective riser by ϵ_1, ϵ_2, ϵ_3. Note that ϵ_1, ϵ_2, ϵ_3 must be positive and the moments up to fifth order are concerned. Since in the statements of Theorem 2, we have used the central moments to specify the m-step increasing function, the origin of the horizontal axis is the arrival time of the signal.

But for given moments $\bar{M}^{(0)}$, $\bar{M}^{(1)}$, $\bar{M}^{(2)}$, ..., $\bar{M}^{(2m-1)}$, such an m-step increasing cumulative distribution function can exist only when some conditions are satisfied. For the case m=3, these conditions are

$$\bar{M}^{(0)} > 0, \qquad \begin{vmatrix} \bar{M}^{(0)} & \bar{M}^{(1)} \\ \bar{M}^{(1)} & \bar{M}^{(2)} \end{vmatrix} > 0, \qquad \begin{vmatrix} \bar{M}^{(0)} & \bar{M}^{(1)} & \bar{M}^{(2)} \\ \bar{M}^{(1)} & \bar{M}^{(2)} & \bar{M}^{(3)} \\ \bar{M}^{(2)} & \bar{M}^{(3)} & \bar{M}^{(4)} \end{vmatrix} > 0$$

4.2 Application of Those Theorems

In the case of a 3-step function stated above, for the purpose of calculating the positions and heights of "risers", i.e., t_1, t_2, t_3, ϵ_1, ϵ_2, ϵ_3 (6 unknowns) in Figure 9, the quantities of moments up to fifth order (6 knowns) are needed. But, if we have the information of only up to fourth moment, we still can construct a 3-step increasing

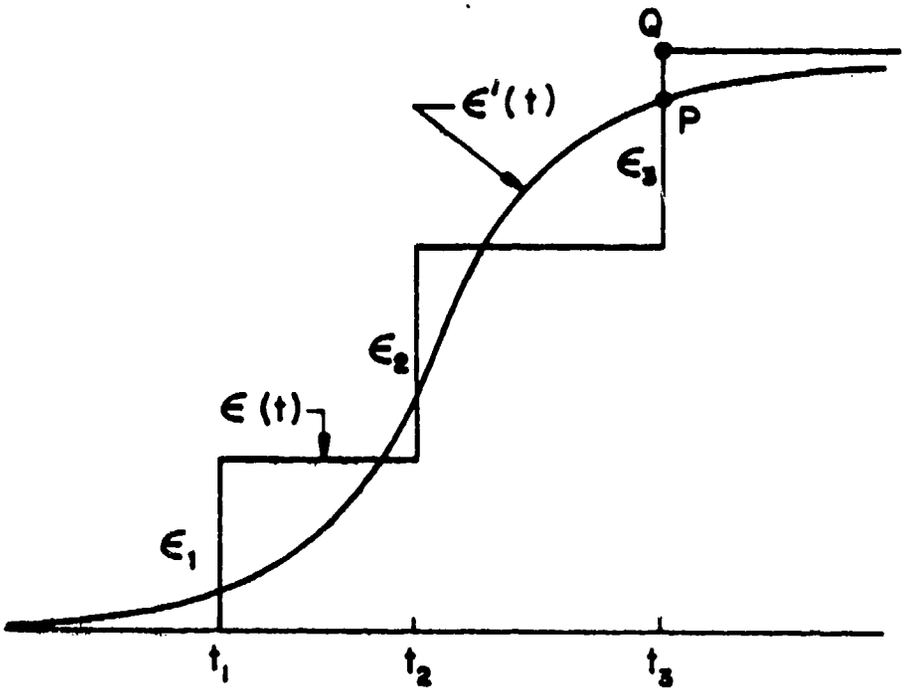

Figure 9. A 3-step function and a increasing curve whose corresponding distribution density functions have the same moments up to fifth order. ϵ_i represents the height of the "riser" at t_i, i=1,2,3. Note that $\epsilon_1+\epsilon_2+\epsilon_3=1$. In this case, these two curves have at least five "points of intersection". Since the height between point P and Q is the fractional signal energy beyond t_3, ϵ_3 is an upper bound of this fractional energy.

function except that any one of t_1, t_2, t_3, ε_1, ε_2, ε_3, must be left undetermined. This undetermined one can be chosen arbitrarily within some restricted ranges.

The conditions under which such a 3-step increasing function can exist have been listed at the end of Section 4.1. They can be satisfied if the cumulative distribution function of our signal intensity distribution is increasing (not constant) at least at 3 points. This is true, since the signal intensity is monotonically increasing at least in some range of time. The proof for the satisfaction of those conditions can be seen just by reviewing the process of deriving those conditions, which we omitted.

Since we are trying to estimate the signal energy outside some time interval from the arrival time in the trailing edge, among t_1, t_2, t_3, ε_1, ε_2, ε_3 we will let t_3 unfixed. Now let us compute t_1, t_2, ε_1, ε_2, ε_3 in terms of t_3, τ, s, K. The starting point of the calculation is the equivalence of those moments between our signal intensity distribution and the distribution with 3-step increasing cumulative distribution function $\varepsilon(t)$. The corresponding distribution density function I(t) of $\varepsilon(t)$ can be expressed by a sum of delta functions as

$$I(t) = \varepsilon_1\delta(t-t_1)+\varepsilon_2\delta(t-t_2)+\varepsilon_3\delta(t-t_3) \tag{75}$$

Then we have relations as follows:

$$\begin{aligned} \bar{M}^{(0)}/\bar{M}^{(0)} &= \varepsilon_1+\varepsilon_2+\varepsilon_3 \\ &= 1 \end{aligned} \tag{76}$$

$$\begin{aligned} \bar{M}^{(1)}/\bar{M}^{(0)} &= \varepsilon_1 t_1+\varepsilon_2 t_2+\varepsilon_3 t_3 \\ &= 0 \end{aligned} \tag{77}$$

$$\bar{M}^{(2)}/\bar{M}^{(0)} = \varepsilon_1 t_1^2+\varepsilon_2 t_2^2+\varepsilon_3 t_3^2$$
$$= \tau^2 \tag{78}$$

$$\bar{M}^{(3)}/\bar{M}^{(0)} = \varepsilon_1 t_1^3+\varepsilon_2 t_2^3+\varepsilon_3 t_3^3$$
$$= \tau^3 s \tag{79}$$

$$\bar{M}^{(4)}/\bar{M}^{(0)} = \varepsilon_1 t_1^4+\varepsilon_2 t_2^4+\varepsilon_3 t_3^4$$
$$= \tau^4(K+3) \tag{80}$$

From equation (75), (76) and (77), it is easy to solve ε_1, ε_2, ε_3 in terms of t_1, t_2, t_3. The results are

$$\varepsilon_1 = \frac{\tau^2+t_2t_3}{(t_3-t_1)(t_2-t_1)} \tag{81}$$

$$\varepsilon_2 = \frac{\tau^2+t_1t_3}{(t_3-t_2)(t_1-t_2)} \tag{82}$$

$$\varepsilon_3 = \frac{\tau^2+t_1t_2}{(t_1-t_3)(t_2-t_3)} \tag{83}$$

Substituting these results in equations (79) and (80), we can obtain the expressions for t_1, t_2 in terms of t_3, τ, s and K. They are as follows:

$$t_1 = \frac{p-\sqrt{p^2-4q}}{2} \tag{84}$$

$$t_2 = \frac{p+\sqrt{p^2-4q}}{2} \tag{85}$$

where

$$p = \frac{\tau^2 t_3(K+2)+\tau^3 s-t_3^2 s\tau}{\tau^2+t_3\tau s-t_3^2} \tag{86}$$

$$\varsigma = \frac{\tau^2[\tau^2 s^2 - t_3 \tau s - \tau^2(K+3) + t_3^2]}{\tau^2 + t_3 \tau s - t_3^2}$$

Now we have constructed the 3-step increasing function $\varepsilon(t)$. Since we know the cumulative distribution function $\varepsilon'(t)$ of our signal intensity distribution is always increasing and must have at least 5 "points of intersection" with $\varepsilon(t)$, the graph of $\varepsilon'(t)$ must pass through the third "riser" of $\varepsilon(t)$ at t_3 (see Figure 9). Furthermore, since the height from this intersection point to the top step is the fractional signal energy beyond t_3, ε_3 is just an upper bound of this fractional energy. In a binary communication, we can always put t_3 at the boundary of a bit and then compute the fractional signal energy extended into the neighboring bits in the trailing edge. But, we have to remember, t_3 can be chosen only within some ranges. These ranges can be found from the conditions which require that t_1 and t_2 must be real and ε_1, ε_2, ε_3 must be real and positive.

4.3 Numerical Results

In this section, we use the model parameters given in Section 3.1 once again. We plot the curves of ε_3 as a function of the carrier frequency in Figure 10. Two values of t_3 are assigned, one at T_0, the other at $2T_0$. The shapes of those four curves are quite similar. In both models, ε_3 asymptotes to about 0.1 for $t_3=T_0$ and to about 0.005 for $t_3=2T_0$. Also we find when the carrier frequency is larger than 1 GHz in Model 1 and larger than 10 GHz in Model 2, ε_3 is approximately equal to the individual asymptotic value. These two values of the carrier frequency coincide roughly with those beyond which the propagation effects on the pulse

width can be neglected, as shown in Figure 3. Also from Figure 6, when the carrier frequencies are above those two values in two models, respectively, skewness values are less than 0.001, which is much smaller than that of the distribution in Figure 5. So we can conclude that the signal shape is nearly unchanged for the carrier frequency range above those two values in two models, respectively. Really, for the undistorted signal, the exact fractional energy beyond T_0 is 0.023 and that beyond $2T_0$ is 5×10^{-5}, which naturally are smaller than their upper bound 0.1 and 0.005 given above, respectively. Because we have the restrictions on the choice of t_3, we can not complete those curves in Figure 10 when the carrier frequency is below some value.

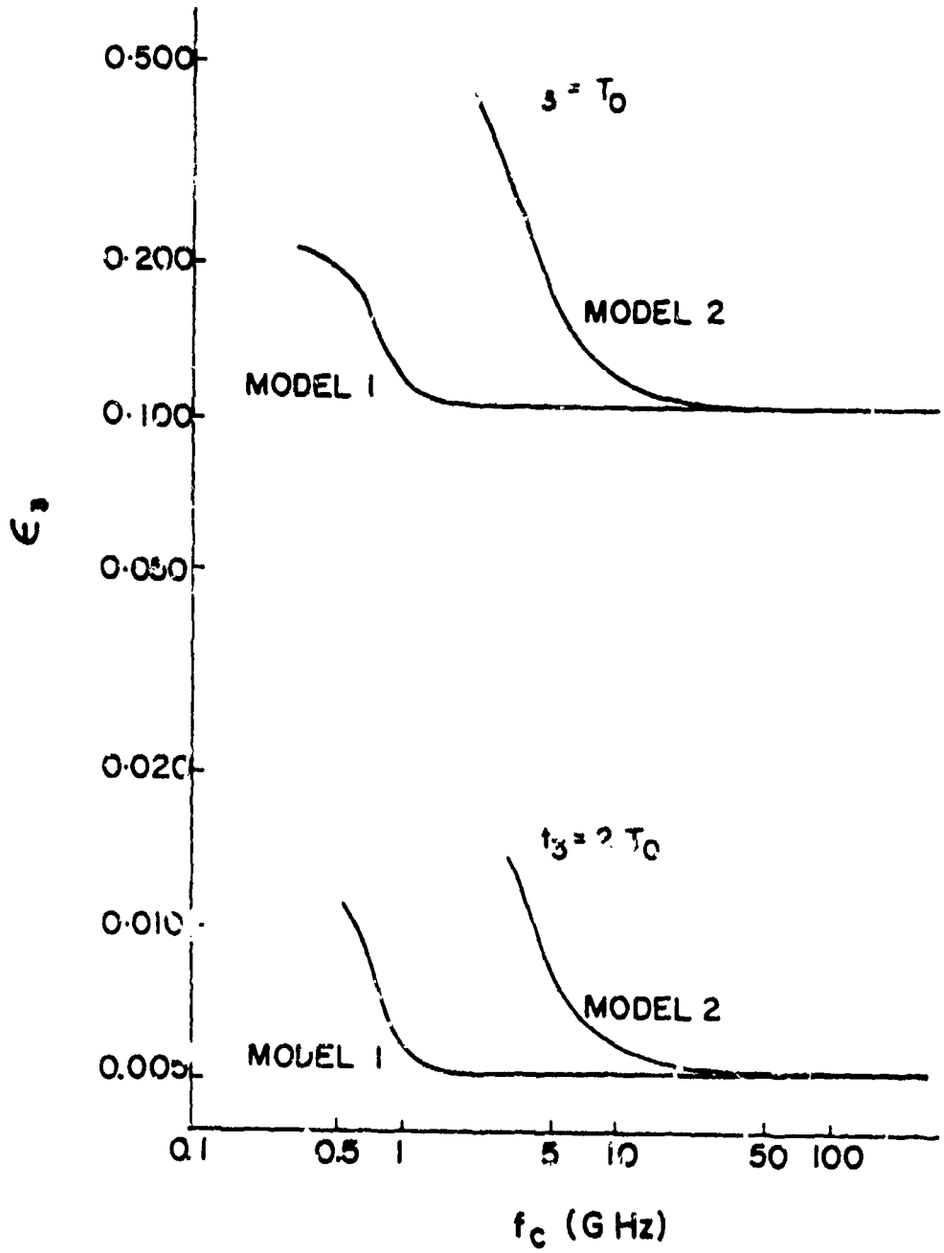

Figure 10. An upper bound of the fractional energy beyond t_3, ε_3 as a function of the carrier frequency. Two values of t_3 are assigned.

5. Summary and Conclusion

Starting from the Helmholtz wave equation (10), we derived an equation (17) for the two-frequency two-position mutual coherence function $\Gamma(\vec{\rho})$. In order to compute Γ_0, Γ_1, Γ_2, Γ_3, Γ_4, a set of equations for W_n and W_n' were derived. Γ_0, Γ_1, Γ_2, Γ_3, Γ_4 were evaluated and then temporal moments and temporal central moments up to the fourth order were computed. Two models for the geometry and ionospheric parameters were used to obtain numerical results.

We next consider a narrow-band Gaussian envelope carrier signal being impressed at z=0. After propagating through a turbulent plasma, owing to dispersion and random scattering, this originally symmetric signal is broadened and becomes asymmetric. The trailing edge is longer than the leading edge. From the information we obtained, we can not tell whether the received signal is just in a single clump. But if we can make sure of it by some other means, we compare the skewness and kurtosis values of the average signal intensity distribution with those of the distribution shown in Figure 5 and then get a rough idea about the shape of the received signal.

The results also showed the dominating propagation effect between dispersion and random scattering. As the arrival time and pulse width are concerned, the random scattering effect is more important, since the propagation effect will be much smaller if there are no random irregularities in the medium. As far as the signal asymmetry is concerned, the propagation effect mainly comes from dispersion in high frequency part and from random scattering in low frequency part in the carrier frequency range we considered. Finally, for the extent of signal concentration, random scattering effect is dominating.

Although we can not know the exact shape of the received signal intensity distribution, we can find an upper bound for the fractional signal energy beyond some time distance from the arrival time. In a binary communication, this information may help us to predict the errors in a decoding process. But to do it, we need more investigations.

References

Leader, J. C. (1978), Intensity fluctuations resulting from partially coherent light propagating through atmospheric turbulence, J. Opt. Soc. Am., 69, pp.73-84.

Liu, C. H., and K. C. Yeh (1977), Propagation of pulsed beam waves through turbulence, cloud, rain, or fog, J. Opt. Soc. Am., 67, No. 9, September.

Liu, C. H., and K. C. Yeh (1978), Pulse propagation in random media, IEEE Trans. on Antennas and Propagation, Vol. AP-26, No. 4, July.

Mark, W. D. (1972), Characterization of stochastic transients and transmission media: The method of power-moments spectra, Journal of Sound and Vibration, 22(3), pp.249-295.

Mises, R. v. (1964), Mathematical Theory of Probability and Statistics, Sec. 4 and 5, Chapter VIII, pp.384-396, Academic Press.

Shkarofsky, I. P. (1968), Generalized turbulence space-correlation and wave-number spectrum-function pairs, Can. J. Phys., Vol. 46, pp.2133-2153.

Sreenivasiah, I., A. Ishimaru, and S. T. Hong (1976), Two-frequency mutual coherence function and pulse propagation in a random medium: An analytic solution to the plane wave case, Radio Sci., 11, 775-778.

Tatarskii, V. I. (1971), The Effects of the Turbulent Atmosphere on Wave Propagation, U.S. Department of Commerce, National Technical Information Service, Springfield, Va.

Yeh, K. C., and C. H. Liu (1977a), An investigation of temporal moments of stochastic waves, Radio Sci., Vol. 12, No. 5, pp.671-680, Sept.-Oct.

Yeh, K. C., and C. H. Liu (1977b), Pulse delay and pulse distortion by random scattering in the ionosphere, AGARD-CP-244, Aspects of Electromagnetic Wave Scattering in Radio Communication, edited by A. N. Ince.

Yeh, K. C., and C. C. Yang (1977c), Mean arrival time and mean pulsewidth of signals propagation through a dispersive and random medium, IEEE Trans. on Antennas and Propagation, Vol. AP-25, No. 5, Sept.

Yeh, K. C., and C. H. Liu (1979), Ionospheric effects on radio communication and ranging pulses, IEEE Trans. on Antennas and Propagation, Vol. AP-27, No. 6, Nov.

Appendix B

A DETERMINISTIC STUDY OF PULSE PROPAGATION IN AN ELECTRON BUBBLE MEDIUM

BY

MICHAEL ROBERT TUCKER

B.S., University of Illinois, 1980

THESIS

Submitted in partial fulfillment of the requirements
for the degree of Master of Science in Electrical Engineering
in the Graduate College of the
University of Illinois at Urbana-Champaign, 1981

Urbana, Illinois

UNIVERSITY OF ILLINOIS AT URBANA-CHAMPAIGN

THE GRADUATE COLLEGE

July, 1981

WE HEREBY RECOMMEND THAT THE THESIS BY

MICHAEL ROBERT TUCKER

ENTITLED A DETERMINISTIC STUDY OF PULSE PROPAGATION IN AN ELECTRON BUBBLE MEDIUM

BE ACCEPTED IN PARTIAL FULFILLMENT OF THE REQUIREMENTS FOR THE DEGREE OF MASTER OF SCIENCE

W. C. Jen
Director of Thesis Research

Head of Department

Committee on Final Examination†

Chairman

† Required for doctor's degree but not for master's.

ACKNOWLEDGMENT

I would like to thank Dr. K. C. Yeh for his guidance throughout my year of research. I would also like to express my gratitude to Mrs. Linda Houston for typing this thesis.

This work was supported by the National Science Foundation through Grant No. ATM-80-07039 and by the Air Force Geophysics Laboratory through contract F19628-78-C-0195.

Appendix B

Table of Contents

1. Introduction

As a radio wave propagates through the ionosphere, random variations in the electron density will cause the wave to fluctuate. These fluctuations are called scintillations. Scintillations are especially apparent in regions called electron bubbles. Electron bubbles are regions in the ionosphere where electron density is very low. Also very sharp electron density gradients are present.

In this report I will make a deterministic study of pulse propagation through a model electron bubble at several different carrier frequencies. Because an electron bubble is a dispersive medium, one would expect a pulse propagating through a bubble to be distorted. I will obtain a graphical relationship between the carrier frequency and the pulse distortion. To obtain this relationship I will calculate the moments of the pulse envelope after the pulse has been transmitted through an electron bubble.

2. The Parabolic Equation

Microwave propagation through an electron bubble is a strong fluctuation problem because the log amplitude variance is greater than (.2-.5). The parabolic equation method [Tatarskii, 1971] will be used to study this problem.

Figure 1 shows the geometry of the problem. A wave propagates from $z=0$ to $z=Z_0$ through an electron bubble. In this report, the geometry is considered to be two dimensional so that there is no y dependence.

2.1 Derivation

The dielectric permittivity at any point $\underline{r}=(z,x)$ is written as an average or background value plus a fluctuating part.

$$\varepsilon_r(\underline{r}) = \langle\varepsilon_r(z)\rangle[1+\varepsilon_1(\underline{r})] \tag{1}$$

The average wave number is defined to be

$$k^2 = \omega^2\mu_0\varepsilon_0 \langle\varepsilon_r(z)\rangle \tag{2}$$

$$k^2 = k_0^2\langle\varepsilon_r(z)\rangle \tag{3}$$

The source free Maxwell's Equations are the starting point for the derivation of the parabolic equation.

$$\nabla\times\underline{E}(\underline{r}) = -i\omega\mu_0\underline{H}(\underline{r}) \tag{4}$$

$$\nabla\times\underline{H}(\underline{r}) = i\omega\varepsilon_r(\underline{r})\underline{E}(\underline{r}) \tag{5}$$

Taking the curl of (4) gives

$$\nabla\times\nabla\times\underline{E}(\underline{r}) = -i\omega\mu_0(\nabla\times\underline{H}(\underline{r})) \tag{6}$$

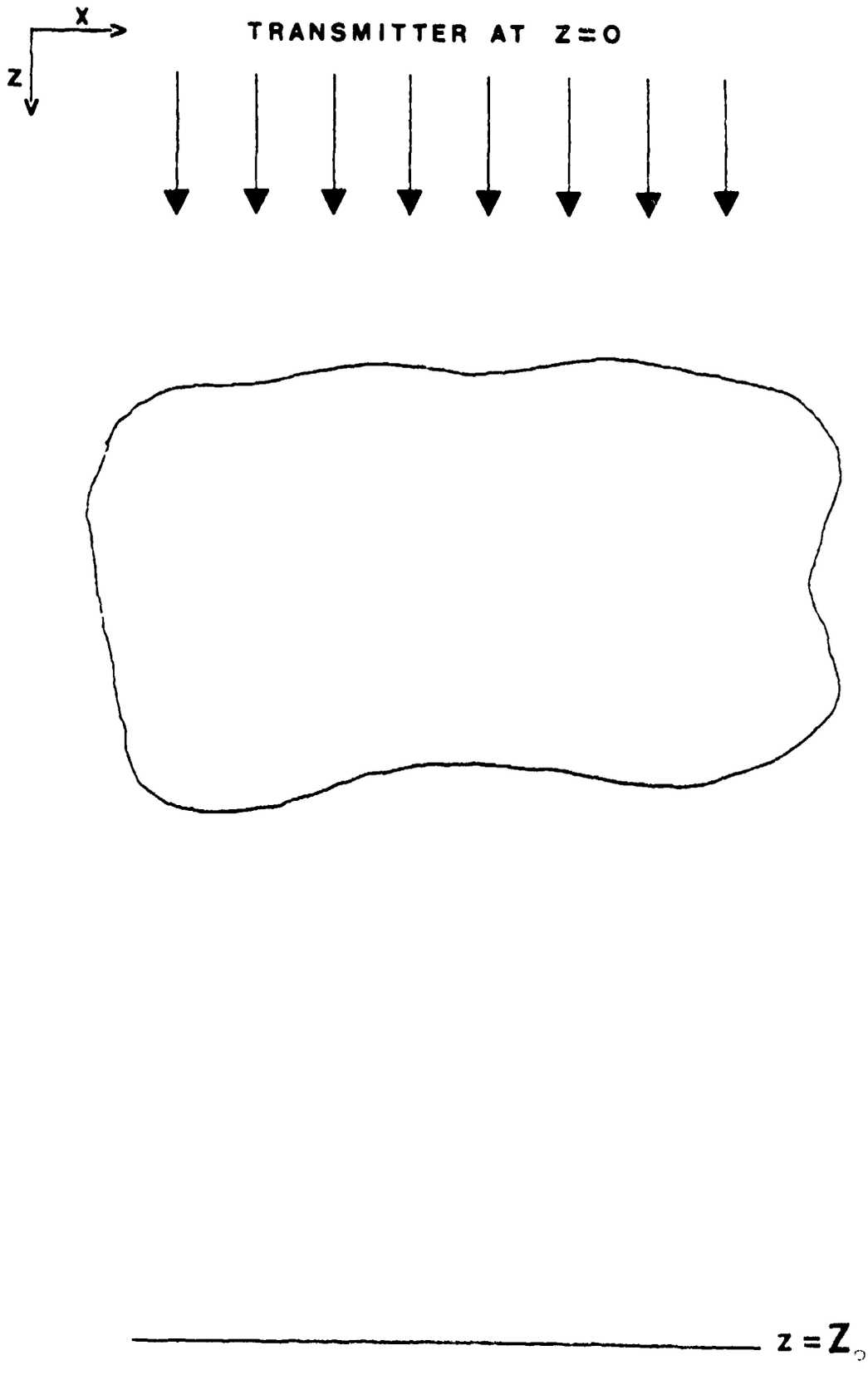

Figure 1- The geometry of the problem.

Substituting (5) into (6) results in

$$\nabla\times\nabla\times\underline{E}(\underline{r}) = -i\omega\mu_0(i\omega\varepsilon_r(\underline{r})\underline{E}(\underline{r})) \tag{7}$$

Using (3) and the vector identity $\nabla\times\nabla\times\underline{A}$=grad div $\underline{A}-\nabla^2\underline{A}$ gives

$$\text{grad div } \underline{E}(\underline{r})-\nabla^2\underline{E}(\underline{r}) = k_0^2\varepsilon_r(\underline{r})\underline{E}(\underline{r}) \tag{8}$$

If the irregularities are large compared to the signal wavelength then div $\underline{E}(\underline{r}) = 0$ [Tatarskii, 1971]. Equation (8) reduces to

$$\nabla^2\underline{E}(\underline{r})+k_0^2\varepsilon_r(\underline{r})\underline{E}(\underline{r}) = 0 \tag{9}$$

The x component of the electric field $\underline{E}(\underline{r})$ can be written as

$$E_x(r) = U(\underline{r})e^{ikz} \tag{10}$$

where $e^{-i\omega t}$ dependence is understood, propagation is along the z direction and $U(\underline{r})$ is complex. From (1)

$$k_0^2\varepsilon_r(\underline{r}) = k^2(1+\varepsilon_1(\underline{r})) \tag{11}$$

Substituting (10) and (11) into (9) gives

$$\nabla^2U(\underline{r})e^{ikz}+k^2(1+\varepsilon_1(\underline{r}))U(\underline{r})e^{ikz} = 0 \tag{12}$$

or

$$\frac{\partial^2}{\partial x^2}U(\underline{r})e^{ikz} + \frac{\partial^2}{\partial y^2}U(\underline{r})e^{ikz} + \frac{\partial^2}{\partial z^2}U(\underline{r})e^{ikz}$$

$$+k^2U(\underline{r})e^{ikz}+k^2\varepsilon_1(\underline{r})U(\underline{r}) = 0 \tag{13}$$

also

$$\frac{\partial^2}{\partial z^2}U(\underline{r})e^{ikz} = e^{ikz}\frac{\partial^2}{\partial z^2}U(\underline{r})+2ike^{ikz}\frac{\partial}{\partial z}U(\underline{r})-U(\underline{r})k^2e^{ikz} \tag{14}$$

Substituting (14) into (13) gives

$$\frac{\partial^2}{\partial x^2} U(\underline{r})e^{ikz} + \frac{\partial^2}{\partial y^2} U(\underline{r})e^{ikz} + e^{ikz} \frac{\partial^2}{\partial z^2} U(\underline{r})+2ike^{ikz}U(\underline{r})$$

$$-k^2U(\underline{r})e^{ikz}+k^2U(\underline{r})e^{ikz}+k^2\varepsilon_1(\underline{r})U(\underline{r})e^{ikz} = 0 \qquad (15)$$

Simplifying (15) results in

$$\nabla^2U(\underline{r})+2ik \frac{\partial}{\partial z} U(\underline{r})+k^2\varepsilon_1(\underline{r})U(\underline{r}) = 0 \qquad (16)$$

The scale size ℓ of the medium is defined to be the average distance over which the fluctuating part of the dielectric permittivity remains correlated. If $\ell >> \lambda$ then

$$\left|k \frac{\partial}{\partial z} U(\underline{r})\right| >> \left| \frac{\partial^2}{\partial z^2} U(\underline{r})\right| \qquad (17)$$

[Tatarskii, 1971]. So ∇^2 can be replaced by the transverse Laplacian

$$\nabla_T^2 = \frac{\partial^2}{\partial x^2} + \frac{\partial^2}{\partial y^2} \qquad (18)$$

and (16) becomes the parabolic equation.

$$\nabla_T^2U(\underline{r})+2ik \frac{\partial}{\partial z} U(\underline{r})+k^2\varepsilon_1(\underline{r})U(\underline{r}) = 0 \qquad (19)$$

The strong fluctuation problem is reduced to solving the parabolic equation for a medium with $\varepsilon_1(\underline{r})$ variations. These variations can be treated stochastically where $\varepsilon_1(\underline{r})$ is a random process. However in an electron bubble medium, very sharp electron density gradients occur. As will be seen in the next section, these will lead to large fluctuations in $\varepsilon_1(\underline{r})$. In this case $\varepsilon_1(\underline{r})$ will be treated deterministically.

2.2 Determination of $\varepsilon_1(r)$

Recalling Equation (1)

$$\varepsilon_r(\underline{r}) = \langle\varepsilon_r(z)\rangle[1+\varepsilon_1(\underline{r})]$$

where:

$\varepsilon_r(\underline{r})$ is the relative dielectric permittivity at any point $\underline{r}$

$\langle\varepsilon_r(z)\rangle$ is the background relative dielectric permittivity for a height z (the value at the edge of the bubble).

$\varepsilon_1(\underline{r})$ is the varying part of the relative permittivity.

The background relative dielectric permittivity is given in terms of the background plasma frequency.

$$\langle\varepsilon_r(z)\rangle = 1 - \frac{\omega_{p_0}^2(z)}{\omega^2} \tag{20}$$

$$\omega_{p_0}^2(z) = \frac{N_0(z)e^2}{m\varepsilon_0} \tag{21}$$

$N_0(z)$ is the background electron density for a height z.

e is the electron charge.

m is the electron mass.

ε_0 is the free space dielectric permittivity.

The relative dielectric permittivity at any point $\underline{r}$ is given by

$$\varepsilon_r(\underline{r}) = 1 - \frac{\omega_p^2(\underline{r})}{\omega^2} \tag{22}$$

$$\omega_p^2(\underline{r}) = \frac{N(\underline{r})e^2}{m\varepsilon_0} \tag{23}$$

where $N(\underline{r})$ is the electron density at any point $\underline{r}$

$$N(\underline{r}) = N_0(z) - \Delta N(\underline{r}) \tag{24}$$

$$N(\underline{r}) = N_0(z)\ [1 - \frac{\Delta N(\underline{r})}{N_0(z)}] \tag{25}$$

Rewriting $\omega_p^2(\underline{r})$ in terms of $\omega_{p_0}^2(z)$

$$\omega_p^2(\underline{r}) = \frac{N_0(z)}{m\varepsilon_0}\, e^2[1 - \frac{\Delta N(\underline{r})}{N_0(z)}] \tag{26}$$

or

$$\omega_p^2(\underline{r}) = \omega_{p_0}^2(z)[1 - \frac{\Delta N(\underline{r})}{N_0(z)}] \tag{27}$$

Substituting (22) and (20) into (1) gives

$$1 - \frac{\omega_p^2(r)}{\omega^2} = [1 - \frac{\omega_{p_0}^2(z)}{\omega^2}][1 + \varepsilon_1(\underline{r})] \tag{28}$$

Substituting (27) and (21) into (28) and solving for $\varepsilon_1(\underline{r})$ results in

$$\varepsilon_1(\underline{r}) = \frac{\omega_{p_0}^2(z)}{\omega^2}\ [\frac{\Delta N(\underline{r})}{N_0(z)}]\ /\ (1 - \frac{\omega_{p_0}^2(z)}{\omega^2}) \tag{29}$$

So the fluctuating part of the relative dielectric permittivity is dependent on the frequency of the wave, the background plasma frequency and the fluctuations in the electron density. In an electron bubble, the electron density fluctuations will be spiky, thus $\varepsilon_1(\underline{r})$ cannot be treated as a statistically homogeneous random process. So the statistics of $\varepsilon_1(\underline{r})$ cannot be uniquely determined by its mean and autocorrelation (or by its power spectrum). Thus a deterministic model is used to study wave propagation in a medium of this type.

3. The Electron Bubble

3.1 The Bubble Model

In several observation programs near the magnetic equator, scintillation at Gigahertz frequencies has been related to the development of electron bubbles. Soon after sunset, thin layers of irregularities develop below the F layer and quickly start to rise. The irregularity layer thickens and develops into a region of depleted electron density. These regions are called electron bubbles.

In-situ rocket and satellite measurements are used to provide further information about electron bubbles. Specifically, in-situ data measured by McClure et al. (1977) was used to develop the model of the bubble used in this report. The data is shown in Figure 2. Figure 2 shows electron density measurements along a satellite path and clearly indicates irregularities and sharp electron gradients. I will use the model developed by Wernik, (1979). Wernik in modeling the bubble assumed a two dimensional model. Also he assumed the horizontal variations of the electron density in the bubble to be that given in Figure 2 at every height z. The background density (the density of the background ionosphere) is assumed to follow a parabolic profile.

$$N_0(z) = N_M\,[1-(z-Z_M)^2/H_0^2]G \qquad (30)$$

where N_M is the maximum electron concentration at height Z_M, and H_0 is the scale height. During the course of bubble development, its leading edge becomes sharper while its trailing (lower) edge becomes more blunt. Wernik defined two stages of development, the initial stage and the developed stage. G is a weighting function which takes

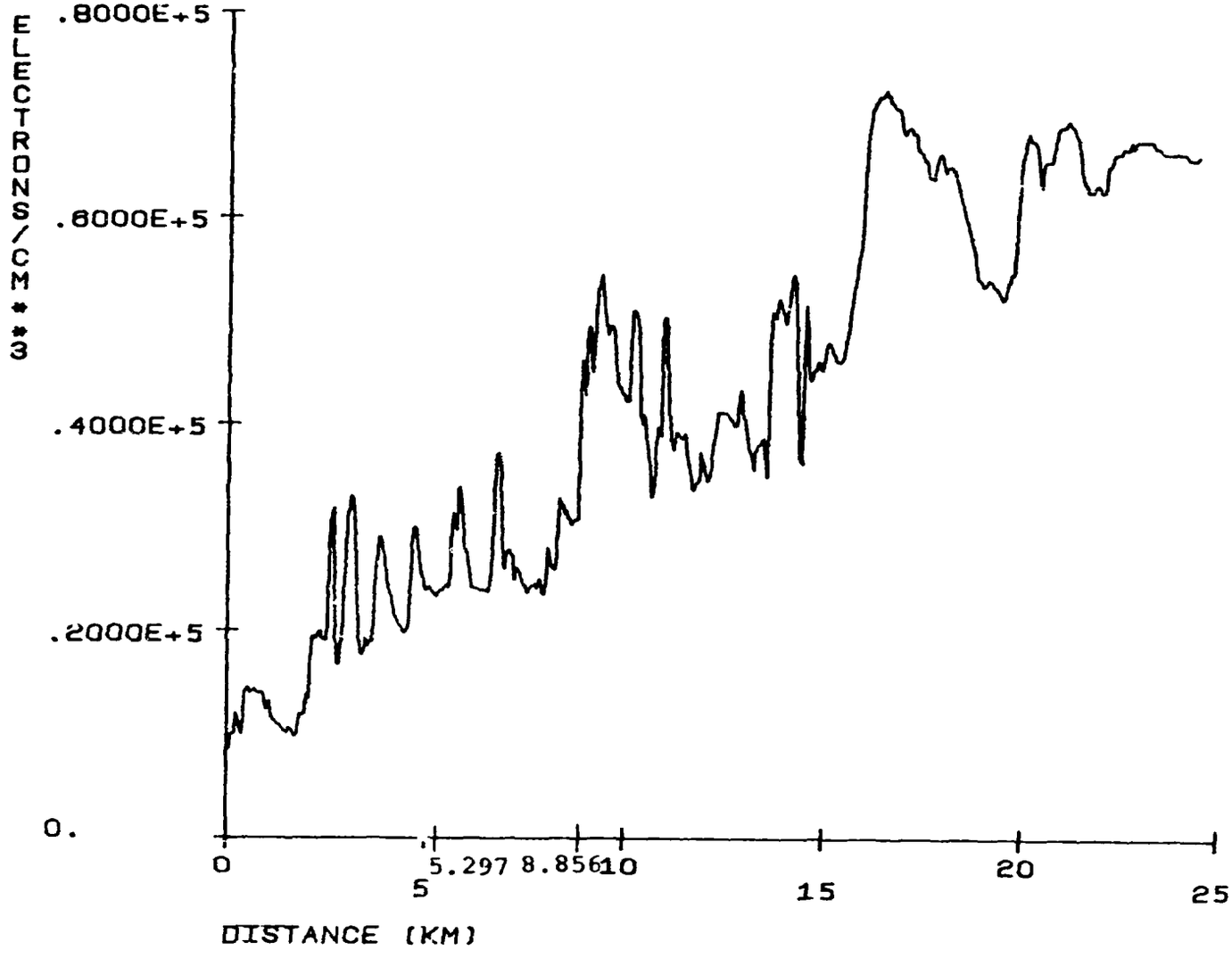

Figure 2- Horizontal electron density fluctuations used in the bubble model.

the different stages into account. In this thesis I will use the developed stage. The weighting function G is shown in Figure 3 for the developed stage.

To calculate the electron density at a point $\underline{r}=(z,x)$ inside the bubble, the following equation is used

$$N(\underline{r}) = N_0(z) - \left[\frac{\Delta N(\underline{r})}{N_0(z)} \right] N_0(z) \tag{31}$$

where $N_0(z)$ is given by (30) and $\Delta N(\underline{r})/N_0(z)$ is obtained from Figure 2.

In order to obtain the solution to the parabolic equation, the fluctuating part of the relative dielectric permittivity must be solved according to Equation (29). When f, the frequency of the wave is much larger than the plasma frequency f_p, which is always the case in this thesis, then (29) can be simplified to

$$\varepsilon_1(\underline{r}) = \frac{80.6(10^{-6})\Delta N(\underline{r})}{f^2} \tag{32}$$

where $\Delta N(\underline{r})=N_0(z)-N(\underline{r})$ and is in electrons/cm^3 and f is in MHz.

3.2 Program SHEET 1

Wernik (1979) developed a program called SHEET to model wave propagation through an electron bubble. I have rewritten and revised his program to make it run more efficiently. My program is called SHEET 1. SHEET 1 solves the wave propagation problem in the electron bubble model described in the previous section by obtaining solutions for the parabolic equation. The following analytic solution to the parabolic equation was used by Wernik in his SHEET program and is used in my SHEET 1 program.

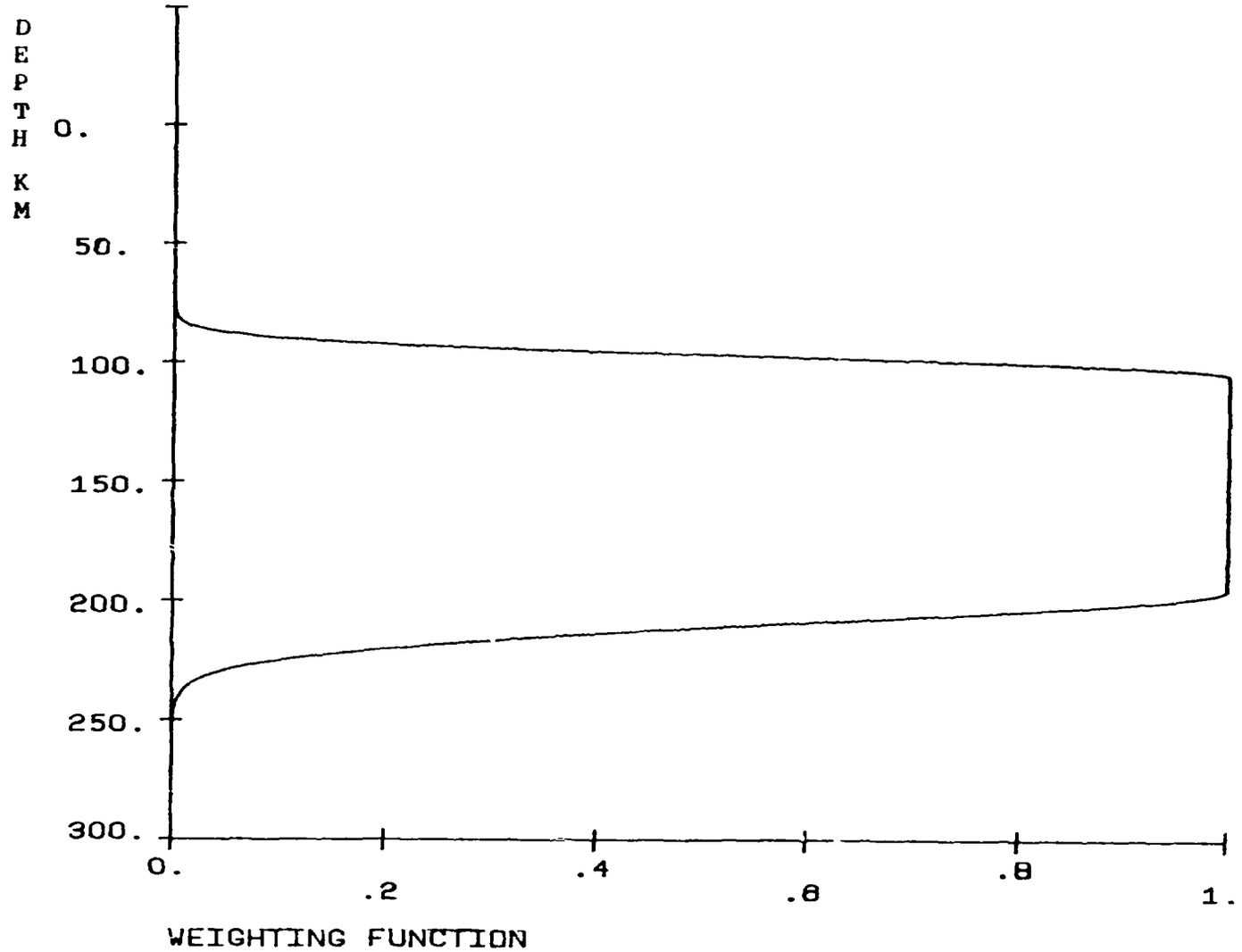

Figure 3- The weighting function used in the bubble model.

The parabolic equation (19) was obtained in section 2.1.

$$\nabla_T^2 U(\underline{r}) - 2ik \frac{\partial}{\partial z} U(\underline{r}) + k^2 \varepsilon_1(\underline{r}) U(\underline{r}) = 0$$

Since the bubble model used in this report is 2 dimensional, $\underline{r}=(z,x)$ so

$$\nabla_T^2 = \partial^2/\partial x^2 \tag{33}$$

thus (19) reduces to

$$-2ik \frac{\partial}{\partial z} U(\underline{r}) + \frac{\partial^2}{\partial x^2} U(\underline{r}) + k^2 \varepsilon_1(\underline{r}) U(\underline{r}) = 0 \tag{34}$$

The following substitutions are made

$$t = kz \qquad b = kx \tag{35}$$

Substituting (35) into (34) gives

$$\frac{\partial}{\partial t} U(t,b) + \frac{i}{2} \frac{\partial^2 U(t,b)}{\partial b^2} + \frac{i}{2} \varepsilon_1(t,b) U(t,b) = 0 \tag{36}$$

The entire medium is partitioned into a grid as shown in Figure 4. The step sizes in (z,x) space are P and M. These must be changed into step sizes in (t,b) space by

$$\begin{aligned} \tau &= P \cdot k \\ H &= M \cdot k \end{aligned} \tag{37}$$

To solve (36) numerically, the implicit Crank-Nicholson difference scheme is used. This scheme uses the following analog to the second derivative

$$\frac{\partial^2}{\partial b^2} U(t,b) = \frac{1}{H^2} [\sigma(U_{j+1}^{n+1} - 2U_j^{n+1} + U_{j-1}^{n+1}) + (1-\sigma)(U_{j+1}^n - 2U_j^n + U_{j-1}^n)] \tag{38}$$

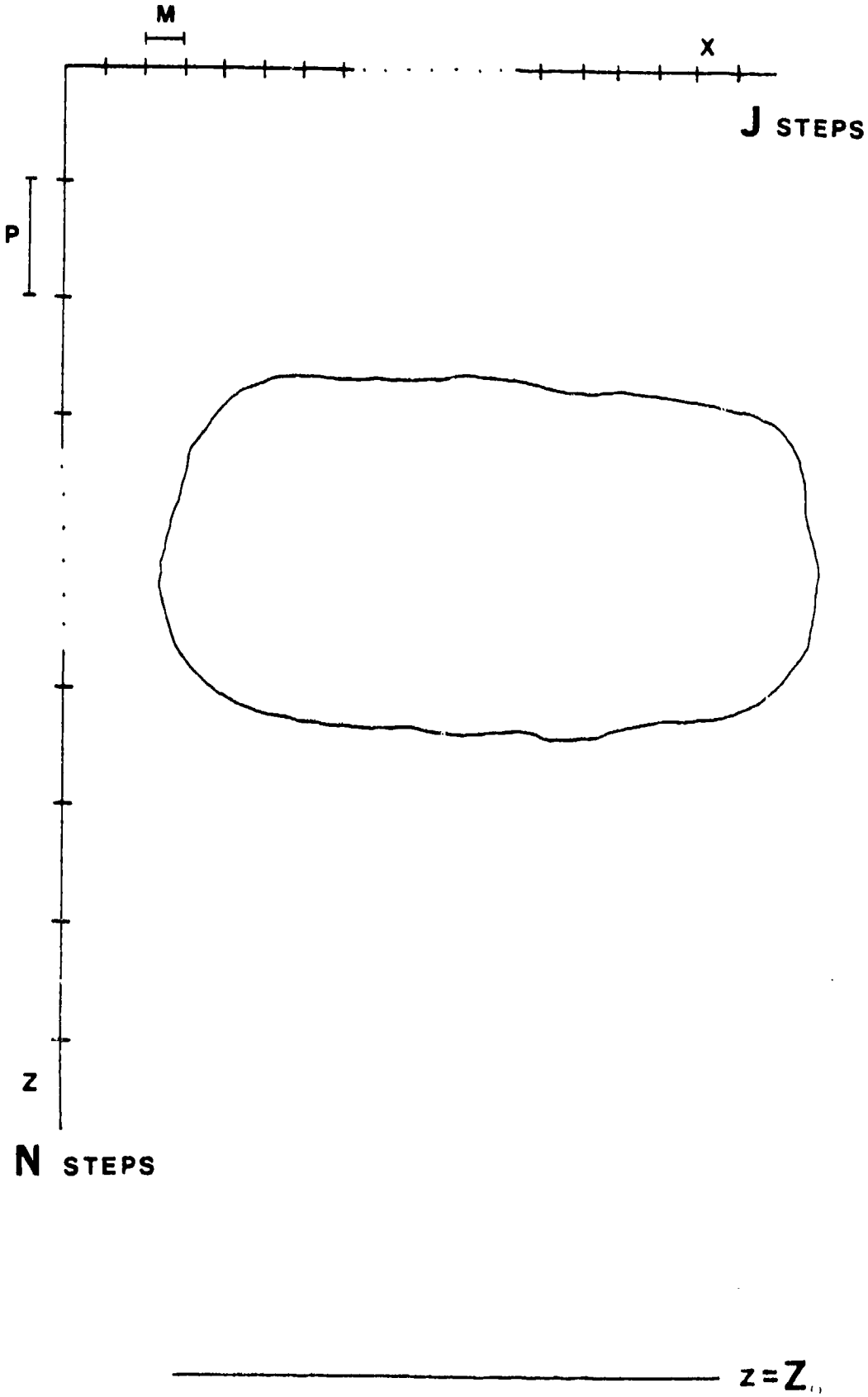

Figure 4- The medium partitioned into a grid.

and the following analog to the first derivative

$$\frac{\partial}{\partial t} U(t,b) = (U_j^{n+1} - U_j^n)/\tau \tag{39}$$

where

$$j = 0,1,2,\ldots, J$$

$$n = 0,1,2,\ldots, N$$

$$\sigma = 1/2$$

J is the number of steps in the b direction (also in the x direction) and N is the number of steps in the t direction (also in the z direction). The term $\varepsilon_1(t,b)U(t,b)$ is expressed as

$$\frac{\varepsilon_{1_j}^{n+1} + \varepsilon_{1_j}^{n}}{2} [\sigma U_j^{n+1} + (1-\sigma)U_j^n] \tag{40}$$

The f function is defined to be

$$f_j^n = (\varepsilon_{1_j}^{n+1} + \varepsilon_{1_j}^{n})/2 \tag{41}$$

Substituting (41), (40), (39) and (38) into (36) gives

$$\frac{i\tau}{2H^2}\sigma U_{j+1}^{n+1} + (1 - \frac{i\tau}{H}\sigma + \frac{i\tau\sigma}{2} f_j^n)U_j^{n+1} + \frac{i\tau}{2H^2}\sigma U_{j-1}^{n+1} = \frac{-i\tau}{H^2}(1-\sigma)U_{j+1}^n + [1 + \frac{i\tau(1-\sigma)}{H^2}$$

$$- \frac{i\tau}{2}(1-\sigma)f_j^n]U_j^n - \frac{i\tau}{2H^2}(1-\sigma)\, U_{j-1}^n \tag{42}$$

A problem occurs at the boundaries of the bubble where the equation depend on U_0^n and U_{J+1}^n. "False" boundries are set up with $U_0^n=0$ and $U_{J+1}^n=0$. The effect of these boundaries does not penetrate deeply into the field.

Equation (42) can be expressed as a matrix multiplication

$$B^n U^{n+1} = (B^n - \tau \cdot A^n) U^n \qquad n=0,1,\ldots,N \tag{43}$$

so for each step in the z direction there is a matrix A^n and a matrix B^n.

$$\left| B^n \right| \left| \begin{matrix} U_0^{n+1} \\ \vdots \\ U_J^{n+1} \end{matrix} \right| = \left| B^n - \tau \cdot A^n \right| \left| \begin{matrix} U_0^n \\ \vdots \\ U_J^n \end{matrix} \right| \tag{44}$$

The matrices A^n and B^n are tridiagonal. Only the main diagonal and the diagonal on each side of the main diagonal have non-zero elements. The reason for this is because (42) depends only on U_{j+1}^{n+1}, U_j^{n+1}, U_{j-1}^{n+1}, U_j^n, U_{j+1}^n and U_{j-1}^n. The elements of the matrices are found from (42)

$$B_{j,j}^n = 1 - \frac{i\tau\sigma}{H^2} + i\tau f_j^n \tag{45}$$

$$B_{j+1,j}^n = B_{j,j+1}^n = \frac{i\tau\sigma}{2H^2} \tag{46}$$

$$A_{j,j}^n = \frac{-i}{H^2} + \frac{i}{2} f_j^n \tag{47}$$

$$A_{j+1,j}^n = A_{j,j+1}^n = \frac{i}{H^2} \tag{48}$$

for $j=0,1,2,\ldots\ldots,J$

Starting from (43) U^{n+1} is solved

$$B^n U^{n+1} = (B^n - \tau \cdot A^n) U^n$$

$$U^{n+1} = [1-(B^n)^{-1} \tau A^n] U^n \tag{49}$$

$$U^{n+1} = U^n - \tau X^n \tag{50}$$

where

$$X^n = (B^n)^{-1} A^n U^n \tag{51}$$

or

$$B^n X^n = A^n U^n \tag{52}$$

Equation (52) is solved in SHEET 1 for X^n using Gaussian elimination via the Thomas algorithm [Ames (1969)]. Since B^n is tridiagonal, Equation (52) can be written as

$$\begin{aligned} aa_j x_{j-1} + cc_j x_j + bb_j x_{j+1} &= d_j \\ cc_1 x_1 + bb_1 x_2 &= d_1 \\ aa_J x_{J-1} + cc_J x_J &= d_J \end{aligned} \tag{53}$$

where:

aa_j, cc_j and bb_j are elements of matrix B^n, and

$$\begin{aligned} x_0 &= x_{J+1} = 0 \\ d_j &= a_j U_{j-1}^n + c_j U_j^n + b_j U_{j+1}^n \\ d_1 &= c_1 U_1^n + b_1 U_2^n \\ d_J &= a_J U_{J-1}^n + C_J U_J^n \end{aligned} \tag{54}$$

where:

a_j, c_j and b_j are elements of matrix A^n, and $U_0^n = U_{J+1}^n = 0$.

The Thomas Algorithm is used to solve (52). A solution is assumed

$$x_j = a_{j+1} x_{j+1} + \beta_{j+1} \tag{55}$$

where:

$$\alpha_{j+1} = -bb_j/(aa_j\alpha_j+cc_j) \tag{56}$$

$$\beta_{j+1} = (d_j-aa_j\beta_j)/(aa_j\alpha_j+cc_j) \tag{57}$$

$$\alpha_2 = -bb_1/cc_1 \qquad \beta_2 = d_2/cc_1 \tag{58}$$

since

$$x_{J+1} = 0 \tag{59}$$

$$x_J = \beta_{J+1} \tag{60}$$

$$x_J = (d_J-aa_J\beta_J)//aa_J\alpha_J+cc_J) \tag{61}$$

After the X^n matrix is solved, (50) is used to obtain the solution of the parabolic equation at the next t (or z) step.

4. Moments

4.1 Definition

In this thesis, pulses of three different carrier frequencies and two different pulse widths are propagated through an electron bubble medium. In order to analyze the output pulse, the method of temporal moments will be used. Specifically, the first four temporal moments will be used to give a description of the output pulse envelope.

The pulse incident on the electron bubble can be described as

$$p_i(\underline{r},t) = \int_{-\infty}^{\infty} F(\omega)e^{-i(\omega t-\underline{k}\cdot\underline{r})}d\omega \tag{62}$$

Where $F(\omega)$ is the frequency spectrum of the pulse. Assuming propagation parallel to the z axis, the pulse at a receiver at (z_0,x_0) is

$$p_0(z_0,x_0,t) = \int_{-\infty}^{\infty} F(\omega)U(z_0,x_0,\omega)e^{-i(\omega t-kz)}d\omega \tag{63}$$

where $U(z_0,x_0,\omega)$ is the parabolic equation solution. The output pulse can alternately be described as

$$p_0(z_0,x_0,t) = A(z,x,t)e^{i\omega_c(t-z/c)} \tag{64}$$

$A(z,x,t)$ is the envelope of the pulse and ω_c is the carrier frequency. The nth temporal moment is defined as

$$M_n(z) = \int_{-\infty}^{\infty} A^*(z,x,t)t^nA(z,x,t)dt \tag{65}$$

where:

$n=0,1,2,.....$

4.2 Physical Significance

When n=0 Equation (65) becomes

$$M_0(z) = \int_{-\infty}^{\infty} |A(z,x,t)|^2 dt \tag{66}$$

Equation (66) is just the expression for the total energy in the pulse. When n=1, Equation (65) becomes

$$M_1(z) = \int_{-\infty}^{\infty} A^*(z,x,t)tA(z,x,t)dt \tag{67}$$

Equation (67) is the expression for the mean of the square of the envelope. If $M_1(z)$ is normalized by dividing by $M_0(z)$, then an expression for the mean arrival time (denoted by t_a) is obtained.

$$t_a = M_1(z)/M_0(z) \tag{68}$$

The mean arrival time can be used to calculate the delay caused by the electron bubble medium.

When moments of higher order are needed, t_a is used to define the central moment. The nth central moment is defined as

$$\bar{M}_n(z) = \int_{-\infty}^{\infty} A^*(z,x,t)(t-t_a)^n A(z,x,t)dt \tag{69}$$

The 2nd central moment is analogous to the variance in probability theory. When n=2, Equation (69) (after normalization) becomes

$$\frac{\bar{M}_2(z)}{M_0(z)} = \tau^2 = \frac{M_2(z)}{M_0(z)} - t_a^2 \tag{70}$$

τ^2 is called the mean square pulse width. τ gives a measure of the pulse spreading caused by frequency dispersion in the medium.

The third central moment is written as

$$\bar{M}_3(z) = \int_{-\infty}^{\infty} A^*(z,x,t)(t-t_a)^3 A(z,x,t)dt \tag{71}$$

The skewness s is defined by

$$\frac{\bar{M}_3(z)}{M_0(z)} = s\tau^3 \tag{72}$$

or

$$s\tau^3 = M_3(z)/M_0(z) - 3M_2(z)t_a/(M_0(z))^2 + 2t_a^3 \tag{73}$$

The value of s is a measure of the pulse asymmetry. If a pulse is perfectly symmetric about the mean arrival time, the skewness will be zero. In this thesis, if s is negative, more of the energy in the pulse is concentrated in the trailing edge of the pulse rather in its leading edge.

5. Data

In this section, I will calculate the moments of the pulse envelope after the pulse has been propagated through the electron bubble medium. Pulses of three different carrier frequencies and two different pulse widths will be analyzed. The three carrier frequencies are 2.5 GHz, 800 MHz and 500 MHz. The two pulse widths are 6.51 nanoseconds and 12.95 nanoseconds. For each of these carrier frequencies and pulse widths, a receiver will be placed at two positions. The first is x=5.297 km. Note from Figure 2 that at x=5.297 km the bubble has relatively constant electron density. The second x position is x=8.856 km. At this x position, the bubble has a very sharp electron density fluctuation.

SHEET 1 is run nine times for each carrier frequency at each x position to obtain the parabolic equation solution across the entire pulse bandwidth. Linear interpolations are done to obtain the amplitude and phase of the parabolic equation solutions between the SHEET 1 outputs. For the 500 MHz carrier frequency, additional SHEET 1 runs were made because the amplitude started to fluctuate greatly at the lower end of the pulse bandwidth. Figures 5-16 show the interpolated parabolic equation solutions for each carrier frequency and each x position. These Figures are essentially the transfer function which describes the electron bubble medium. This transfer function is dependent on frequency and on x.

Some of the input and output pulses are shown in Figures 17-23. These Figures show the input pulse, the input pulse spectrum, the input pulse envelope, the output pulse at x=5.297 km, the output pulse envelope at x=5.297 km, the output pulse at x=8.856 km and the output

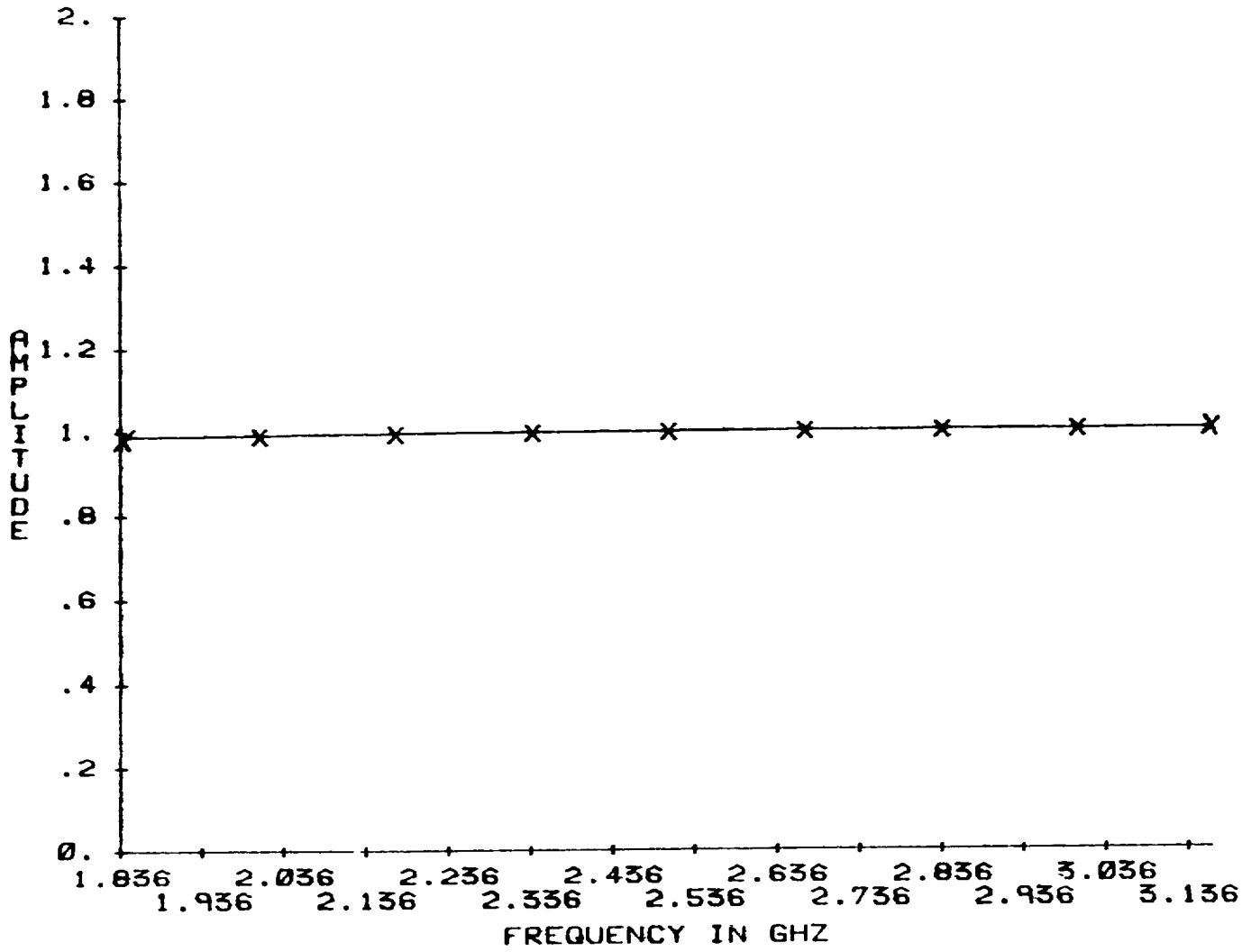

Figure 5- The amplitude of the transfer function for 2.5 GHZ at x=5.297 km.

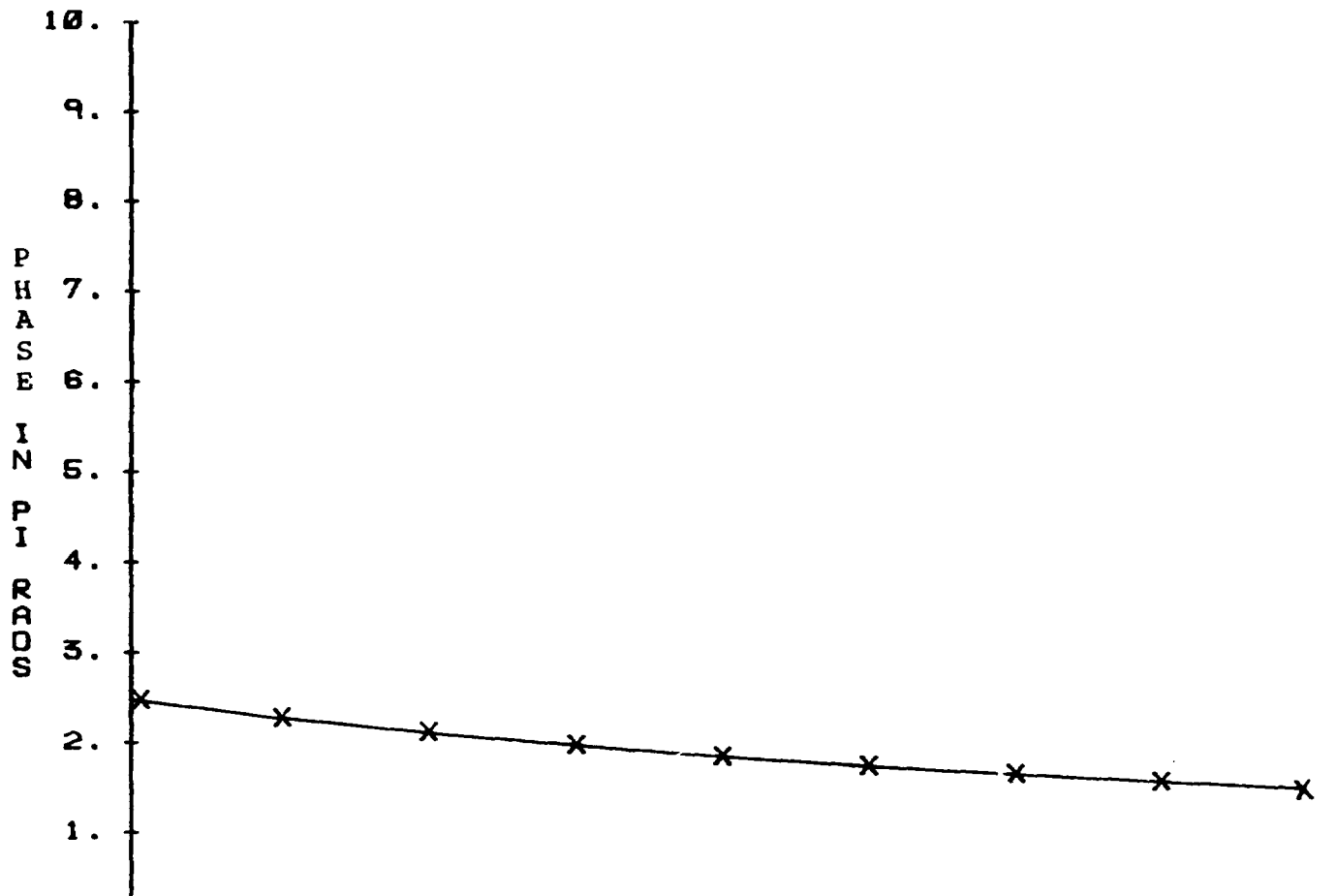

Figure 6- The phase of the transfer function for 2.5 GHZ at x=5.297 km.

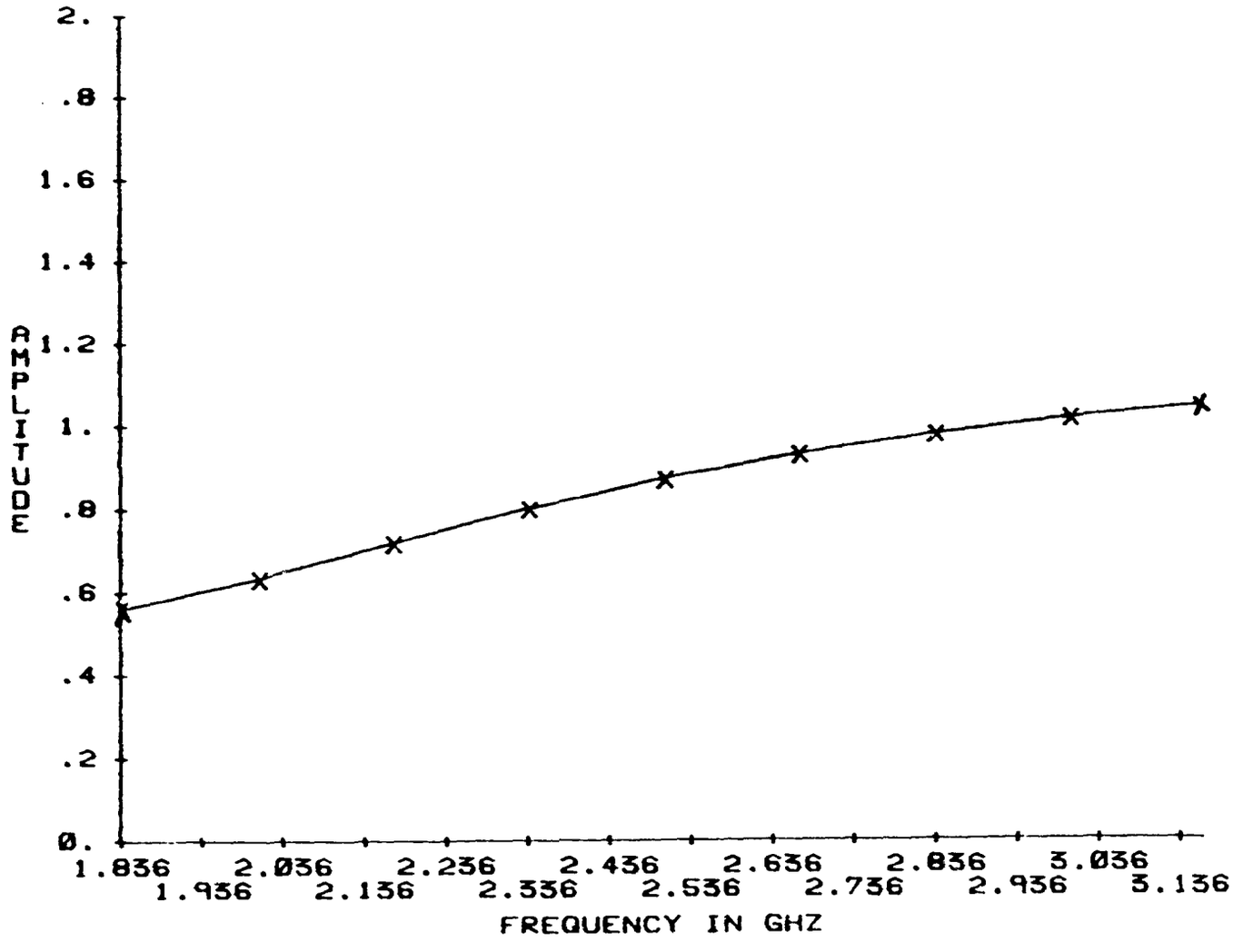

Figure 7- The amplitude of the transfer function for 2.5 GHZ at x=8.856 km.

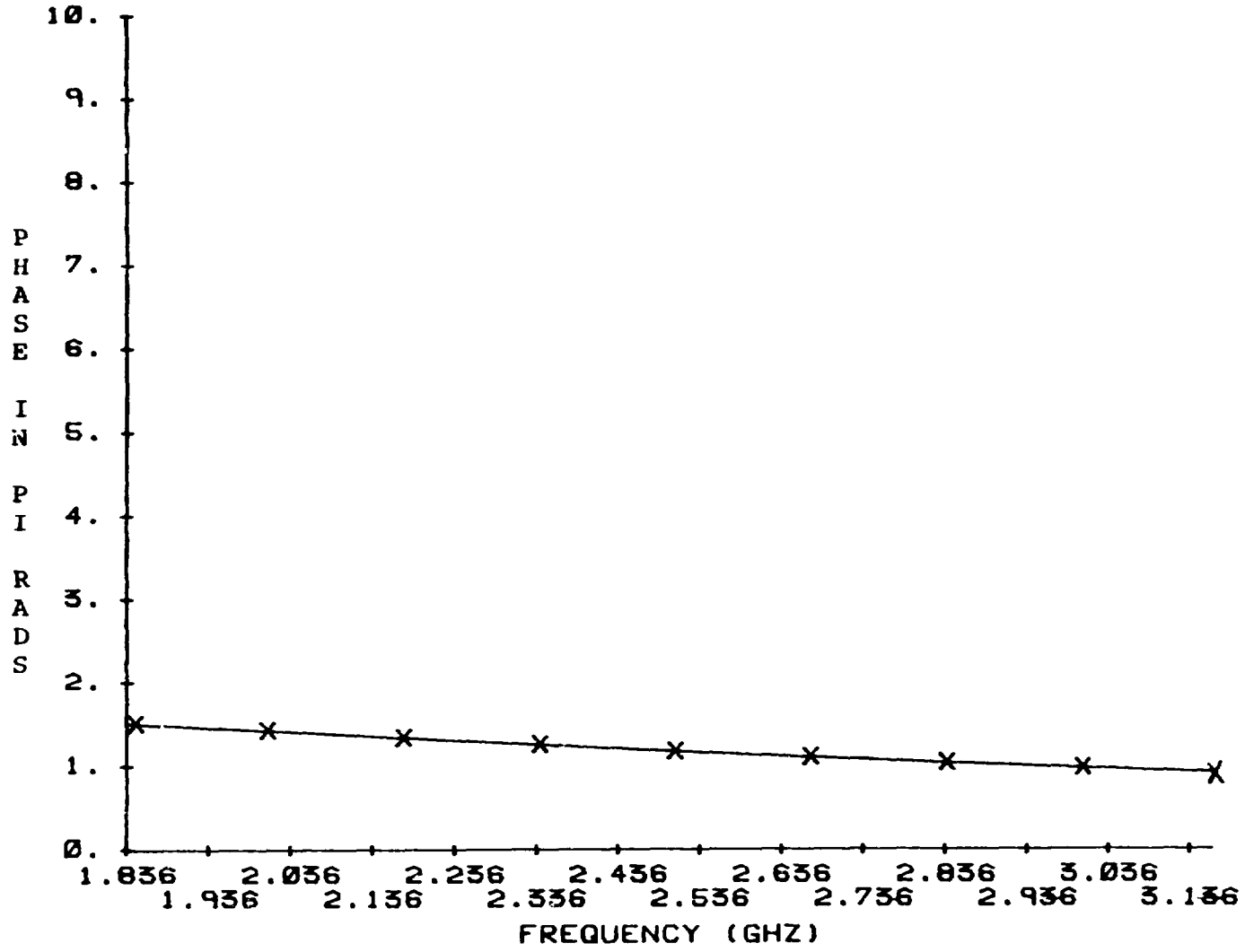

Figure 8- The phase of the transfer function for 2.5 GHZ at x=8.856 km.

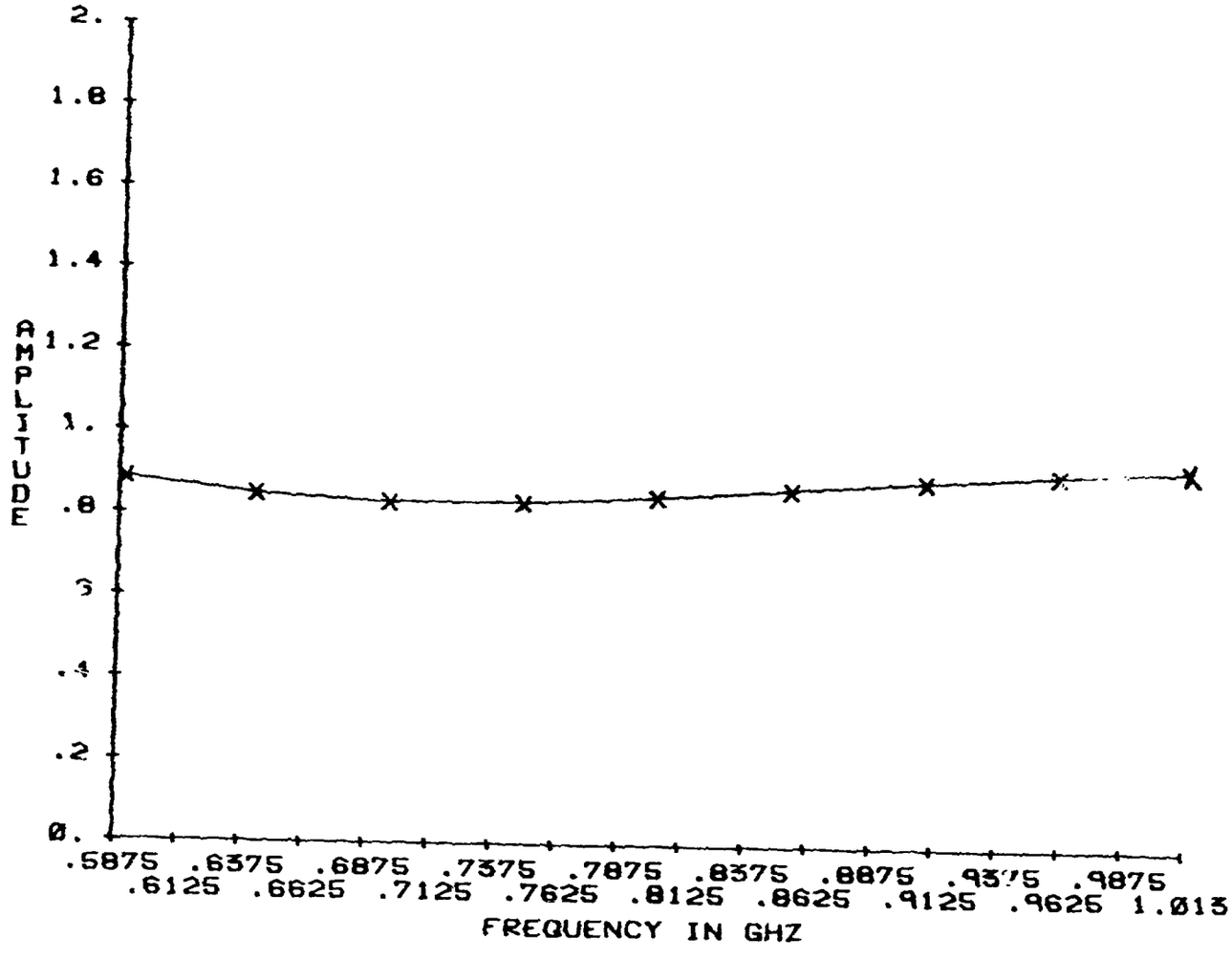

Figure 9- The amplitude of the transfer function for 800 MHZ at x=5.297 km.

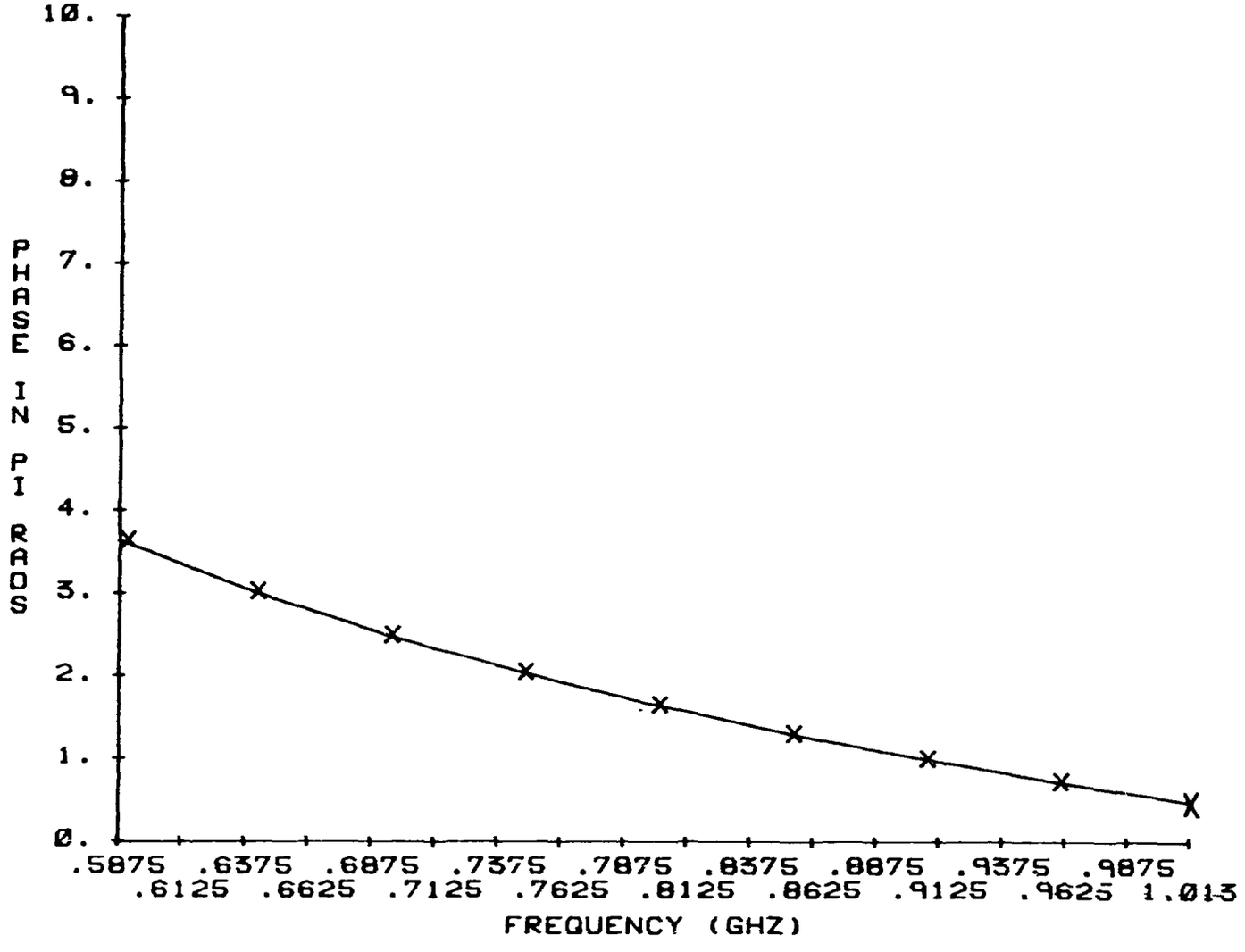

Figure 10- The phase of the transfer function for 800 MHZ at x-5.297 km.

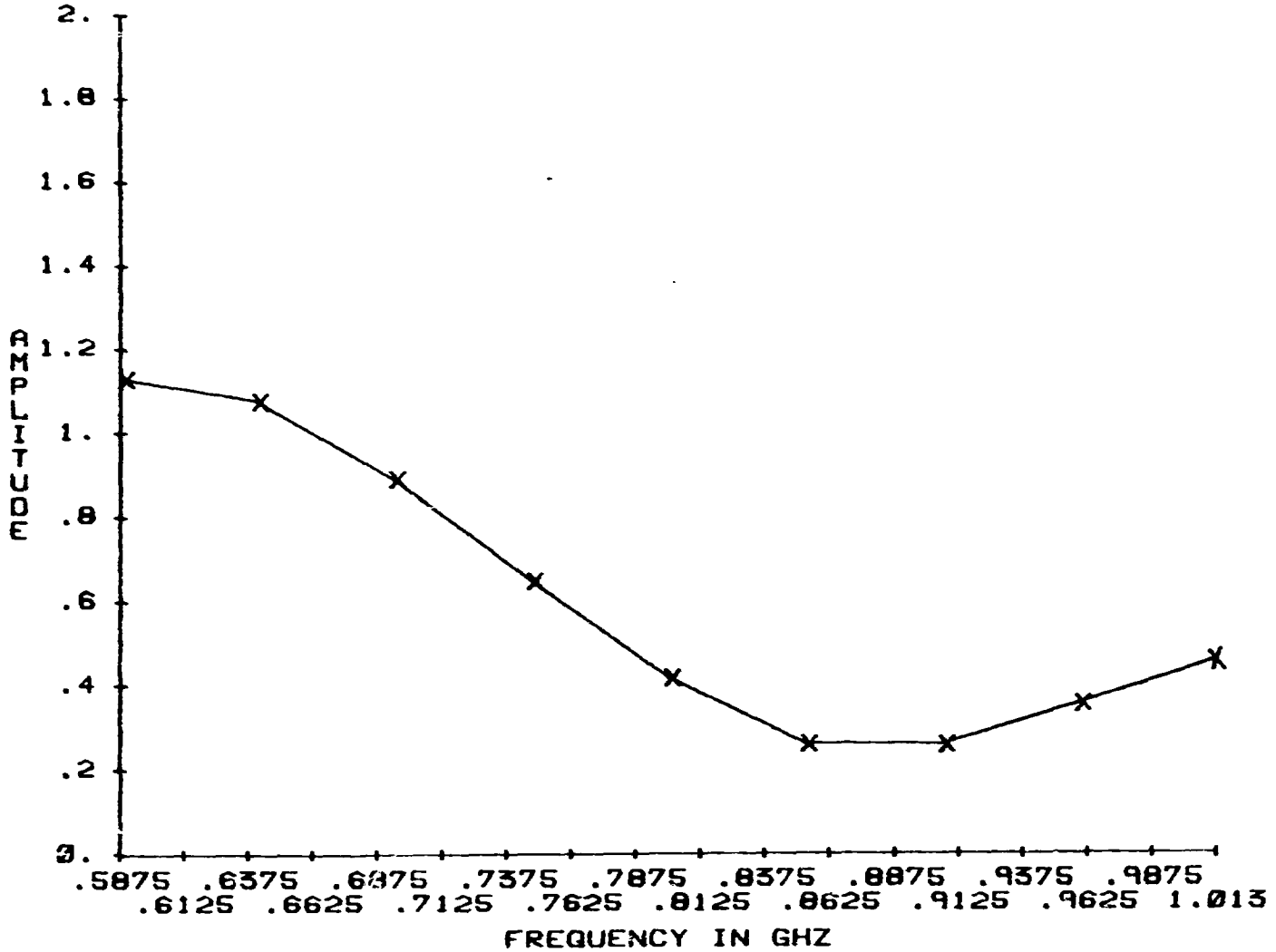

Figure 11- The amplitude of the transfer function for 800 MHZ at x=8.856 km.

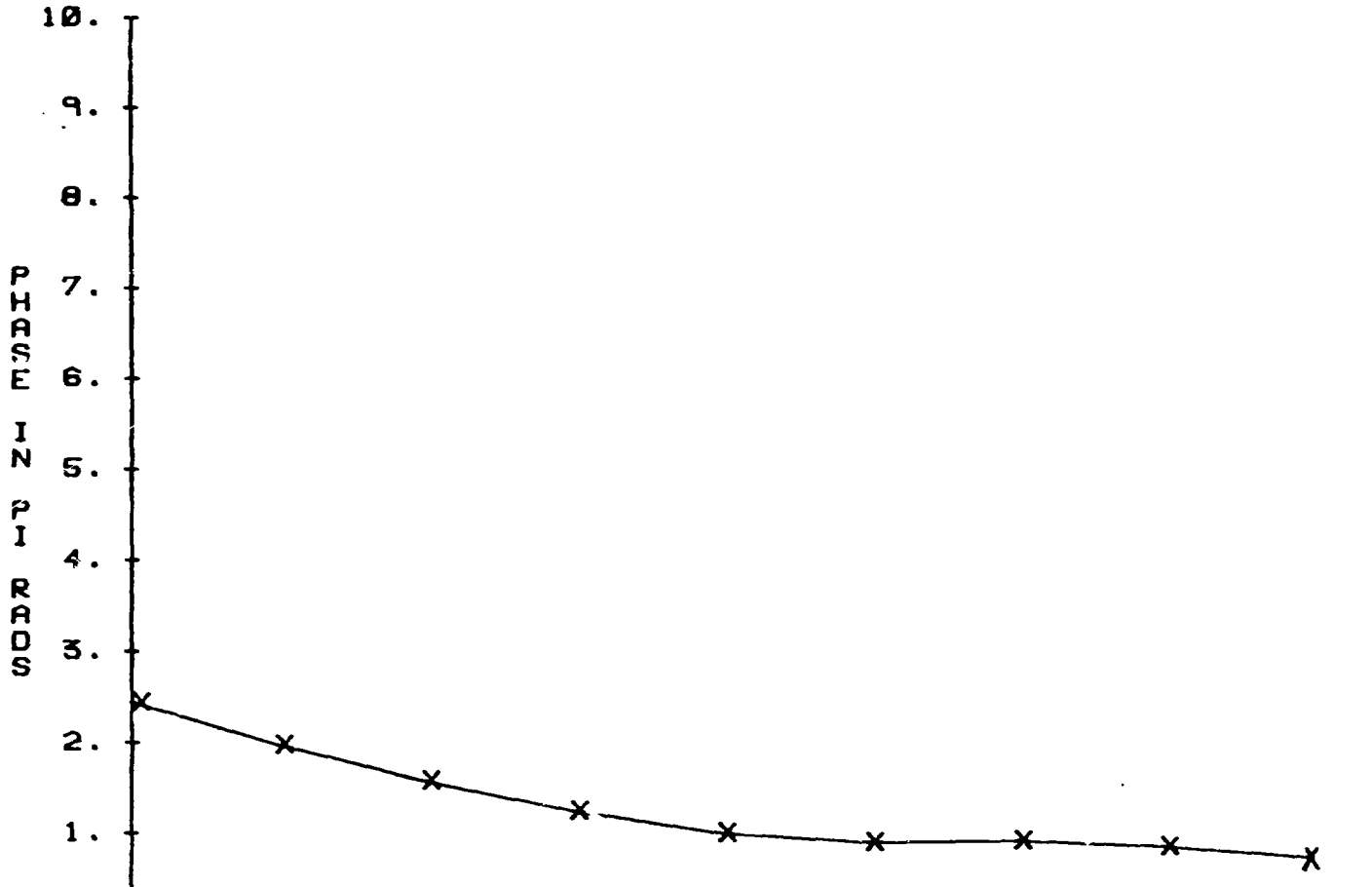

Figure 12- The phase of the transfer function for 800 MHZ at x=8.856 km.

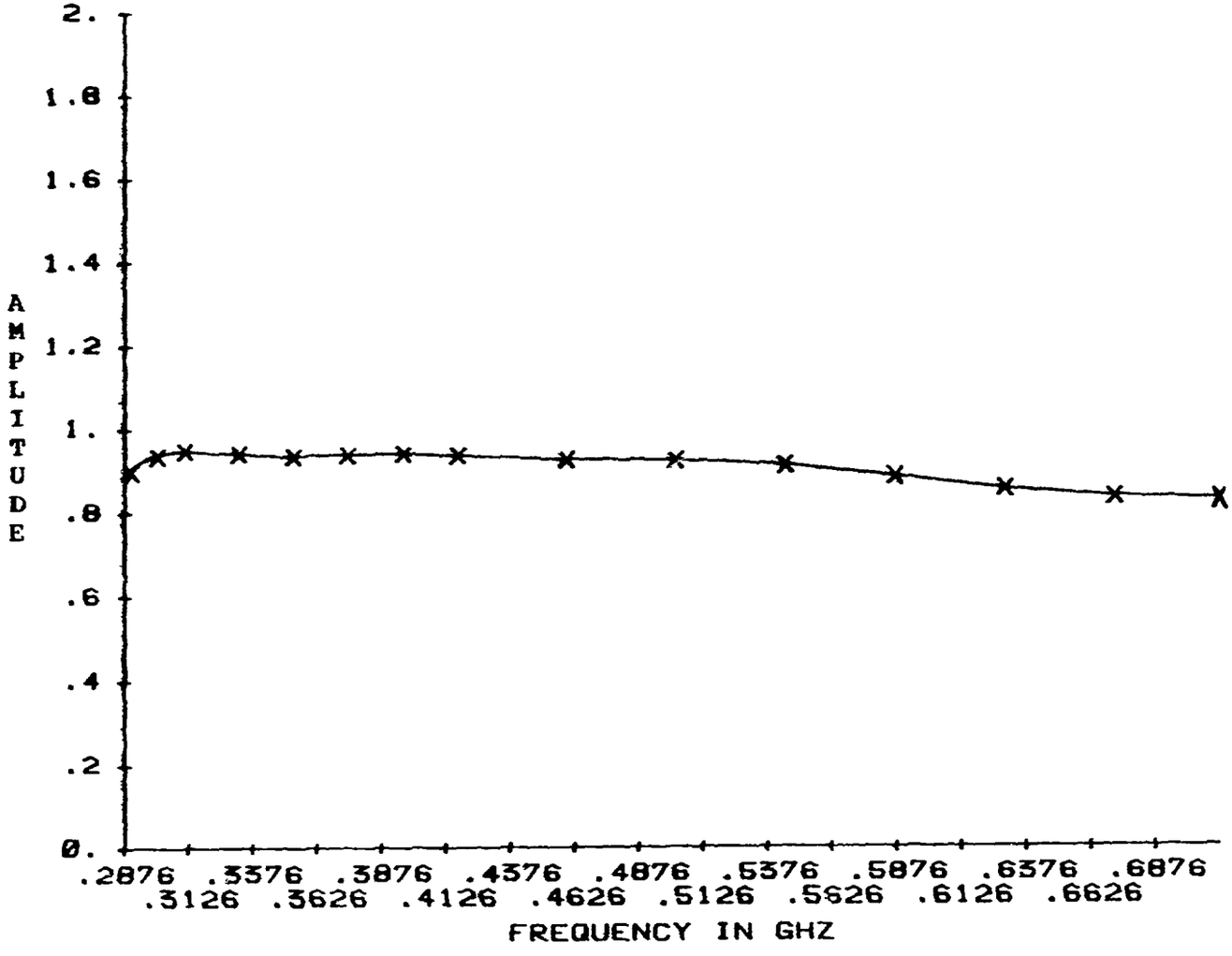

Figure 13- The amplitude of the transfer function for 500 MHZ at x=5.297 km.

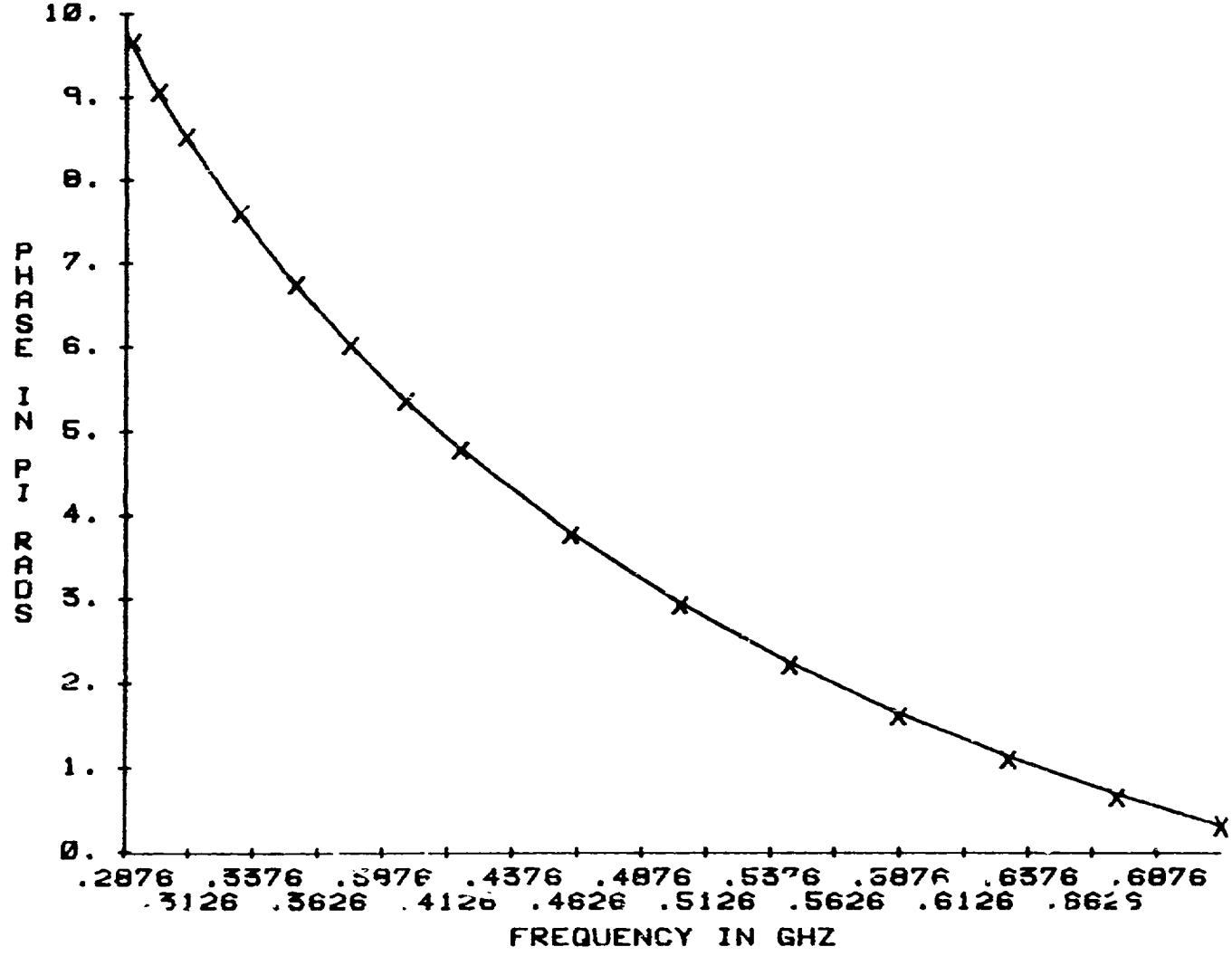

Figure 14- The phase of the transfer function for 500 MHZ at x=5.297 km.

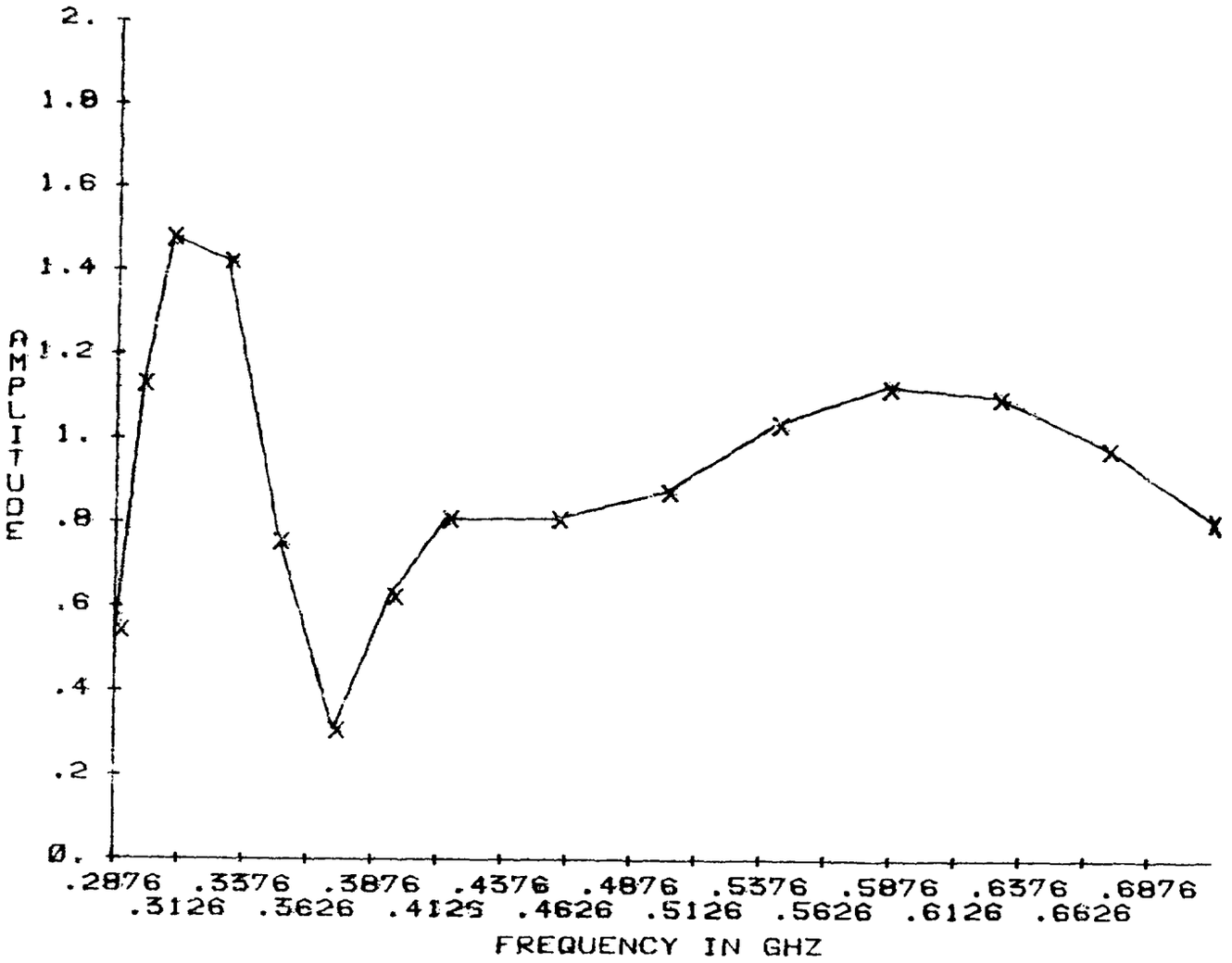

Figure 15- The amplitude of the transfer function for 500 MHZ at x=8.856 km.

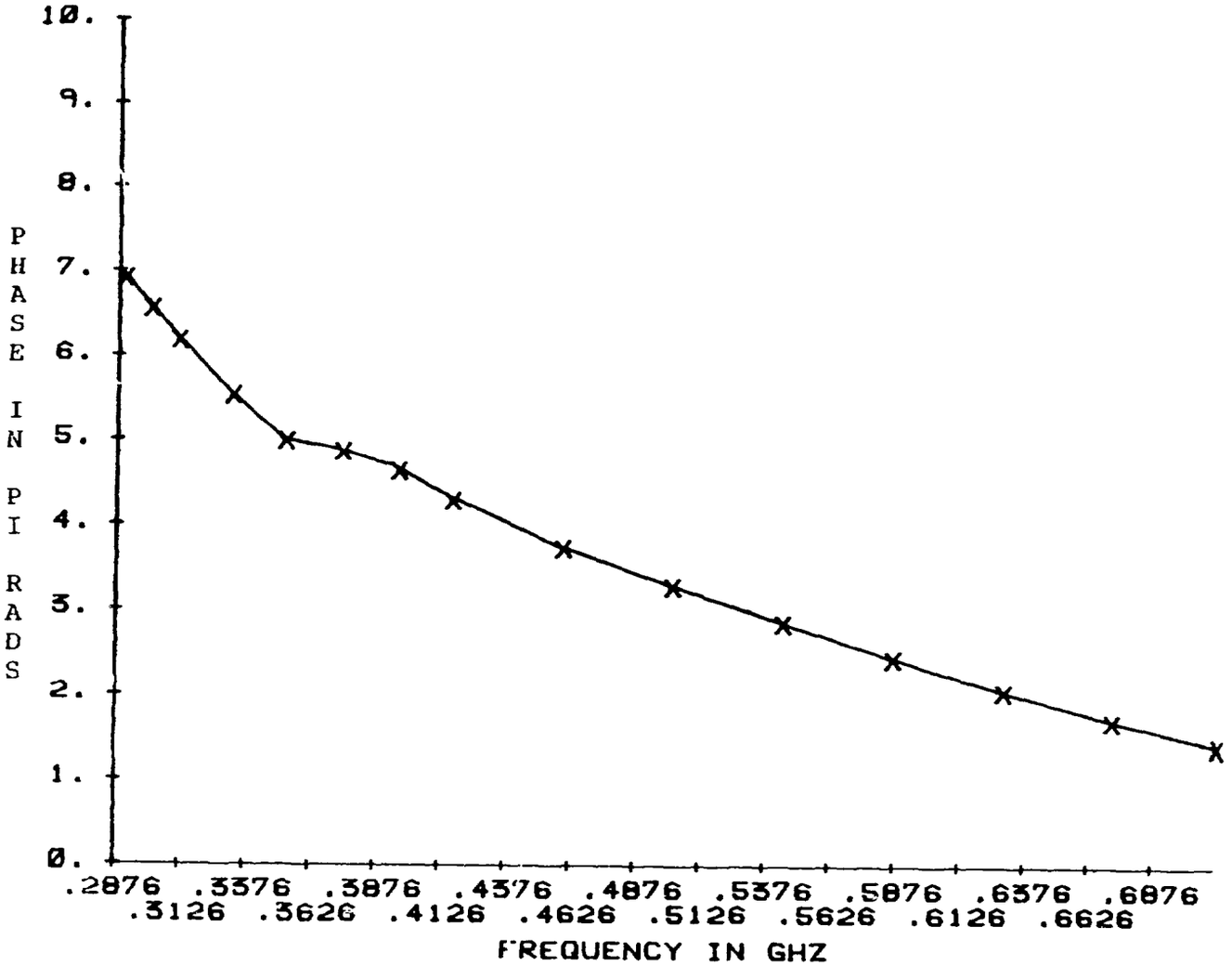

Figure 16- The phase of the transfer function for 500 MHZ at x=8.856 km.

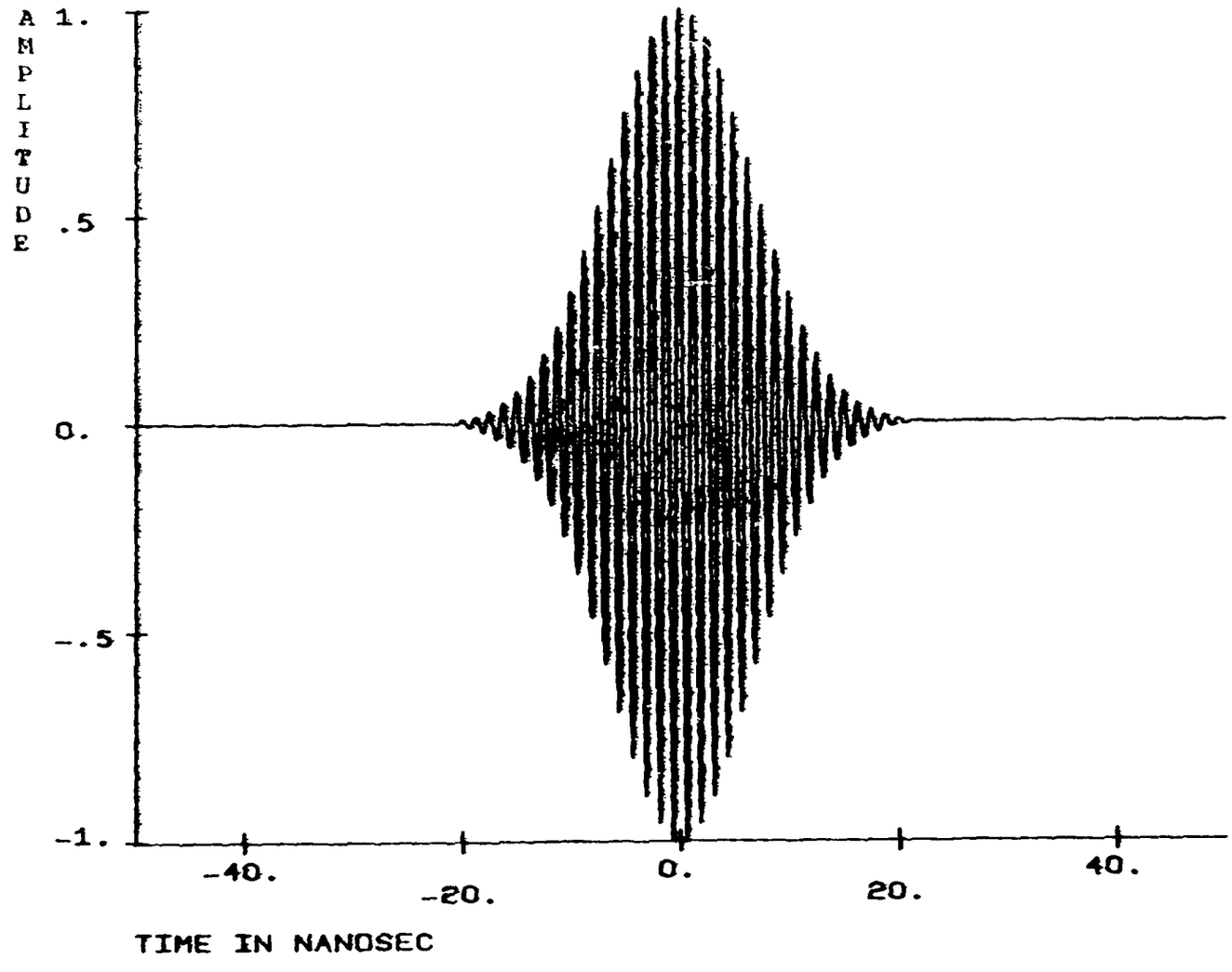

Figure 17- The input pulse applied to the medium with a carrier frequency of 800 MHZ and a pulse width of 6.51 nsec.

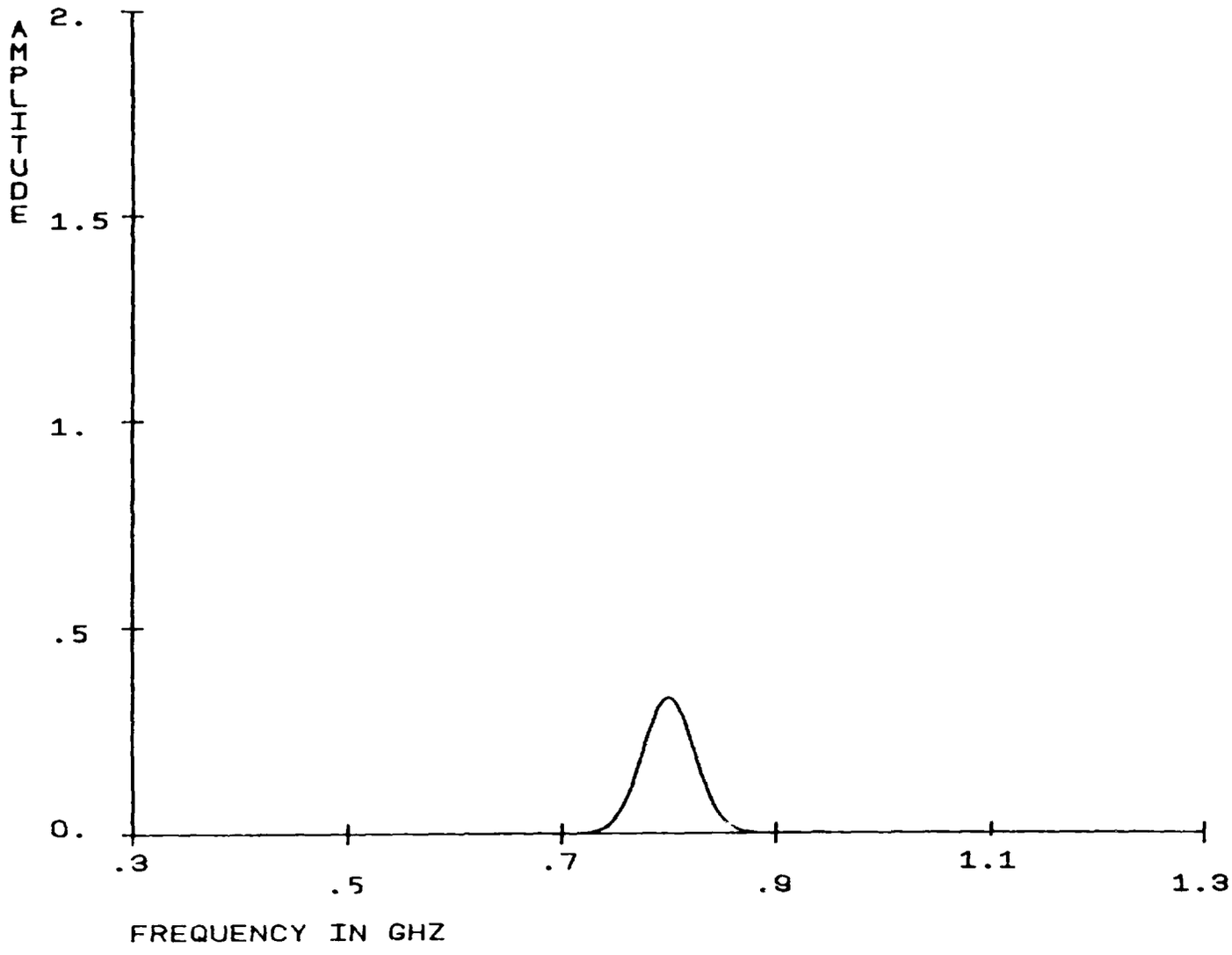

Figure 18- The frequency spectrum of the input pulse.

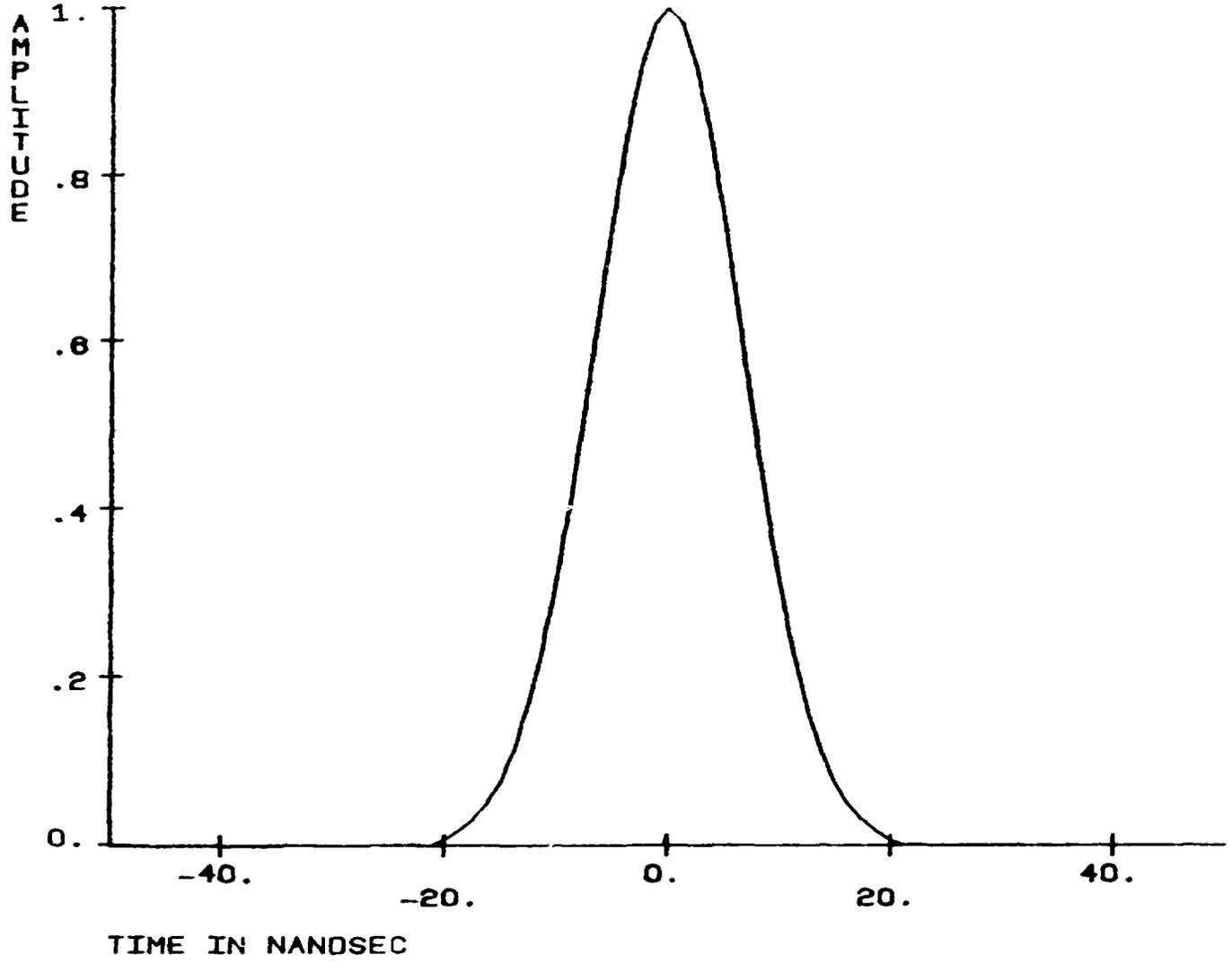

Figure 19- The envelope of the input pulse.

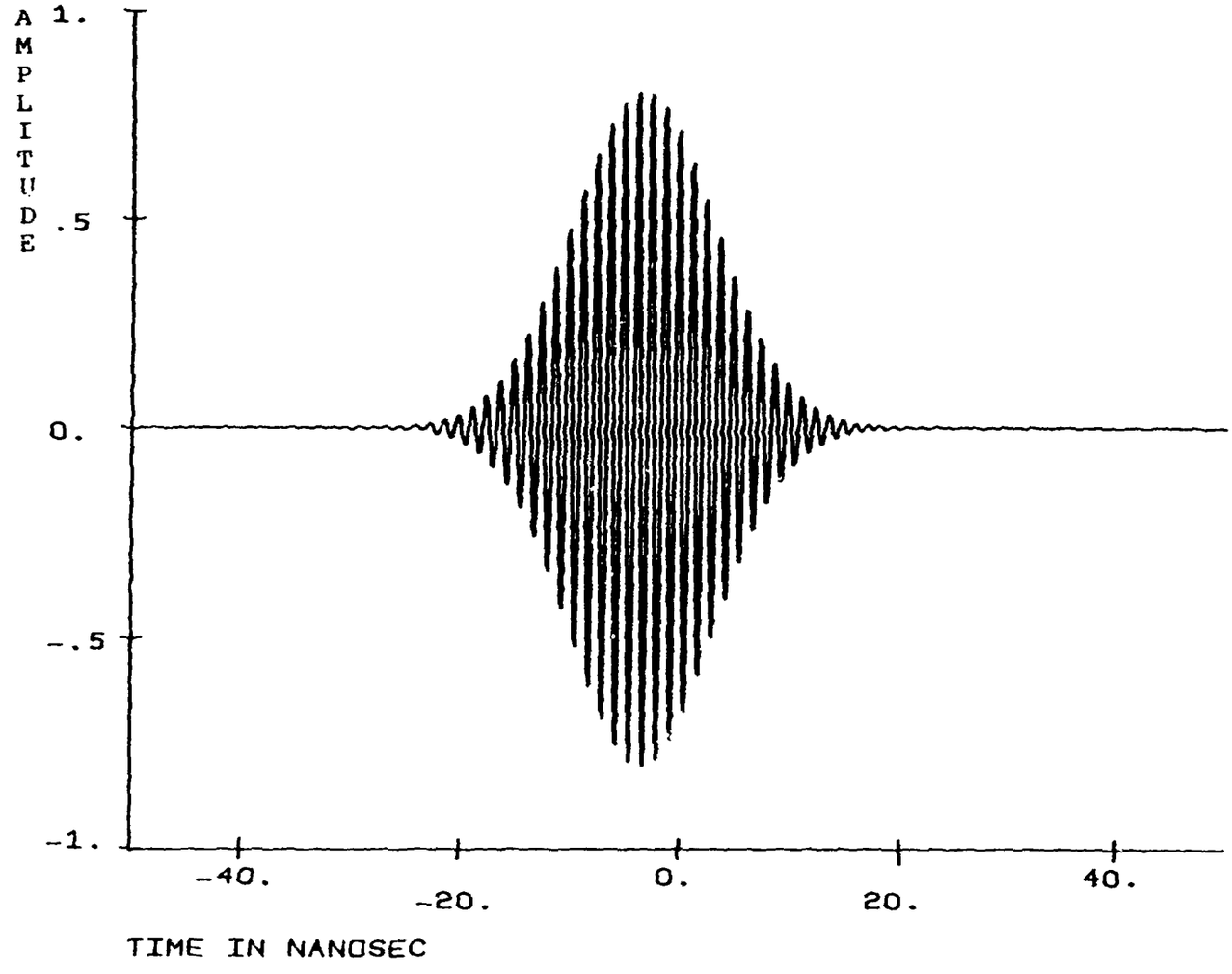

Figure 20- The output pulse at x=5.297 km.

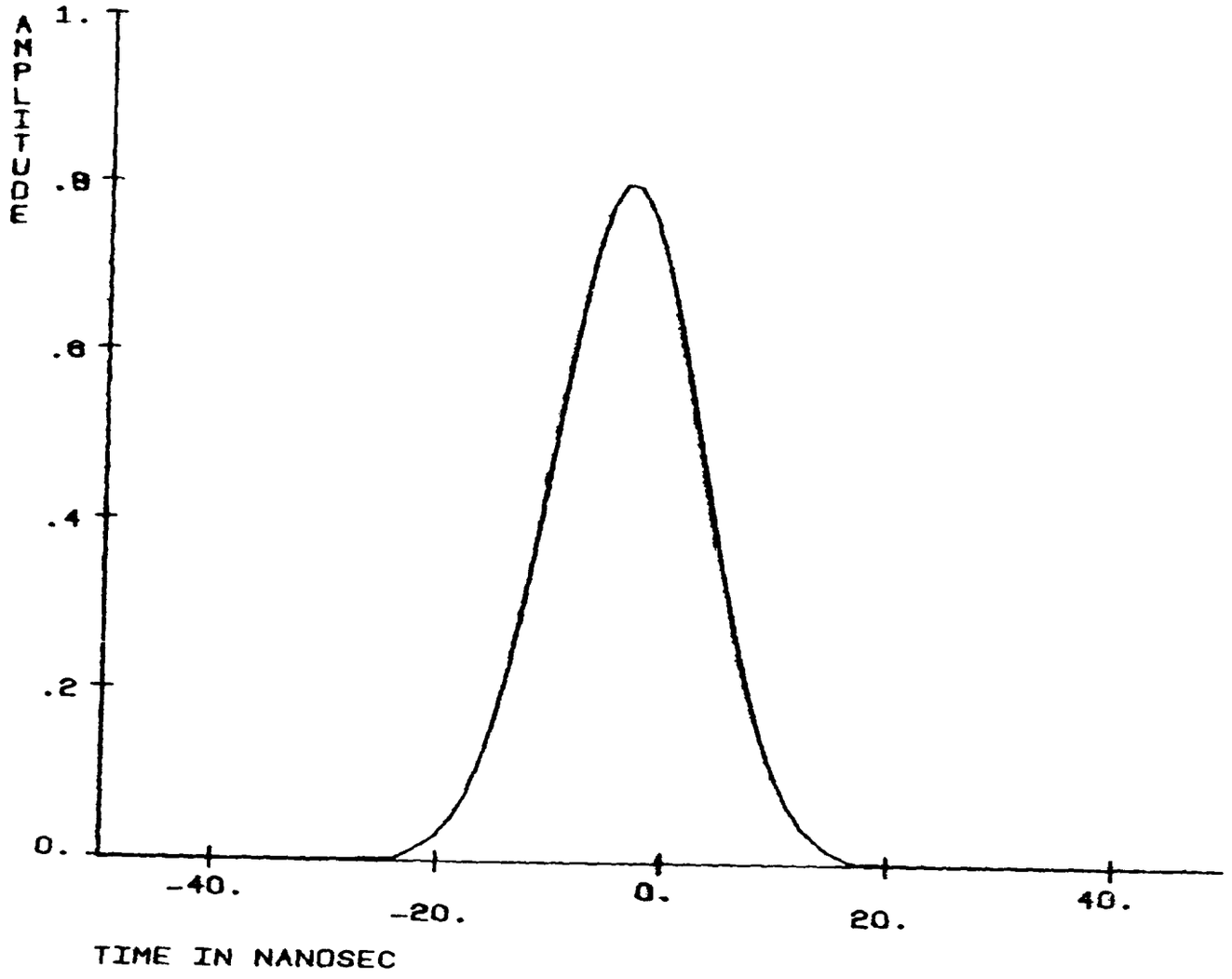

Figure 21- The output pulse envelope at x=5.297 km.

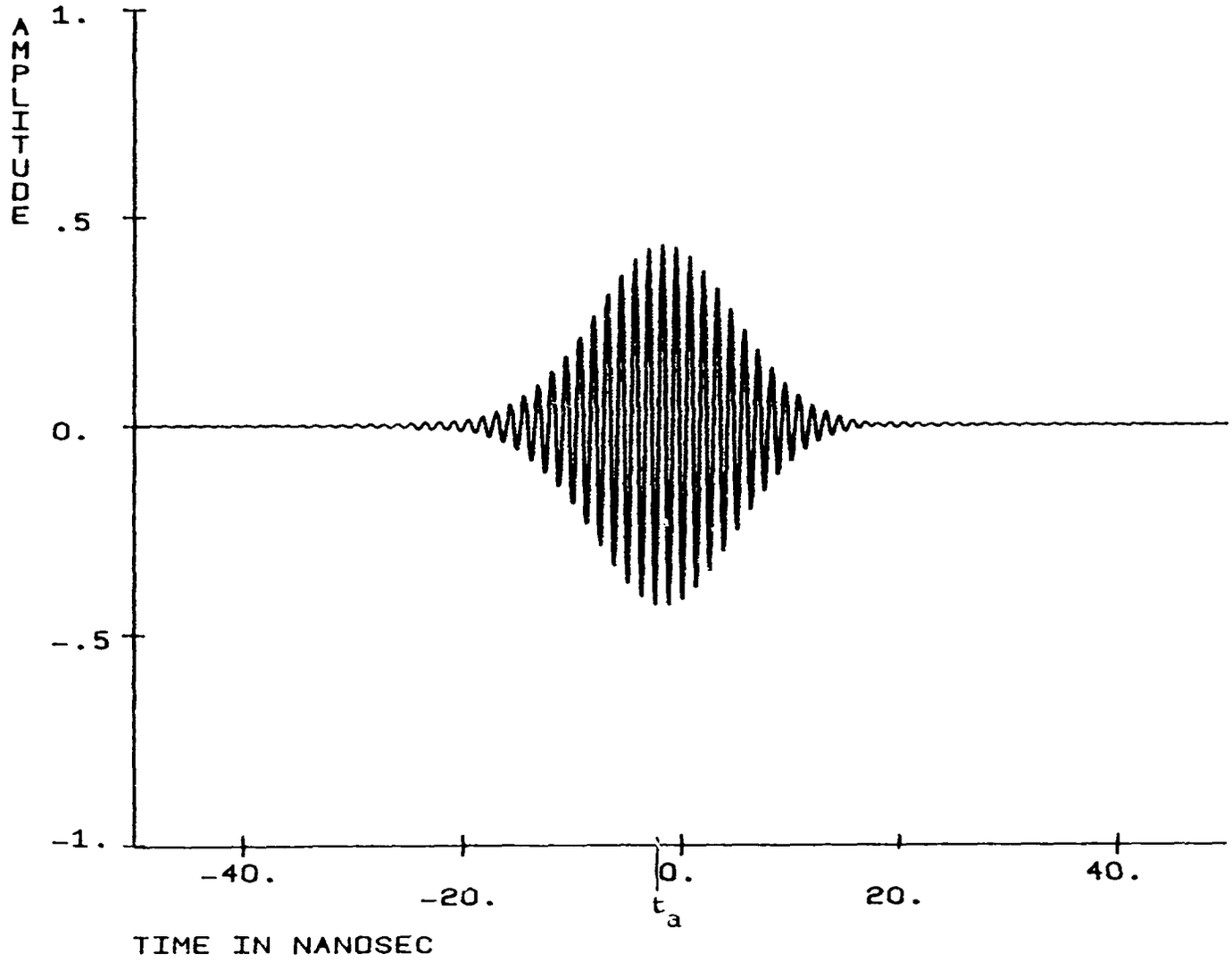

Figure 22- The output pulse at x=8.856 km.

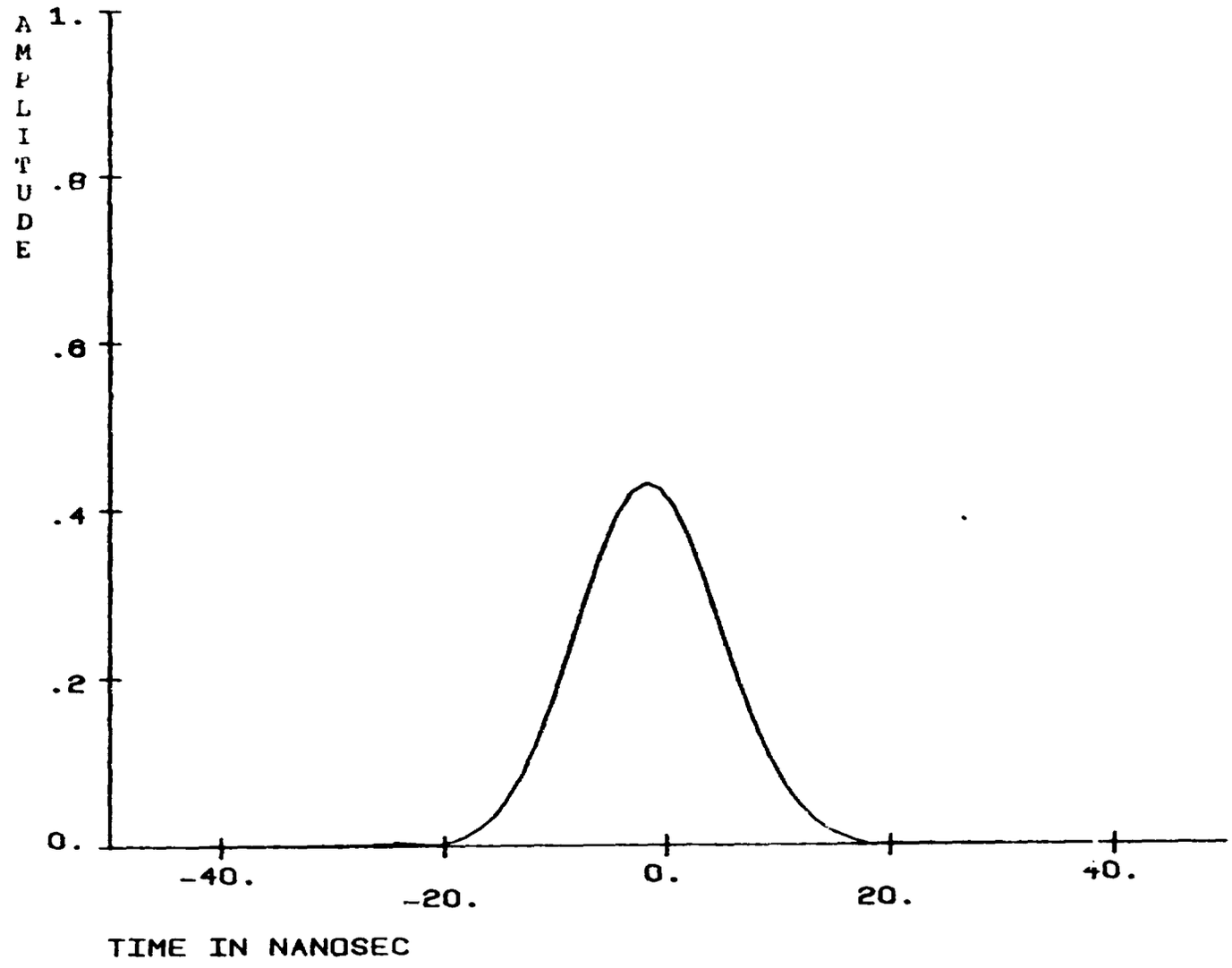

Figure 23- The output pulse envelope at x=8.656 km.

pulse envelope for x=8.856 km respectively for the 6.51 nanosecond, 800 MHz pulse (one of the twelve carrier frequency and pulse width combinations analyzed). In Figure 17 (the input pulse), the leading edge of the pulse is in positive time and the trailing edge of the pulse is in negative time. The pulse is centered at time zero. Figures 22 and 23 clearly show an example of pulse distortion. In Figure 22, the delayed mean arrival time (t_a) is marked. A pulse propagating through free space the same distance would be centered at t=0. The mean arrival time is the excess delay caused by the electron bubble medium.

The normalized moments of the output pulse envelopes are plotted versus frequency in Figures 24-29. Figures 24-26 are for the pulse width equal to 6.51 nanoseconds and Figures 27-29 are for the pulse width equal to 12.95 nanoseconds. The dashed lines are the data for x=5.297 km and the solid lines are for x=8.856 km.

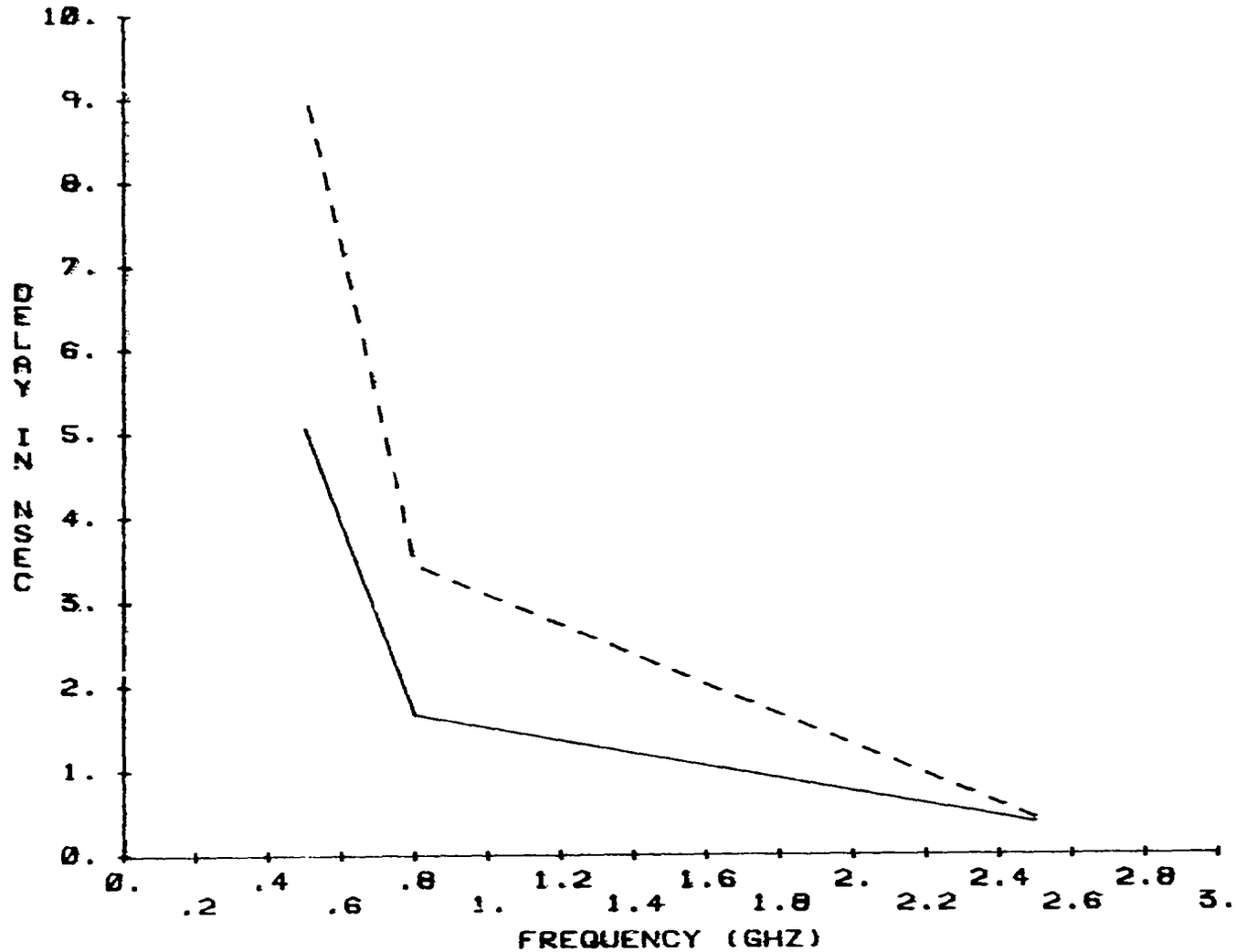

Figure 24- The delay data for the applied pulse of 6.51 nanoseconds pulsewidth.

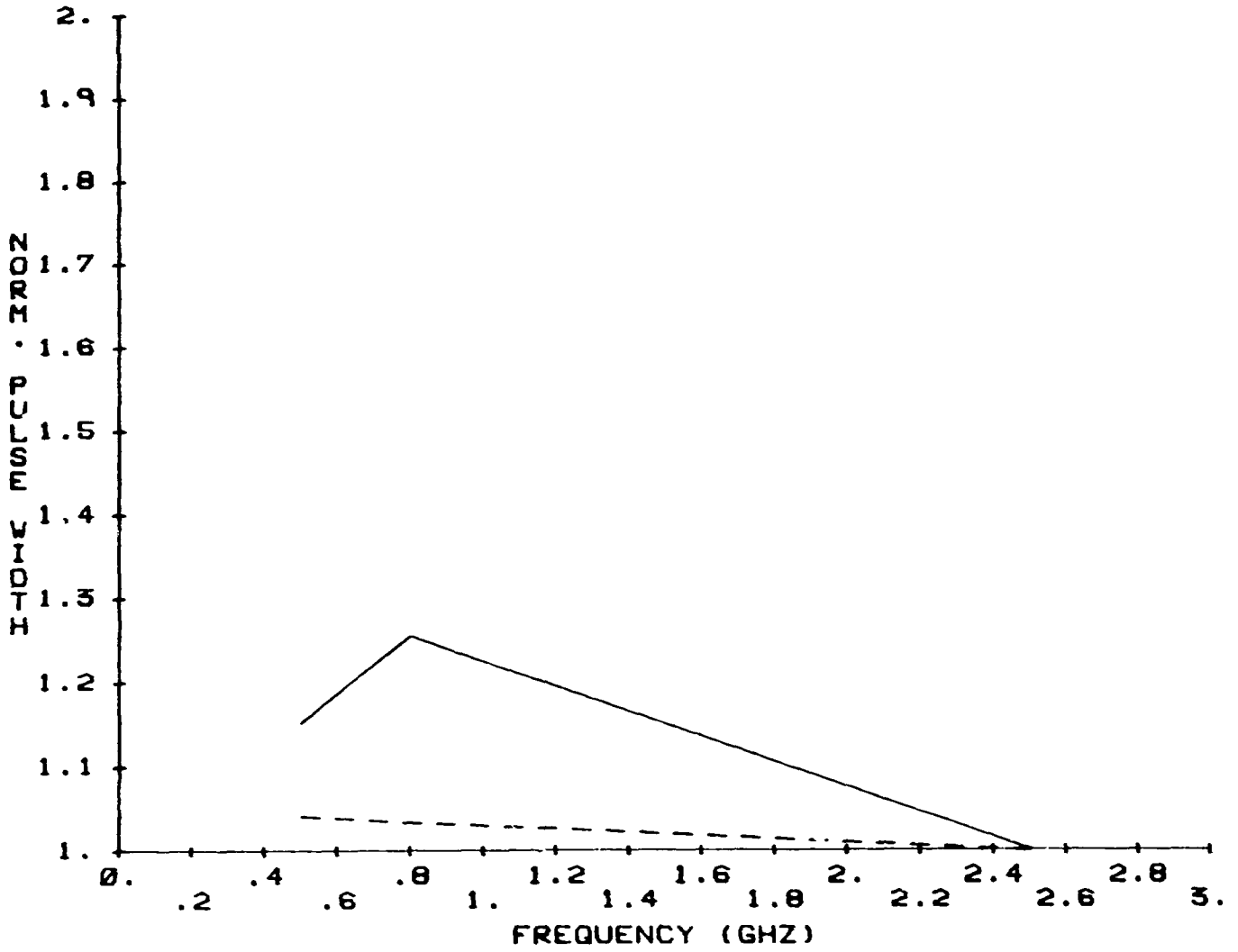

Figure 25- The pulsewidth data for the applied pulse of 6.51 nanoseconds pulsewidth.

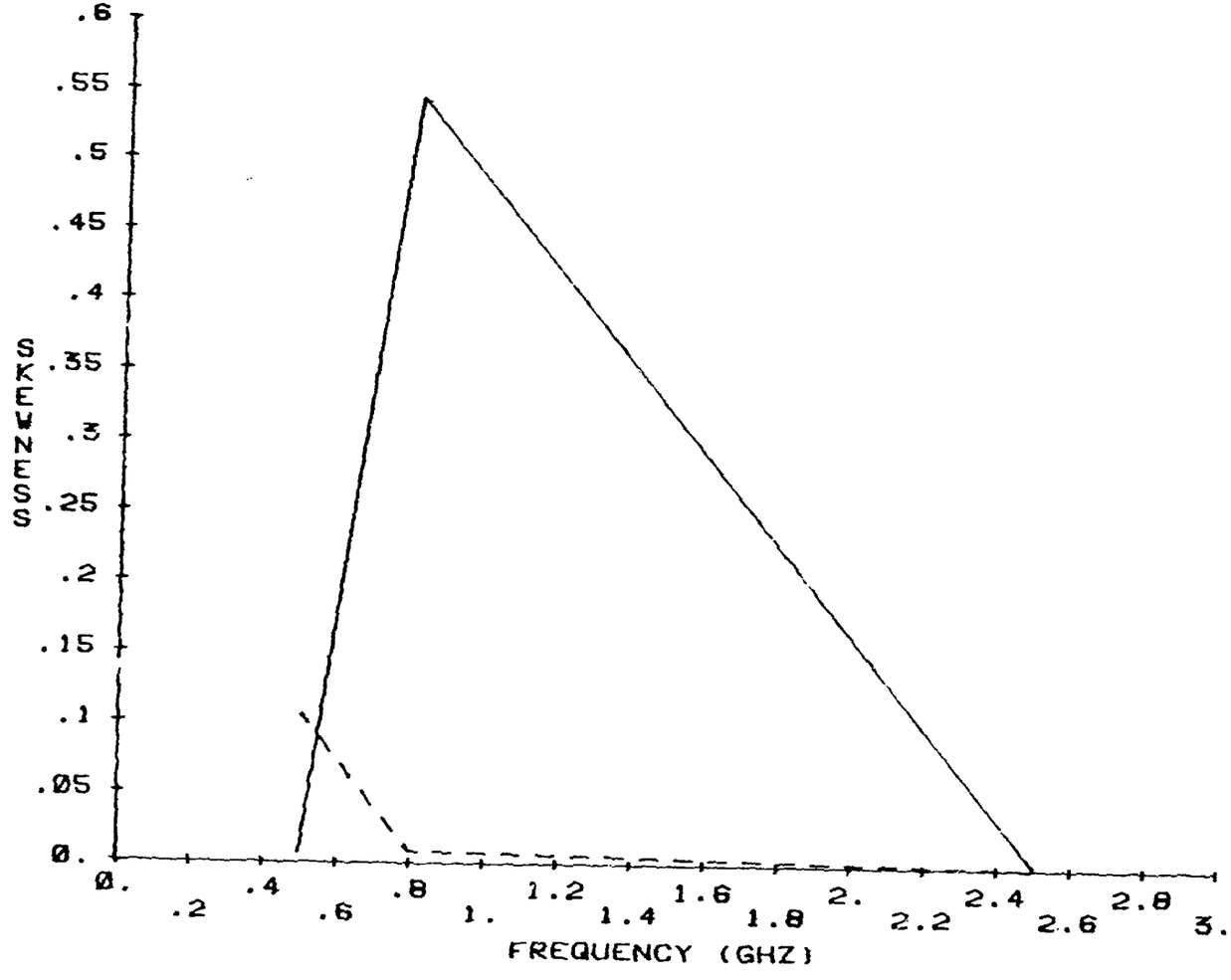

Figure 26- The skewness data for the applied pulse of 6.51 nanoseconds pulsewidth.

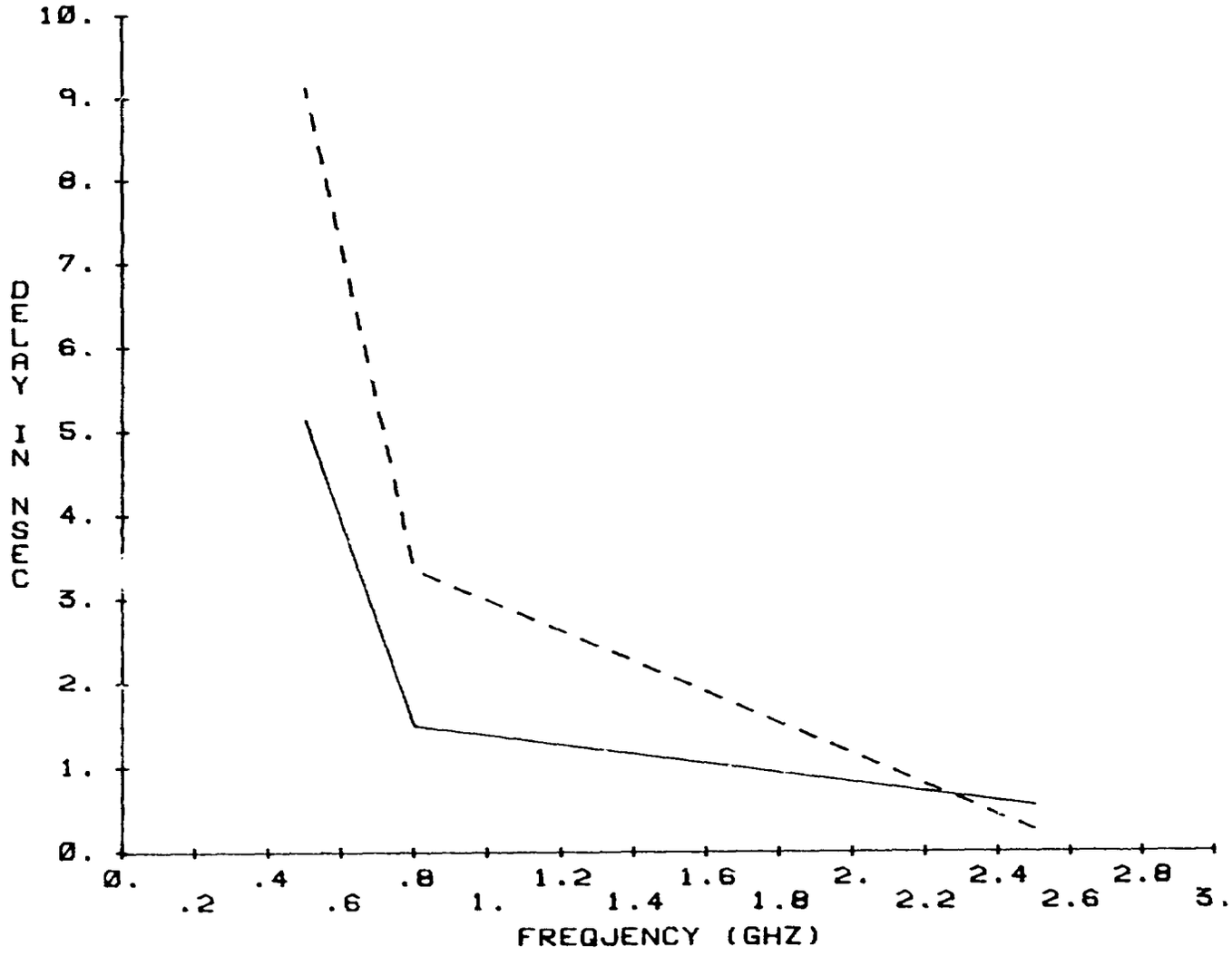

Figure 27- The delay data for the applied pulse of 12.95 nanoseconds pulsewidth.

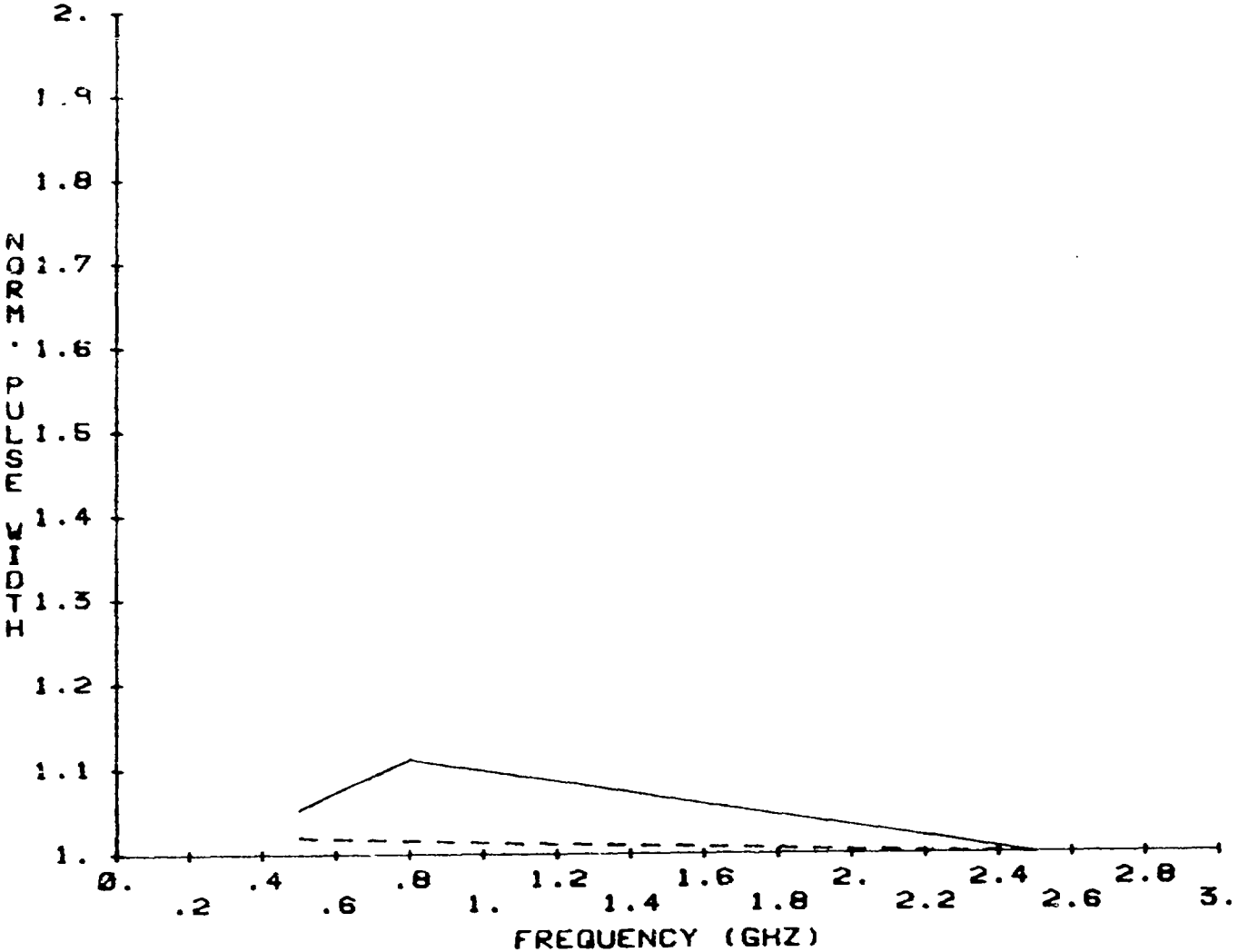

Figure 28- The pulsewidth data for the applied pulse of 12.95 nanoseconds pulsewidth.

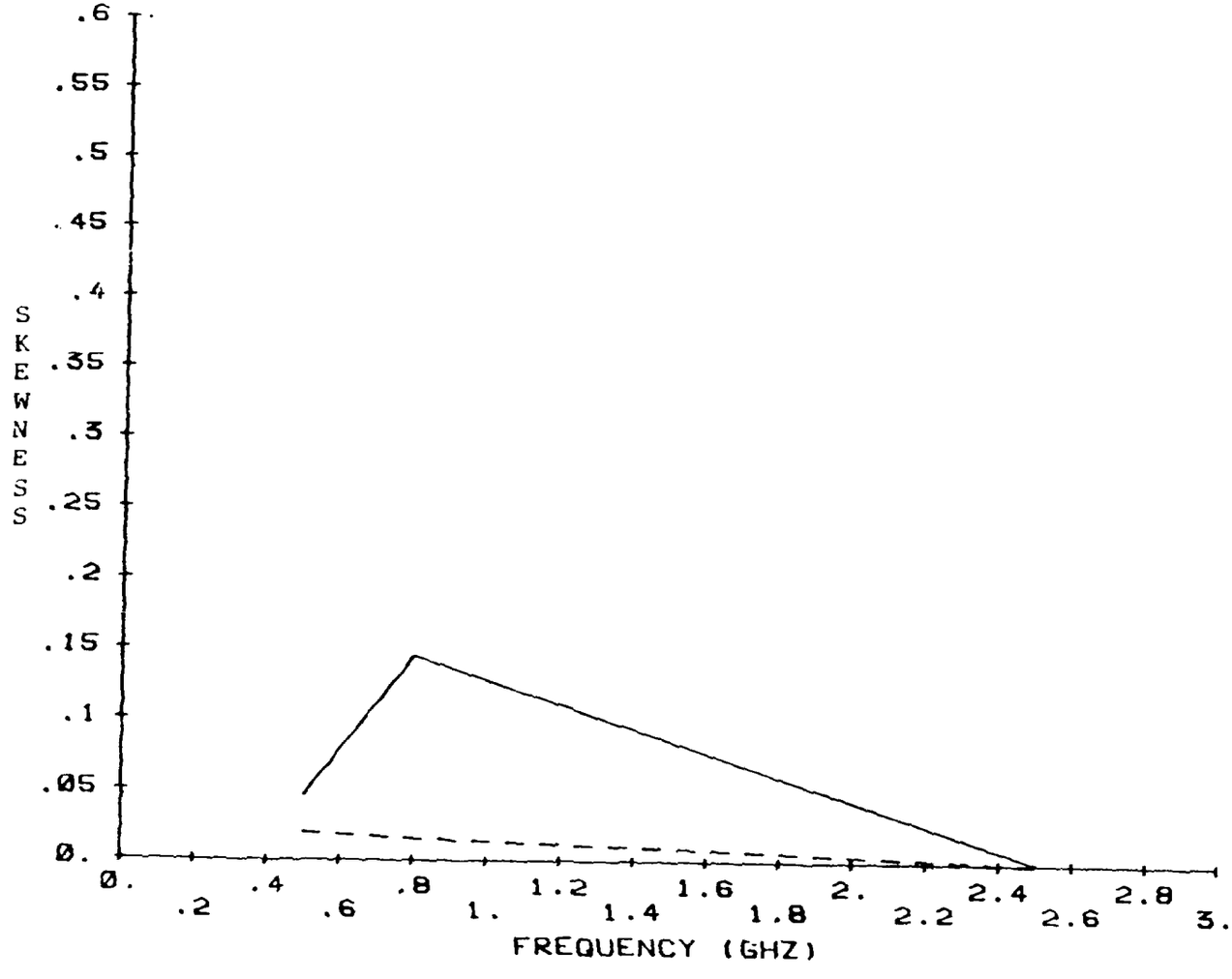

Figure 29- The skewness data for the applied pulse of 12.95 nanoseconds pulsewidth.

6.0 Analysis

In section 2.1 the fluctuating part of the relative dielectric permittivity was derived as Equation (29).

$$\varepsilon_1(\underline{r}) = \frac{\left(\frac{\omega_{p_0}^2(z)}{\omega^2}\right)\left|\frac{\Delta N(\underline{r})}{N_0(z)}\right|}{1-(\omega_{p_0}(z)/\omega)^2}$$

As the wave frequency is made larger, $\varepsilon_1(\underline{r})$ tends toward zero. Thus for high frequencies the fluctuations in electron density will have little effect on a propagating wave. The wave will propagate like the medium is free space. However, at lower frequencies, the electron density fluctuations will have a great effect. Also the effect will be different for every frequency across the pulse bandwidth. Thus a low carrier frequency pulse propagating through an electron bubble medium will be distorted.

To analyze the results, the moments of the pulse envelope must be related to its frequency spectrum. The moment theorem [Papoulis, (1962)], relates the derivatives of $F(\omega)$ at the origin to the moments of the time function. In this problem, a carrier frequency shifts the frequency spectrum of the envelope to the carrier frequency so the moments of the envelope will be related to the derivatives of its frequency spectrum at the carrier frequency. In addition to the shifting, the frequency spectrum is also multiplied by a factor of 1/2.

The moment theorem which relates the derivatives of the frequency spectrum to the moments of the pulse envelope is

$$(-i)^n M_n = \frac{2d^n F(\omega)}{d\omega^n}\Big|_{\omega=\omega_c} \qquad (74)$$

The frequency spectrum of the envelope is written in terms of a magnitude part and a phase part.

$$F(\omega) = H(\omega)e^{i\phi(\omega)} \tag{75}$$

Since the pulse $p_0(t)$ is real, $H(\omega)$ is even and $\phi(\omega)$ is odd. $H(\omega)$ and $\phi(\omega)$ are expanded in a Taylor series about the carrier frequency ω_c.

$$H(\omega) = 1 + \frac{h_2(\omega-\omega_c)^2}{2!} + \ldots \tag{76}$$

$$\phi(\omega) = b_1(\omega-\omega_c) + \frac{b_3}{3!}(\omega-\omega_c)^3 + \ldots \tag{77}$$

where

$$h_2 = \frac{d^2}{d\omega^2} H(\omega)\Big|_{\omega=\omega_c}$$

$$b_1 = \frac{d\phi(\omega)}{d\omega}\Big|_{\omega=\omega_c}$$

$$b_3 = \frac{d^3\phi(\omega)}{d\omega^3}\Big|_{\omega=\omega_c}$$

Using the series representation for the exponential

$$e^{+i\phi(\omega)} = 1+b_1(\omega-\omega_c) + \frac{ib_3}{3!}(\omega-\omega_c)^3 - \frac{b_1^2}{2!}(\omega-\omega_c)^2 - \frac{ib_1^3}{3!}(\omega-\omega_c)^3 \tag{78}$$

therefore

$$F(\omega) = \left[1 + \frac{h_2}{2!}(\omega-\omega_c)^2 + \ldots\right]\left[1+ib_1(\omega-\omega_c) + \frac{ib_3}{3!}(\omega-\omega_c)^3 - \frac{b_1^2}{2!}(\omega-\omega_c)^2 - \frac{ib_1^3}{3!}(\omega-\omega_c)^3 + \ldots\right] \tag{79}$$

or

$$F(\omega) = 1+ib_1(\omega-\omega_c) + \frac{h_2-b_1^2}{2!}(\omega-\omega_c)^2 - \frac{i}{3!}(b_1^3-3h_2b_1-b_3)(\omega-\omega_c)^3+ \ldots \tag{80}$$

The pulse is written as an envelope function multiplied by a complex sinusoid

$$p_0(t) = A(t)\, e^{+i\omega_c t} \tag{81}$$

so

$$F(\omega) = \int_{-\infty}^{\infty} A(t)e^{-i(\omega-\omega_c)t}\, dt \tag{82}$$

Using the series representation for the exponential gives

$$F(\omega) = \int_{-\infty}^{\infty} A(t) \left[\sum_{n=0}^{\infty} \frac{-i(\omega-\omega_c)t)^n}{n!} \right] dt \tag{83}$$

integrating (83) termwise gives

$$F(\omega) = \sum_{n=0}^{\infty} \frac{(-i)^n(\omega-\omega_c)^n}{n!} M_n \tag{84}$$

and substituting (74) into (84) results in

$$F(\omega) = \sum_{n=0}^{\infty} \frac{2d^nF(\omega)}{d\omega^n} \frac{(\omega-\omega_c)^n}{n!} \tag{85}$$

Assuming $M_0=1$ and equating the terms of (84) and (80) results in

$$b_1 = -M_1 = \frac{d\phi(\omega)\,|\,\omega=\omega_c}{d\omega} \tag{86}$$

$$h_2 = M_1^2-M_2 = \frac{d^2H(\omega)\,|\,\omega=\omega_c}{d\omega^2} \tag{87}$$

$$M_3 = -(b_1^3-3b_1h_2-b_3) \tag{88}$$

and defining

$$t_m = \int_{-\infty}^{\infty} tA(t)dt \tag{89}$$

$$\sigma^2 = \int_{-\infty}^{\infty} (t-t_m)^2 A(t)dt \tag{90}$$

$$\delta = \int_{-\infty}^{\infty} (t-t_m)^3 A(t)dt \tag{91}$$

gives

$$t_m = \frac{-d\phi(\omega)\,|\,\omega=\omega_c}{d\omega} \tag{92}$$

$$\sigma^2 = \frac{-d^2H(\omega)\,|\,\omega=\omega_c}{d\omega^2} \tag{93}$$

$$\delta = \frac{d^3\phi(\omega)\,|\,\omega=\omega_c}{d\omega^3} \tag{94}$$

Thus the delay is related to the slope of the phase function at the carrier frequency and the pulse spreading is related to the curvature of the amplitude function at the carrier frequency. The skewness is related to the 3rd derivative of the phase function. Note that the delay, pulsewidth and skewness defined above are slightly different than the quantities defined in Section 4. The definitions above are related to the envelope while the definitions in Section 4 are related to the square of the envelope (since the pulses are real). In the next several paragraphs, the above derivations will be used to qualitatively explain the output pulses due to several different transfer functions. The delay, pulsewidth and skewness of the square of the envelope are directly related to the delay, pulsewidth and skewness of the envelope itself.

According to Equation (29), one would expect pulse distortion to become greater when the carrier frequency is decreased. Thus the pulse width and the skewness should become greater when the carrier frequency is decreased. That is exactly what is observed in Figures 25, 26, 28, and 29 when the receiver is placed at x=5.297 km. But when the receiver is placed at x=8.856 km, something different is observed. From 2.5 GHz to 800 MHz the expected distortion versus frequency occurs. But at 500 MHz the distortion becomes less. By studying Figures 12 and 16 one can see why the distortion is less at the lower frequency. In Figure 12, the 800 Mhz phase transfer function, there is a non-linearity near the center of the bandwidth. In Figure 16, the 500 MHz phase transfer function, the phase is nearly linear near the center of the pulse bandwidth. According to Equation (92), non-linear phase causes pulse distortion because delay is dependent on the derivative of the phase function. Delay as a function of frequency (D(f) is written as

$$D(f) = \frac{-d\phi(f)}{df} \tag{95}$$

If the phase is non-linear, some of the frequency components in the pulse are delayed different amounts of time than other components. Thus the pulse is distorted. So one reason the 800 MHz pulse is distorted more than the 500 MHz pulse is because the phase is more non-linear near the center of the 800 MHz phase transfer function.

Figures 11 and 15 can be used to explain why the pulsewidth decreases at 500 MHz for x=8.856 km. When the amplitude spectrum of the input pulse is multiplied by the transfer function of Figure 11 a large amount of negative curvature at the carrier frequency results. However when the amplitude spectrum of the input pulse is multiplied

by the transfer function of Figure 15, less negative curvature at the carrier frequency results because in Figure 15 there is a large amount of positive curvature which tends to cancel some of the negative curvature of the input spectrum. According to Equation (93), the pulsewidth is related to the negative curvature of the amplitude function at the carrier frequency. Thus the output pulse due to the transfer function of Figure 11 will be spread in time more than the output pulse due to the transfer function of Figure 15.

Figure 12 can also be used to justify the large skewness value at x=8.856 km for the 800 MHz carrier frequency. Since skewness is related to the 3rd derivative of the phase function according to Equation (94), the transfer function of Figure 12 would give rise to a large skewness value because of the non-linearities in the phase near the center of the bandwidth.

At first the above results might be considered disturbing because Equation (29) predicts that the pulse distortion should rise as the carrier frequency is decreased. However, more analysis could easily rationalize the results. If a receiver was placed at every x point below the bubble and if a pulse was applied at every x point above the bubble, on the average the expected pulse distortion would occur.

In the real ionosphere, the electron bubble would be moving relative to the line of propagation. If a pulse train was transmitted, the delay, pulsewidth and the skewness of each successive pulse would vary. But on the average, the delay, pulsewidth and skewness would rise if the carrier frequency of the pulse train was decreased.

In order to use this computer model to study this propagation problem in greater detail, a receiver would have to be placed at every x position. To do that would require a very large computer budget.

References

Ames, W. F., Numerical Methods for Partial Differential Equations, Barnes and Noble, Inc., New York, 1969.

Chen, C. T., One Dimensional Digital Signal Processing, Marcel Dekker Inc., New York, 1979.

Ishimaru, Akira, Theory and Application of Wave Propagation and Scattering in Random Media, Proceedings of the IEEE, Vol. 65, No. 7, July 1977.

Ishimaru, Akira, Wave Propagation and Scattering in Random Media, Volume 2, Academic Press, New York, 1978.

Jordan, E. and Balman, K., Electromagnetic Waves and Radiating Systems Second Edition, Prentice-Hall, Inc., Englewood Cliffs, N.J., 1968.

Liu, C. H. and Yeh, K. C., Pulse Propagation in Random Media, Dept. of E.E., University of Illinois, July 1978.

McClure, J. P., Hanson, W. B., and Hoffman, J. H., Plasma Bubbles and Irregularities in the Equatorial Ionosphere, J. Geophys. Res., V. 82, pp. 2650-2656, 1977.

Papoulis, A., The Fourier Integral and its Applications, McGraw Hill Book Comp., Inc., New York, 1962.

Tatarskii, V. I., The Effects of the Turbulent Atmosphere on Wave Propagation, U.S. Dept. of Commerce, National Technical Information Service, Springfield, Va., 1971.

Wernik, A. W., Model Computations of Radio Wave Scintillation Caused by Equatorial Bubbles. Dept. of E.E., University of Illinois, July 1979.

Wernik, A. W., Liu, C. H. and Yeh, K. C., Model Computations of Radio Wave Scintillation Caused by Equatorial Ionospheric Bubbles, Radio Science, Vol. 15, No. 3, pp. 559-572, May-June 1980.

Wong, Y. K., Mean Arrival Time and Mean Pulse Width of Signals Propagating Through an Inhomogeneous Ionosphere with Random Irregularities, Masters Thesis, University of Illinois, 1978.

Yang, C. C., Temporal Behavior of Pulses After Propagating Through a Turbulent Ionosphere, Masters Thesis, University of Illinois, 1981.

Appendix A

The software procedure used to obtain the moments for a pulse envelope is shown below. Each of the programs is explained and listed in this appendix.

1. Program SHEET 1

This program numerically solves the parabolic equation for a wave propagating through the model electron bubble. Program SHEET 1 is explained fully in section 3.2.

2. Program Pulse

This program computes the frequency spectrum of the incident pulse from the time function. The frequency spectrum is computed using the Discrete Fourier Transform via a standard decimation in time FFT routine.

The pulse time function is set up in an array. The frequency spectrum is computed using the DFT.

$$F_i(m\rho) = \sum_{n=0}^{N-1} p_i(nT) e^{-i\left(\frac{2\pi}{N}\right)mn}$$

where

$N = 8192$

$p_i(nT)$ = the pulse time function

$m = 0,1,2,\ldots N-1$

T = sampling rate

The frequency spectrum is computed for N values in the range $m\rho=(0,2\pi)$ radians. To obtain the actual frequency scale, the following relationship is used

$$\omega T = \rho$$

So

$$F_i(m\omega) = F_i(m\omega T)$$

In this thesis, I will adjust T each time the carrier frequency is changed so that the 1024th point of the frequency spectrum array corresponds to the carrier frequency.

3. Program INTER

This program interpolates between the nine SHEET 1 solutions to obtain a parabolic equation solution corresponding to each of the points in the frequency spectrum computed by program PULSE. Two linear interpolations are done, one for the amplitude and one for the phase.

4. Program MULT

This program multiplies the interpolated parabolic equation solutions and the input pulse frequency spectrum to obtain the output pulse frequency spectrum.

5. Program IFFT

Program IFFT calculates the output pulse time function from the frequency spectrum using the inverse Discrete Fourier Transform via a standard decimation in time FFT routine. The inverse DFT is given by

$$p_0(nT) = \frac{1}{N} \sum_{m=0}^{N-1} F_0(m\omega) e^{i(\frac{2\pi}{N})mn}$$

where:

$N = 8192$

$n = 0,1,2,....N-1$

$F_0(m\omega)$ = output pulse frequency spectrum

$p_0(nT)$ = output pulse time function

T = sampling rate

6. Program ENVEL

Program ENVEL finds the envelope of the output pulse and then calculates the first four moments.

```
      PROGRAM SHEET1(INPUT,OUTPUT,ELFL,RESULT,PASS,DA2,
     +TAPE1=RESULT,TAPE2=ELFL,TAPE3=DA2,TAPE5=PASS,
     +TAPE6=OUTPUT)
C*****************************************************************
C
C...THIS PROGRAM SOLVES THE PARABOLIC EQUATION NUMERICALLY
C...FOR A WAVE PROPAGATING IN THE IRREGULAR IONOSPHERE
C...OR IN FREE SPACE.
C
C*****************************************************************
C
C*****************************************************************
C
C...THE 4 INPUT/OUTPUT FILES PREFORM THE FOLLOWING FUNCTIONS:
C
C           (1) DA2 CONTAINS INPUT PARAMETERS
C               K,N,TAU,H,SIGM,FREQ,KSKIP,
C               XM,KK,KL,AL,BET,Z0,Z00,EMAX,EZ,ZMAX.
C           (2) ELFL CONTAINS INFORMATION ABOUT THE HORIZONTAL
C               ELECTRON DENSITY STRUCTURE.
C           (3) RESULT CONTAINS THE SOLUTIONS TO THE PARABOLIC
C               EQUATION AT EACH HEIGHT Z AND EACH X STEP.
C           (4) PASS IS THE RENAMED FILE RESULT.  PASS IS USED
C               IF FURTHER COMPUTATIONS ARE TO BE DONE IN FREE
C               SPACE BELOW THE BUBBLE.
C
C*****************************************************************
C*****************************************************************
C
C...THE 4 SUBROUTINES PREFORM THE FOLLOWING FUNCTIONS
C
C           (1) UO SETS THE INTIAL VALUES ON THE WAVE AT Z=0.
C           (2) FLUCT CALCULATES THE FLUCTUATING PART OF THE
C               DIELECTRIC PERMITTIVITY AND CALCULATES THE F
C               FUNCTION.
C           (3) DCALC CALCULATES THE MATRIX EQUATION D=A*U.
C           (4) THOMAS SOLVES THE MATRIX EQUATION B*X=D USING
C               GAUSSIAN ELIMINATION VIA THE THOMAS ALGORITHM.
C
C*****************************************************************
C
C...THE INPUT PARAMETERS IN DA2 ARE:
C
C           (1) K THE NUMBER OF STEPS IN THE X DIRECTION.
C           (2) N THE NUMBER OF STEPS IN THE Z DIRECTION.
C           (3) H THE STEP SIZE IN THE X DIRECTION IN METERS.
C           (4) TAU THE STEP SIZE IN THE Z DIRECTION IN
C               METERS.
C           (5) SIGM A FACTOR USED IN THE NUMERICAL PARABOLIC
C               EQUATION SOLUTION. (SEE REPORT)
C           (6) FREQ THE WAVE FREQUENCY IN MHZ.
C           (7) KSKIP THE NUMBER OF STEPS IN THE Z DIRECTION
```

```
C                RECORDED ON FILE PASS. IF KSKIP IS NOT EQUAL
C                TO ZERO THEN PASS IS AUTOMATICALLY READ AND
C                ELFL IS NOT READ.
C           (8)  ZM ONLY EVERY ZM STEP IN THE Z DIRECTION IS
C                RECORDED ON FILE RESULT.
C           (9)  KK ONLY EVERY KK STEP IN THE X DIRECTION IS
C                RECORDED ON FILE RESULT.
C          (10)  KL THE NUMBER OF STEPS IN THE Z DIRECTION
C                COMPUTED IN ALL PREVIOUS RUNS.
C          (11)  AL A FACTOR USED IN THE WEIGHTING FUNCTION.
C          (12)  BET A FACTOR USED IN THE WEIGHTING FUNCTION.
C          (13)  Z0 A FACTOR USED IN THE WEIGHTING FUNCTION.
C          (14)  Z00 A FACTOR USED IN THE WEIGHTING FUNCTION.
C          (15)  EMAX A FACTOR USED TO COMPUTE THE PARABOLIC
C                PROFILE. THE ELECTRON DENSITY IN
C                ELECTRONS/CM**3 AT ZMAX.
C          (16)  EZ THE ELECTRON DENSITY IN ELECTRONS/CM**3
C                AT Z=0.
C          (17)  ZMAX THE HEIGHT OF THE MAXIMUM ELECTRON
C                DENSITY IN THE PARABOLIC PROFILE.
C
C*******************************************************************
C*******************************************************************
      COMMON/AAA/ELX(800)
      COMMON/BBB/FREQ,H,N,TAU,PI,XKI
      COMMON/CCC/AL,BET,EMAX,EZ,ZMAX,Z0,Z00
      COMPLEX AK(800),CK(800),U(800),CCK(800),D(800)
     +,X(800),AAK(800)
      DIMENSION F(800),AMP(800),PH(800),TEMP(2,800)
      INTEGER ZM
C
C...READ THE INPUT PARAMETER FROM FILE DA2.
C
      READ(3,100)K,N,TAU,H,SIGM,FREQ,KSKIP
      READ(3,125)ZM,KK,KL
      READ(3,150)AL,BET,Z0,Z00,EMAX,EZ,ZMAX
C
C...NORMALIZE THE STEP SIZE TO THE WAVE NUMBER AND SET THE
C...VALUE FOR PI. THIS IS EQUATION (35).
C
      PI=4.0*ATAN(1.)
      XKI=300./(2*PI*FREQ)
      TAU=TAU/XKI
      H=H/XKI
C
C...IF KSKIP IS NOT EQUAL TO ZERO THEN THE COMPUTATIONS WILL
C...BE DONE OUTSIDE THE IRREQULAR MEDIUM.  THE FILE ELFL
C...DOES NOT NEED TO BE READ AND THE INITIAL VALUES FOR
C...THE U MATRIX ARE OBTAINED FROM THE PREVIOUS
C...COMPUTATIONS IN FILE PASS.
C
      IF(KSKIP.NE.0)GO TO 15
```

```
C
C...READ THE FILE ELFL WHICH CONTAINS THE ELECTRON DENSITY
C...INFORMATION OF FIGURE 2. THIS INFORMATION IS STORED
C...IN ELX.
C
      READ(2,175)(ELX(I),I=1,K)
C
C...IF FILE PASS HAS NO VALUES STORED IN IT, THE COMPUTATIONS
C...START AT Z=0 AND THE PARAMETERS ARE OUTPUT TO
C...FILE RESULT.
C
      KL=N
      T=TAU*XKI
      H1=H*XKI
      WRITE(1,200)K,N,T,H1,SIGM,FREQ,KL,KSKIP
      WRITE(1,225) KK,ZM
C
C...THE U MATRIX IS THE COMPLEX AMPLITUDE OF THE WAVE.
C...SUBROUTINE UO IS CALLED TO SET THE INITIAL CONDITIONS
C...OF U.
C
      CALL UO(U,K)
      GO TO 11
C
C...THIS IS THE BRANCH POINT IF KSKIP IS NOT EQUAL TO ZERO
C...AND THE FILE PASS NEEDS TO BE READ. IN THIS CASE THE
C...INTIAL VALUES OF U ARE OBTAINED FROM PREVIOUS
C...COMPUTATIONS STORED IN FILE PASS.
C
 15   READ(5,250) K,N,TAU,H,SIGM,FREQ,KL,KSKIP
      READ(5,275) KK,ZM
           DO 16 L=1,KSKIP
           READ(5,300)(TEMP(1,I),TEMP(2,I),AMP(I),PH(I),I=1,K)
 16        CONTINUE
           DO 17 I=1,K
           U(I)=CMPLX(TEMP(1,I),TEMP(2,I))
 17        CONTINUE
 11 CONTINUE
C
C...THE NUMERICAL SOLUTION TO THE PARABOLIC EQUATION BEGINS.
C
C...THE TWO MATRICES OF EQUATION (43) A AND B ARE STORED IN
C...THREE ARRAYS EACH. FOR A, THE THREE ARRAYS ARE AK,CK,BK.
C...AK AND BK STORE THE OFF DIAGONAL ELEMENTS OF A
C...AND CK STORES THE DIAGONAL ELEMENTS OF A.  SIMILARILY,
C...AAK, BBK, CCK STORE THE ELEMENTS OF MATRIX B.
C...SINCE THIS PROBLEM HAS SPECIAL SYMMETRY AK=BK AND
C...AAK=BBK SO THESE ARRAYS ARE NOT STORED TWICE.
C
C...THE AK AND AAK MATRICES ARE SET UP ACCORDING TO EQUATIONS
C...(45-48).
C
```

```
            DO 1 I=1,K
            R=0.0
            AI=0.5/(H*H)
            AK(I)=CMPLX(R,AI)
            R=0.0
            AI=(.5/(H*H))*TAU*SIGM
            AAK(I)=CMPLX(R,AI)
 1          CONTINUE
C
C...NOW THE MAIN LOOP BEGINS.  FIRST THE DIAGONALS OF THE
C...A AND B MATRICES ARE SET UP. BY EQUATIONS (45-48)
C...IT CAN BE SEEN THAT THESE VALUES DEPEND ON THE ELECTRON
C...DENSITY FLUCTUATIONS.  IF THE COMPUTATIONS ARE TO BE
C...DONE IN FREE SPACE THERE ARE NO ELECTRON DENSITY
C...FLUCTUATIONS SO THE F.FUNCTION IS SET TO ZERO.
C
            DO 2 J=1,N
                 DO 3 I=1,K
                 F(I)=0.0
 3               CONTINUE
            IF(KSKIP.NE.0) GOTO 5
            CALL FLUCT(F,J,K)
 5               DO 6 I=1,K
                 R=0.0
                 AI=-1.0/(H*H)+F(I)/2
                 CK(I)=CMPLX(R,AI)
                 R=1.0
                 AI=-(TAU*SIGM)/(H*H)+F(I)*SIGM*TAU/2
                 CCK(I)=CMPLX(R,AI)
 6               CONTINUE
C
C...NEXT THE PRODUCT OF TWO MATRICES D=A*U IS CALCULATED IN
C...DCALC.
C
            CALL DCALC(AK,AK,CK,U,D,K)
C
C...NOW THE SYSTEM OF EQUATIONS IS SOLVED VIA THE THOMAS
C...ALGORITHM. X=(B INVERSE)*A*U. THIS IS EQUATION (51).
C
            CALL THOMAS(AAK,AAK,CCK,X,D,K)
C
C...FINALLY THE EQUATION U(N+1)=U(N)-X*TAU IS CALCULATED.
C...EQUATION (49).
C
                 DO 4 I=1,K
                 R=REAL(U(I))-TAU*REAL(X(I))
                 AI=AIMAG(U(I))-TAU*AIMAG(X(I))
                 U(I)=CMPLX(R,AI)
 4               CONTINUE
C
C...THE MAGNITUDE AND PHASE OF THE COMPLEX AMPLITUDE IS
C...CALCULATED.
```

```
C
                DO 7 I=1,K
                AMP(I)=SQRT(REAL(U(I))**2+AIMAG(U(I))**2)
                PH(I)=ATAN2(AIMAG(U(I)),REAL(U(I)))
                IF(PH(I).LT.0.0) PH(I)=PH(I)+2*PI
                PH(I)=PH(I)/PI
 7              CONTINUE
C
C...WRITE THE REAL PART, THE IMAGINARY PART, THE AMPLITUDE
C...AND THE PHASE TO FILE RESULT.  ONLY EVERY ZM TH STEP
C...IN THE Z DIRECTION AND EVERY KK TH STEP IN THE X
C...DIRECTION IS OUTPUT.
C
      I=(J/ZM)*ZM
      IF(I.NE.J) GOTO 2
           WRITE(1,300)(REAL(U(I)),AIMAG(U(I)),AMP(I)
     +                ,PH(I),I=1,K,KK)
 2         CONTINUE
      ENDFILE 1
 100  FORMAT(I4,1X,I4,4(1X,F12.6),1X,I6)
 125  FORMAT(I4,I4,I6)
 150  FORMAT(7E10.2)
 175  FORMAT(10F8.2)
 200  FORMAT(2HK=,I4,2X,2HN=,I5,2X,4HTAU=,F11.4,2X
     +,2HH=,F11.4,2X,5HSIGM=,F6.4,2X,5HFREQ=,F8.2,2X
     +,3HKL=,I5,2X,6HKSKIP=,I5)
 225  FORMAT(3HKK=,I4,3HZM=,I4)
 250  FORMAT(2X,I4,4X,I5,6X,F11.4,4X,F11.4,7X,F6.4,7X,F8.2,
     +5X,I5,8X,I5)
 275  FORMAT(3X,I4,3X,I4)
 300  FORMAT(2(2X,4E16.10))
 400  FORMAT(1X,I5)
      STOP
      END
C
C*********************************************************************
C
      SUBROUTINE UO(U,L)
C
C...THIS SUBROUTINE SETS THE INITIAL VALUES TO THE MATRIX U
C
      COMPLEX U(L)
      DO 1 I=1,L
      U(I)=CMPLX(1.0,0.0)
 1    CONTINUE
      RETURN
      END
C
C*********************************************************************
C
      SUBROUTINE FLUCT(F,J,K)
C
```

```
C...THIS SUBROUTINE CALCULATES THE FLUCTUATING PART OF THE
C...DIELECTRIC PERMITTIVITY AND THE F FUNCTION FOR THE BUBBLE
C...MODEL.  THE VERTICAL VARIATIONS ARE DETERMINED BY THE
C...PARABOLIC PROFILE MULTIPLIED BY THE WEIGHTING FUNCTION
C...G.  THE HORIZONTAL VARIATIONS ARE DETERMINED BY THE FILE
C...ELFL (STORED IN ARRAY ELX).
      COMMON/AAA/ELX(800)
      COMMON/BBB/FREQ,H,N,TAU,PI,XKI
      COMMON/CCC/AL,BET,EMAX,EZ,ZMAX,Z0,Z00
      DIMENSION F(600),DPZ(600),DPZ1(600)
      Z=TAU*(J-1)*XKI
      Z1=TAU*J*XKI
C
C...CALCULATE THE WEIGHTING FUNCTION FOR Z AND Z1. (G AND G1)
C
      IF(Z.LE.Z0) GOTO 1
      IF(Z.GT.Z00) GOTO 2
      G=1.0
      G1=1.0
      GO TO 3
 1    ARG=((Z-Z0)/AL)**2
      ARG1=((Z1-Z0)/AL)**2
      IF(ARG.GT.200.0) GOTO 4
      IF(ARG1.GT.200.0) GOTO 4
      G=EXP(-ARG)
      G1=EXP(-ARG1)
      GOTO 3
 2    ARG=((Z-Z00)/BET)**2
      ARG1=((Z1-Z00)/BET)**2
      IF(ARG.GT.200.0) GOTO 4
      IF(ARG1.GT.200.0) GOTO 4
      G=EXP(-ARG)
      G1=EXP(-ARG1)
      GOTO 3
 4    G=0.0
      G1=0.0
C
C...THE SCALE HEIGHT HH IS CALCULATED.
C
 3    HH=110.0E+03
C
C...THE ELECTRON DENSITY AT THE EDGE OF THE BUBBLE IS
C...CALCULATED FOR HEIGHTS Z AND Z1.
C
      E=EMAX*(1.0-((Z-ZMAX)/HH)**2)*G
      E1=EMAX*(1.0-((Z1-ZMAX)/HH)**2)*G1
      FACT=1.0
      FACT1=1.0
      IF(E.LE.0.0) FACT=0.0
      IF(E1.LE.0.0) FACT1=0.0
C
C...THE SQUARE OF THE PLASMA FREQUENCY AND THE FACTOR
```

```
C...(WP/W)**2 ARE CALCULATED FOR THE BUBBLE EDGE AT
C...HEIGHTS Z AND Z1.
C
      FP=80.6E-6*E/(FREQ**2)
      FP1=80.6E-6*E1/(FREQ**2)
C
C...THE FLUCTUATING PART OF THE DIELECTRIC PERMITTIVITY
C...AND THE F FUNCTION IS CALCULATED FOR EACH X STEP AT
C...HEIGHT Z1. EQUATION (32).
C
            DO 6 I=1,K
            DPZ(I)=FACT*FP*(ELX(I)/ELX(K)-1.0)
            DPZ1(I)=FACT1*FP1*(ELX(I)/ELX(K)-1.0)
            F(I)=(DPZ(I)+DPZ1(I))/2.0
 6          CONTINUE
      RETURN
      END
C
C*********************************************************************
C
      SUBROUTINE DCALC(AK,BK,CK,U,D,K)
C
C...THIS SUBROUTINE CALCULATES THE PRODUCT D=A*U. EQUATION
C...(54). NOTE THAT AK=BK IN THIS PROBLEM.
C
      COMPLEX AK(K),BK(K),CK(K),U(K),D(K)
      M=K-1
      DO 1 I=2,M
      D(I)=AK(I)*U(I-1)+CK(I)*U(I)+BK(I)*U(I+1)
 1    CONTINUE
      D(1)=CK(1)*U(1)+BK(1)*U(2)
      D(K)=AK(K)*U(K-1)+CK(K)*U(K)
      RETURN
      END
C
C*********************************************************************
C
      SUBROUTINE THOMAS(A,B,C,X,D,K)
      COMPLEX A(600),B(600),C(600),X(600),D(600)
     +,ALF(600),BT(600)
C
C...THIS SUBROUTINE SOLVES THE MATRIX EQUATION BX=AU
C...(WHICH IS THE SAME AS BX=D) FOR X.
C
C...CONSIDER THE SYSTEM:
C
C           (1) A(I)*X(I-1)+C(I)*X(I)+B(I)*X(I+1)=D(I)
C           (2) X(1)=-B(1)/C(1)*X(2)+D(1)/C(1)
C           (3) X(K)=-A(K)/C(K)*X(K-1)+D(K)/C(K)
C
C...BECAUSE X(0)=0 AND X(K+1)=0
C
```

```
C...ASSUME THE SOLUTION:
C              X(I)=ALF(I)*X(I+1)+BT(I+1)
C
C...WHERE:
C           (4) ALF(2)=-B(1)/C(1)          SEE EQ. (2) ABOVE
C           (5) BT(2)=D(1)/C(1)            SEE EQ. (2)  ABOVE
C           (6) ALF(I+1)=-B(I)/(A(I)*ALF(I)+C(I))
C           (7) BT(I+1)=(D(I)-A(I)*BT(I))/(A(I)*ALF(I)+C(I))
C
C...NOTE THAT A=B IN THIS PROBLEM BECAUSE OF SYMMETRY.
C
      ALF(2)=-B(1)/C(1)
      BT(2)=D(1)/C(1)
      M=K-1
            DO 1 I=2,M
            ALF(I+1)=-B(I)/(A(I)*ALF(I)+C(I))
            BT(I+1)=(D(I)-A(I)*BT(I))/(A(I)*ALF(I)+C(I))
 1          CCNTINUE
      X(K)=(D(K)-A(K)*BT(K))/(A(K)*ALF(K)+C(K))
            DO 2 I=1,M
            J=M-I+1
            X(J)=ALF(J+1)*X(J+1)+BT(J+1)
 2          CONTINUE
      RETURN
      END
```

```
      PROGRAM PULSE(INPUT,OUTPUT,ISPECT,TAPE20=ISPECT,IFREQ,
     +TAPE30=IFREQ)
C...THIS PROGRAM WILL CALCULATE AND PLOT THE FFT OF A PULSE
C...THE PARAMETERS OF THE PULSE THAT CAN BE
C...CHOOSEN ARE:
C                    1) FREQ, THE CARRIER FREQUENCY IN GHZ.
C                    2) TAU, THE PULSE DURATION IN NANOSEC.
C                    3) A, THE AMPLITUDE OF THE PULSES IN
C                       VOLTS.
C...THE PULSE  TIME FUNCTION IS ALSO PLOTTED.
C...THE MAX FREQUENCY COMPONENT SHOULD BE LESS THAN 60 GHZ
C...TO AVOID ALIASING.
C
      DIMENSION DATA(8200),XT(8200)
      COMPLEX C(8200)
      INTEGER PERIOD, TAU
C
C...SET UP THE PARAMETERS OF THE PULSE.
C
      READ(30,125) FREQ,TAU
      A=1.0
C
C...INITIALIZE THE ARRAYS, DATA (WHERE THE TIME FUNCTION AND
C...LATER THE FREQ SPECTRUM IS STORED). C THE COMPLEX REP.
C...OF DATA. AND, XT AN ARRAY USED TO PLOT AGAINST.
C
            DO 1 I=1,8200
            C(I)=CMPLX(0.00,0.00)
            DATA(I)=0.0
            XA=I
            XT(I)=(XA/(FREQ*8.0)-4096.0/(FREQ*8.0))
 1          CONTINUE
C
C...NOW THE PULSE  IS COMPUTED AND STORED IN DATA AND C.
C
      TAU1=TAU*(8*FREQ)
      J=(4096-TAU1/2)
      L=(4096+TAU1/2)
            DO 3 J1=J,L
            X=(J1-J)*(3.14)/4.0
            DATA(J1)=A*COS(X)
 3          CONTINUE
C
C...THE PULSE IS MULTIPLIED BY A GAUSSIAN FUNCTION SO THAT IT
C...DOESN'T BEGIN AND END ABRUPTLY.
C
      IM=0
      V=SQRT(((TAU/2)**2)/(2*4.61))
            DO 8 I=J,L
            X=((XT(I)-IM)**2)/(2*(V**2))
            DATA(I)=DATA(I)*EXP(-X)
 8          CONTINUE
```

```
          DO 10 I=1,8192
          Y1=DATA(I)
          Y2=0.0
          C(I)=CMPLX(Y1,Y2)
10        CONTINUE
C
C...FIND THE POWER IN THE TIME DOMAIN EXPRESSION OF THE
C...PULSE.
C
     PT=0.0
          DO 15 I=J,L
          PT=DATA(I)**2+PT
 15       CONTINUE
C
C...PLOT THE TIME FUNCTION.
C
     X1=TAU/2+30
     CALL USTART
     CALL UERASE
     CALL URESET
     CALL UDAREA(0.00,7.49,0.00,5.71)
     CALL USET("XBOTH")
     CALL USET("YBOTH")
     CALL UPSET("XLABEL","TIME IN NANOSEC.;")
     CALL UPSET("YLABEL","AMPLITUDE;")
     CALL USET("OWNSCALE")
     CALL UWINDO(-X1,X1,-1.0,1.0)
     CALL UPLOT1(XT,DATA,8192.0)
     CALL UPAUSE
C
C...NOW THE FFT SUBROUTINE IS CALLED, THE FREQ SPECTRUM WILL
C...BE RETURNED IN ARRAY C.
C
 9   NN=13
     CALL FFT(C,NN,.TRUE.)
C
C...NEXT THE FREQUENCY SPECTRUM IS PLOTTED.
C
     X1=FREQ/1024
          DO 4 I=1,4097
          DATA(I)=SQRT((REAL(C(I))**2)+(AIMAG(C(I))**2))
          XT(I)=(I-1)*X1
 4        CONTINUE
C
C...FIND THE POWER IN THE FREQUENCY DOMAIN EXPRESSION OF THE
C...PULSE AND ADJUST THE FREQUENCY SPECTRUM SO THAT
C...PARSEVAL'S THEOREM HOLDS.
C
     PF=0.0
          DO 14 I=1,4096
          DATA(I)=DATA(I)/1500.0
          PF=DATA(I)**2+PF
```

```
            DO 10 I=1,8192
            Y1=DATA(I)
            Y2=0.0
            C(I)=CMPLX(Y1,Y2)
10          CONTINUE
C
C...FIND THE POWER IN THE TIME DOMAIN EXPRESSION OF THE
C...PULSE.
C
      PT=0.0
            DO 15 I=J,L
            PT=DATA(I)**2+PT
 15         CONTINUE
C
C...PLOT THE TIME FUNCTION.
C
      X1=TAU/2+30
      CALL USTART
      CALL UERASE
      CALL URESET
      CALL UDAREA(0.00,7.49,0.00,5.71)
      CALL USET("XBOTH")
      CALL USET("YBOTH")
      CALL UPSET("XLABEL","TIME IN NANOSEC.;")
      CALL UPSET("YLABEL","AMPLITUDE;")
      CALL USET("OWNSCALE")
      CALL UWINDO(-X1,X1,-1.0,1.0)
      CALL UPLOT1(XT,DATA,8192.0)
      CALL UPAUSE
C
C...NOW THE FFT SUBROUTINE IS CALLED, THE FREQ SPECTRUM WILL
C...BE RETURNED IN ARRAY C.
C
 9    NN=13
      CALL FFT(C,NN,.TRUE.)
C
C...NEXT THE FREQUENCY SPECTRUM IS PLOTTED.
C
      X1=FREQ/1024
            DO 4 I=1,4097
            DATA(I)=SQRT((REAL(C(I))**2)+(AIMAG(C(I))**2))
            XT(I)=(I-1)*X1
 4          CONTINUE
C
C...FIND THE POWER IN THE FREQUENCY DOMAIN EXPRESSION OF THE
C...PULSE AND ADJUST THE FREQUENCY SPECTRUM SO THAT
C...PARSEVAL'S THEOREM HOLDS.
C
      PF=0.0
            DO 14 I=1,4096
            DATA(I)=DATA(I)/1500.0
            PF=DATA(I)**2+PF
```

```
 14        CONTINUE
      XF=SQRT(PT/PF)
      XF=XF/2.5066
           DO 13 I=1,4096
           DATA(I)=DATA(I)*XF
 13        CONTINUE
      X1=FREQ-.5
      X2=FREQ+.5
      CALL USTART
      CALL UERASE
      CALL URESET
      CALL UDAREA(0.00,7.49,0.00,5.71)
      CALL USET("XBOTH")
      CALL UPSET ("XLABEL","FREQUENCY IN GHZ;")
      CALL USET("YBOTH")
      CALL UPSET("YLABEL","AMPLITUDE;")
      CALL USET("OWNSCALE")
      CALL UWINDO(X1,X2,0.0,2.0)
      CALL UPLOT1(XT,DATA,4096.0)
      CALL UPAUSE
C
C...PLOT THE PHASE SPECTRUM.
C
           DO 6 I=1,4096
           DATA(I)=0.0
           Y1=AIMAG(C(I))
           Y2=REAL(C(I))
           Y=Y1**2+Y2**2
           IF(Y.EQ.0) GOTO 6
           DATA(I)=ATAN2(Y1,Y2)
  6        CONTINUE
      CALL UERASE
      CALL UDAREA(0.00,7.49,0.00,5.71)
      CALL UPSET("YLABEL","PHASE IN RADS;")
      CALL UWINDO(X1,X2,-4.0,4.0)
      CALL UPLOT1(XT,DATA,4096.0)
      CALL UPAUSE
C
C...PRINT REAL AND IMAGINARY PARTS OF THE FREQUENCY
C...SPECTRUM IN FILE ISPECT.
C
      PRINT(20,100) (XT(I),REAL(C(I)),AIMAG(C(I)),I=1,4097)
100   FORMAT(1X,2(F7.4,1X,F14.7,1X,F14.7,3X))
125   FORMAT(1X,F8.4,1X,I4)
      END
      SUBROUTINE FFT(X,M,FORWAR)
C*****************************************************************
C     FAST FOURIER TRANSFORM     VERSION 0.1     30 JULY 1980
C*****************************************************************
C
C...STANDARD FAST FOURIER TRANSFORM.  X IS BOTH THE INPUT
C...AND THE OUTPUT ARRAY CONTAINING 2**M COMPLEX DATA POINTS.
```

```
C...FORWAR=.TRUE. DOES FORWARD TRANSFORM, FORWAR=.FALSE.
C...DOES INVERSE TRANSFORM.
C
C*****************************************************************
      LOGICAL FORWAR
      COMPLEX X,U,W,T
      DIMENSION X(8200)
      N=2**M
C
C...BIT REVERSAL SECTION
C
      NV2=N/2
      NM1=N-1
      J=1
         DO 40 I=1,NM1
         IF (I.GE.J) GO TO 10
         T=X(J)
         X(J)=X(I)
         X(I)=T
   10    K=NV2
   20    IF (K.GE.J) GO TO 30
         J=J-K
         K=K/2
         GO TO 20
   30    J=J+K
   40    CONTINUE
C
C...MULTIPLICATION SECTION
C
      PIE=-3.141592653589
      IF (.NOT. FORWAR) PIE=-PIE
         DO 70 L=1,M
         LE=2**L
         LE1=LE/2
         ANGLE=PIE/FLOAT(LE1)
         U=(1.0,0.0)
         W=CMPLX(COS(ANGLE),SIN(ANGLE))
            DO 60 J=1,LE1
               DO 50 I=J,N,LE
               IP=I+LE1
               T=X(IP)*U
               X(IP)=X(I)-T
               X(I)=X(I)+T
   50          CONTINUE
            U=U*W
   60       CONTINUE
   70    CONTINUE
C
C...SCALING SECTION - INVERSE TRANSFORM ONLY
C
      IF (FORWAR) RETURN
      SCALE=1.0/FLOAT(N)
```

```
      DO 80 IJ=1,N
      X(IJ)=X(IJ)*SCALE
 80   CONTINUE
      RETURN
      END
```

```
      PROGRAM INTER(INPUT,OUTPUT,U9,UFREQ,TAPE10=U9,
     +TAPE20=UFREQ,IFREQ,TAPE30=IFREQ)
C
C...THIS PROGRAM INTERPOLATES BETWEEN THE NINE FREQUENCIES
C...THAT ARE THE OUTPUTS OF SHEET1.
C
      DIMENSION TA(4097),A(9),P(9),TP(4097),XT(4097)
      READ(30,200) FREQ
C
C...THE ARRAY WHICH WILL STORE THE INTERPOLATED FREQUENCY
C...OUTPUT IS INITIALIZED TO ZERO SO THAT ALL OF THE
C...FREQUENCIES OUTSIDE OF THE PULSE BANDWIDTH WILL BE ZERO.
C
           DO 1 I=1,4097
           TA(I)=0.0
           TP(I)=0.0
           XT(I)=(FREQ/1024.0)*(I-1)
 1         CONTINUE
C
C...READ THE INPUT DATA FROM FILE U9.
C
           DO 2 I=1,9
           READ(10,100) A(I),P(I)
 2         CONTINUE
      TA(753)=A(1)
      TA(821)=A(2)
      TA(889)=A(3)
      TA(957)=A(4)
      TA(1025)=A(5)
      TA(1093)=A(6)
      TA(1161)=A(7)
      TA(1229)=A(8)
      TA(1297)=A(9)
      TP(753)=P(1)
      TP(821)=P(2)
      TP(889)=P(3)
      TP(957)=P(4)
```

```
      TP(1025)=P(5)
      TP(1093)=P(6)
      TP(1161)=P(7)
      TP(1229)=P(8)
      TP(1297)=P(9)
      I1=753
C
C...THE LINEAR INTERPOLATION BEGINS.
C
            DO 3 I=753,1297
            I2=I1+68
            J=I-I1
            TA(I)=((TA(I2)-TA(I1))/(I2-I1))*J+TA(I1)
            TP(I)=((TP(I2)-TP(I1))/(I2-I1))*J+TP(I1)
            IF(I.EQ.I2) I1=I1+68
 3          CONTINUE
C
C...WRITE THE INTERPOLATED SHEET1 OUTPUT TO FILE UFREQ.
C
      PRINT(20,125) (XT(I),TA(I),TP(I),I=1,4097)
100   FORMAT(1X,F12.8,3X,F12.8)
125   FORMAT(1X,2(F7.4,1X,F14.7,1X,F14.7,3X))
200   FORMAT(1X,F8.4)
      STOP
      END




      PROGRAM MULT(INPUT,OUTPUT,UFREQ,ISPECT,OUTMUL,IFREQ,
     +TAPE10=UFREQ,TAPE20=ISPECT,TAPE30=OUTMUL,TAPE40=IFREQ)
C
C...THIS PROGRAM TAKES THE PULSE FREQUENCY SPECTRUM FROM
C...PROGRAM PULSE AND THE INTERPOLATED FREQUENCY OUTPUT FROM
C...PROGRAM INTER AND MULTIPLIES THEM TOGETHER TO PRODUCE
C...THE OUTPUT PULSE FREQUENCY SPECTRUM.
C
      DIMENSION UA(4097),UP(4097),FR(4097),FI(4097),XT(4097)
C
C...READ THE INPUT DATA FROM FILES ISPECT AND UFREQ.
C
      READ(10,125) (XT(I),UA(I),UP(I),I=1,4097)
      READ(20,125) (XT(I),FR(I),FI(I),I=1,4097)
      READ(40,150) FREQ,TAU
C
C...CHANGE THE MAGNITUDE AND PHASE PARTS OF THE INTERPOLATED
C...SPECTRUM INTO REAL AND IMAGINARY PARTS.
C
            DO 5 I=1,4097
            IF(UP(I).GE.2.0) UP(I)=UP(I)-2.0
            IF(UP(I).GE.2.0) UP(I)=UP(I)-2.0
```

```
          IF(UP(I).GE.2.0) UP(I)=UP(I)-2.0
          IF(UP(I).GE.2.0) UP(I)=UP(I)-2.0
5         CONTINUE
     PI=3.141592654
          DO 1 I=1,4097
          UP(I)=UP(I)*PI
          A=UA(I)
          B=UP(I)
          CALL PR(A,B,X,Y)
          UA(I)=X
          UP(I)=Y
 1        CONTINUE
C
C...NOW THE TWO FREQUENCY SPECTRUMS ARE MULTIPLIED TOGETHER.
C
          DO 2 I=1,4097
          X=(UA(I)*FR(I))-(UP(I)*FI(I))
          Y=(UP(I)*FR(I))+(UA(I)*FI(I))
          FR(I)=X
          FI(I)=Y
 2        CONTINUE
C
C...PLOT THE OUTPUT PULSE FREQUENCY SPECTRUM.
C
          DO 4 I=1,4097
          XT(I)=(FREQ/1024.0)*(I-1)
          UA(I)=SQRT(FR(I)**2+FI(I)**2)*.009
 4        CONTINUE
     X1=FREQ-.5
     X2=FREQ+.5
     CALL USTART
     CALL URESET
     CALL UERASE
     CALL UDAREA(0.00,7.49,0.00,5.71)
     CALL USET("XBOTH")
     CALL USET("YBOTH")
     CALL UPSET("XLABEL","FREQUENCY IN GHZ;")
     CALL UPSET("YLABEL","AMPLITUDE;")
     CALL USET("OWNSCALE")
     CALL UWINDO(X1,X2,0.0,2.0)
     CALL UPLOT1(XT,UA,4097.0)
     CALL UPAUSE
C
C...THE OUTPUT PULSE FREQUENCY SPECTRUM IS OUTPUT TO FILE
C...OUTMUL.
C
     PRINT(30,100) (XT(I),FR(I),FI(I),I=1,4097)
100  FORMAT(1X,3(F7.4,1X,F10.3,1X,F9.3,3X))
125  FORMAT(1X,2(F7.4,1X,F14.7,1X,F14.7,3X))
150  FORMAT(1X,F8.4,1X,I4)
     STOP
     END
```

```
C
C*****************************************************************
C
      SUBROUTINE PR(A,P,X,Y)
C
C...THIS SUBROUTINE CONVERTS COMPLEX NUMBERS IN THE POLAR
C...REPRESENTATION TO THE RECTANGULAR REPRESENTATION.
C
      PI=3.141592654
      Y1=ABS(PI/2.0-P)
      IF(Y1.LT..001) GOTO 1
      Y2=ABS(3.0*PI/2.0-P)
      IF(Y2.LT..001) GOTO 2
      TP=TAN(P)
      X=((A**2)/(1+TP**2))**.5
      Y=X*TP
      IF(P.GT.PI/2.0.AND.P.LT.3.0*PI/2.0) GOTO 4
      GOTO 3
1     X=0.0
      Y=A
      GOTO 3
2     X=0.0
      Y=-A
      GOTO 3
4     X=-X
      Y=-Y
3     RETURN
      END




      PROGRAM IFFT(INPUT,OUTPUT,OUTMUL,OUTTIM,TAPE10=OUTMUL,
     +TAPE20=OUTTIM,IFREQ,TAPE30=IFREQ)
C
C...THIS PROGRAM TAKES THE OUTPUT FREQUENCY SPECTRUM AND
C...PRODUCES THE TIME DOMAIN PULSE VIA THE INVERSE FFT.
C
      INTEGER TAU
      DIMENSION FR(8200),FI(8200)
      COMPLEX C(8200)
C
C...READ THE INPUT DATA FROM FILE OUTMUL.
C
      READ(10,100) (XT,FR(I),FI(I),I=1,4097)
      READ(30,150) FREQ,TAU
C
C
C...THE FREQUENCY SPECTRUM IS PERIODIC WITH A PERIOD OF 2 PI.
C...THE REAL PART OF THE SPECTRUM IS A EVEN FUNCTION, SO THE
C...MIRROR IMAGE IS CREATED FOR [PI,2PI]. THE IMAGINARY PART
```

```
C...OF THE SPECTRUM IS AN ODD FUNCTION, SO THE NEGATIVE
C...MIRROR IMAGE IS CREATED FOR [PI,2PI].
C
          DO 2 I=1,4095
          FR(4097+I)=FR(4097-I)
          FI(4097+I)=-FI(4097-I)
 2        CONTINUE
          DO 3 I=1,8192
          C(I)=CMPLX(FR(I),FI(I))
 3        CONTINUE
C
C...CALL THE INVERSE FFT TO GET THE OUTPUT PULSE IN
C...THE TIME DOMAIN.
C
     NN=13
     CALL FFT(C,NN,.FALSE.)
C
C...PLOT THE TIME FUNCTION
C
          DO 4 I=1,8192
          FR(I)=REAL(C(I))
          FI(I)=(I/(FREQ*8.0)-4097/(FREQ*8.0))
 4        CONTINUE
     Y=0.0
          DO 5 I=1,8192
          IF(FR(I).GT.Y) Y=FR(I)
 5        CONTINUE
     IF(Y.LE.1.0) GOTO 9
          DO 6 I=1,8192
          FR(I)=FR(I)/Y
 6        CONTINUE
 9        CONTINUE
          DO 15 I=1,4096
          TEMP=FR(I)
          FR(I)=FR(8193-I)
          FR(8193-I)=TEMP
 15       CONTINUE
     X1=TAU/2+30
     CALL PLOTS(0.,0.,99)
     CALL USTART
     CALL UERASE
     CALL UDAREA(0.00,7.49,0.00,5.71)
     CALL USET("XBOTH")
     CALL USET("YBOTH")
     CALL UPSET("XLABEL","TIME IN NANOSEC;")
     CALL UPSET("YLABEL","AMPLITUDE;")
     CALL USET("OWNSCALE")
     CALL UWINDO(-X1,X1,-1.0,1.0)
     CALL UPLOT1(FI,FR,8192.0)
     CALL UPAUSE
     CALL PLOT(0.,0.,999)
888  CONTINUE
```

```
C
C...OUTPUT THE TIME FUNCTION TO FILE OUTTIM.

      PRINT(20,125) (FI(I),FR(I),I=1,8192)
 100  FORMAT(1X,3(F7.4,1X,F10.3,1X,F9.3,3X))
 125  FORMAT(1X,4(F8.1,2X,F7.4,4X))
 150  FORMAT(1X,F8.4,1X,I4)
      STOP
      END
      SUBROUTINE FFT(X,M,FORWAR)
C*********************************************************************
C     FAST FOURIER TRANSFORM     VERSION 0.1     30 JULY 1980
C*********************************************************************
C
C...STANDARD FAST FOURIER TRANSFORM.  X IS BOTH THE INPUT
C...AND THE OUTPUT ARRAY CONTAINING 2**M COMPLEX DATA POINTS.
C...FORWAR=.TRUE. DOES FORWARD TRANSFORM, FORWAR=.FALSE. DOES
C...INVERSE TRANSFORM.
C
C*********************************************************************
      LOGICAL FORWAR
      COMPLEX X,U,W,T
      DIMENSION X(8200)
      N=2**M
C
C...BIT REVERSAL SECTION
C
      NV2=N/2
      NM1=N-1
      J=1
         DO 40 I=1,NM1
         IF (I.GE.J) GO TO 10
         T=X(J)
         X(J)=X(I)
         X(I)=T
   10    K=NV2
   20    IF (K.GE.J) GO TO 30
         J=J-K
         K=K/2
         GO TO 20
   30    J=J+K
   40    CONTINUE
C
C...MULTIPLICATION SECTION
C
      PIE=-3.141592653589
      IF (.NOT. FORWAR) PIE=-PIE
         DO 70 L=1,M
         LE=2**L
         LE1=LE/2
         ANGLE=PIE/FLOAT(LE1)
         U=(1.0,0.0)
```

```
      W=CMPLX(COS(ANGLE),SIN(ANGLE))
         DO 60 J=1,LE1
            DO 50 I=J,N,LE
            IP=I+LE1
            T=X(IP)*U
            X(IP)=X(I)-T
            X(I)=X(I)+T
50          CONTINUE
         U=U*W
60       CONTINUE
70    CONTINUE
C
C...SCALING SECTION - INVERSE TRANSFORM ONLY
C
      IF (FORWAR) RETURN
      SCALE=1.0/FLOAT(N)
         DO 80 IJ=1,N
         X(IJ)=X(IJ)*SCALE
80    CONTINUE
      RETURN
      END



      PROGRAM ENVEL(INPUT,OUTPUT,OUTTIM,OUTEN,TAPE10=OUTTIM,
     +TAPE20=OUTEN,OUTM,TAPE30=OUTM,IFREQ,TAPE40=IFREQ)
C
C...THIS PROGRAM FINDS THE ENVELOPE OF A PULSE STORED IN FILE
C...OUTTIM.  ALSO THE 1ST,2ND AND 3RD MOMENTS ARE CALCULATED
C...AS WELL AS THE MEAN SQUARE PULSE WIDTH.
C
      INTEGER TAU
      DIMENSION TO(8192),EN(501),X(501)
      READ(40,250) FREQ,TAU
      READ(40,350) CORR
C
C...READ THE INPUT DATA FROM FILE OUTTIM.
C
      READ(10,100) (Y,TO(I),I=1,8192)
      I3=500
      X3=I3
      I1=4089
           DO 6 I=4093,4101
           IF(TO(I).GT.TO(I1)) I1=I
6          CONTINUE
      J=I1-(I3*4)
      L=I1+(I3*4)
      X2=4097-I1
C
C...COMPUTE THE PULSE ENVELOPE.
C
```

```
            DO 3 I=1,I3
            EN(I)=0.0
 3          CONTINUE
      K=1
            DO 1 I=J,L,8
            X(K)=((K-1)-(X3/2)-(X2/8.0))/FREQ
            X(K)=X(K)-CORR
            EN(K)=(TO(I)**2)**.5
            K=K+1
 1          CONTINUE
      WRITE(30,325)  I1,J,X(251)
C
C...PLOT THE PULSE ENVELOPE.
C
      X1=TAU/2+30
      CALL PLOTS(0.,0.,99)
      CALL USTART
      CALL UERASE
      CALL UDAREA(0.00,7.49,0.00,5.71)
      CALL USET("XBOTH")
      CALL USET("YBOTH")
      CALL UPSET("XLABEL","TIME IN NANOSEC;")
      CALL UPSET("YLABEL","AMPLITUDE;")
      CALL USET("OWNSCALE")
      CALL UWINDO(-X1,X1,0.0,1.0)
      CALL UPLOT1(X,EN,X3)
      CALL UPAUSE
      CALL PLOT(0.,0.,999)
C
C ..CALCULATE THE FIRST FOUR MOMENTS.
C
      A=0.0
      B=0.0
      C=0.0
      D=0.0
            DO 2 I=1,I3
            A=(EN(I)**2)+A
            B=(EN(I)**2)*X(I)+B
            C=(EN(I)**2)*(X(I)**2)+C
            D=(EN(I)**2)*(X(I)**3)+D
 2          CONTINUE
      TM1=B/A
      TM2=C/A
      TM0=A
      TM3=D/A
      RMSP=TM2-(TM1**2)
      SK=TM3-(3*TM2*TM1)+(2*(TM1**3))
      SK=0.0
            DO 5 I=1,I3
            SK=(EN(I)**2)*((X(I)-TM1)**3)+SK
 5          CONTINUE
      SK=SK/((RMSP**.5)**3)
```

```
      SK=SK/A
C
C...OUTPUT THE TEMPORAL MOMENTS AND THE MEAN SQUARE PULSE
C...WIDTH TO FILE OUTM.
C
      WRITE(30,275) FREQ,TAU
      WRITE(30,125) TM0
      WRITE(30,150) TM1
      WRITE(30,175) TM2
      WRITE(30,200) RMSP
      WRITE(30,225) TM3
      WRITE(30,300) SK
C
C...OUTPUT THE PULSE ENVELOPE TO FILE OUTEN.
C
      WRITE(20,100) (X(I),EN(I),I=1,I3)
100   FORMAT(1X,4(F8.1,2X,F7.4,4X))
125   FORMAT(1X,F10.4,11H 0TH MOMENT)
150   FORMAT(1X,F10.4,11H 1ST MOMENT)
175   FORMAT(1X,F10.4,11H 2ND MOMENT)
200   FORMAT(1X,F10.4,21H MEAN SQ. PULSE WIDTH)
225   FORMAT(1X,F15.4,11H 3RD MOMENT)
250   FORMAT(1X,F8.4,1X,I4)
275   FORMAT(1X,F8.4,4H GHZ,3X,I4,8H NANOSEC)
300   FORMAT(1X,F10.4,9H SKEWNESS)
325   FORMAT(1X,3H***,3X,I7,3X,I9,3X,F8.2)
350   FORMAT(1X,F8.4)
      STOP
      END
```

Appendix B

The input parameters for the bubble model are stored in two files.

I. File ELFL

This file contains the $N(z,x)/N_0(z)$ information of Figure 2. The $N(z,x)/N_0(z)$ ratio remains constant for a given x over the entire range of z. However, $N_0(z)$ changes according to Equation (30).

II. File DA2

This file stores 17 input parameters. The input parameters are:

1. K=576, the number of steps in the x direction.
2. N=620, the number of steps in the z direction.
3. H=42.3729, the step size in meters in the x direction.
4. TAU=500, the step size in meters in the z direction.
5. SIGM=.5, a factor used in the parabolic equation solution.
6. FREQ=2500, 800, 500, the wave frequency in MHz.
7. KSKIP=0, the number of steps in the z direction recorded on file PASS. If KSKIP=0 then PASS is not read.
8. ZM=620, only every ZM steps in the z direction is stored on file RESULT.
9. KK=1, only every KK steps in the x direction is recorded on file RESULT.
10. KL=0, the number of steps in the z direction recorded in previous runs.
11. AL=1000, a factor used in the weighting function.
12. BET=2000, a factor used in the weighting function.
13. ZO=105.0E+03, a factor used in the weighting function.

14. ZOO=195.0E+03, a factor used in the weighting function.

15. EMAX=2.5E+05, the electron density in electrons/cm^3 at ZMAX. This parameter is named N_M in Equation (30).

16. EZ, not used, the electron density in electrons/cm^3 at z=0.

17. ZMAX=150.0E+03, the height in meters of the maximum in the vertical electron density profile. This parameter is named Z_M in Equation (30).

H_O, the scale height, is equal to 110 km in Program SHEET 1.

The output of SHEET 1 is stored in file RESULT.

Appendix C

54493 — Engr. Elec — 10-12 cent. — 7-28-82-db
Galley 1

Systematic Refraction Caused by Equatorial Plasma Bubbles Observed in Microwave Scintillations

S. Franke, J. Austen, A. W. Wernik*
and
C. H. Liu
Department of Electrical Engineering
University of Illinois
Urbana-Champaign, Illinois 61801

* On leave from the Space Research Center, Polish Academy of Sciences, Warsaw, Poland

Abstract. Equatorial ionospheric scintillation data at 1541.5 Mhz (L-band) and 3945.5 Mhz (C-band) showing time shifts of up to one second between similar fades of the two signals are presented. Simple model computations show that systematic refractive effects due to equatorial plasma bubbles in the particular propagation geometry may explain the observed data. Implications on equatorial ionospheric irregularities and scintillation theory are discussed.

Introduction

Electron density irregularities in the nighttime equatorial ionosphere are responsible for causing scintillations of transionospherically propagated radio waves with frequencies as high as the GHz range. The onset of scintillation has been shown to correspond to the passage of large depletions in ionization density through the propagation path (Yeh et al., 1979; Basu et al., 1980). The depletions have been named plasma bubbles (McClure et al., 1979) and are also associated with the plume structures seen by radar backscatter that extend vertically several hundred kilometers to the topside of the F layer (Woodman and LaHoz, 1976) and the occurrence of "range spread F" on ionograms obtained in the equatorial region (Aarons, 1982).

The scintillations produced by the irregularities associated with the plasma bubbles are often quite severe, producing saturated fluctuations at VHF and peak-to-peak fluctuations of up to 27 db at 1541.5 MHz (L-band) and 8 db at 3945.5 MHz (C-band) in the data analyzed for this report.

In this paper we report one aspect of the equatorial GHz scintillation phenomenon that has not been reported previously. Scintillation data observed simultaneously at L-band and C-band have been found to exhibit time displacements of up to ± one second between similar fades. Previous workers have observed similar time shifts in multifrequency observations of radio star scintillation at VHF frequencies at low elevation angles (Wild and Roberts, 1955) and the scintillation of pulsars caused by the tenuous interstellar plasma (Rickett and Lang, 1973). Shishov (1973) introduced a model of the interstellar medium having two scales of inhomogeneities, small, random scintillation producing irregularities and large, non-random ones which cause only refraction, to explain the observed frequency drift of interstellar scintillation features. Cole and Slee (1980) observed the time shift in wideband observations of the quasar 3C273 through the interplanetary plasma. Their interpretation is that the dispersion of the scintillation pattern is caused by diffraction refraction from sharp gradients in the interplanetary electron density. In both cases coherent refractive propagation effects are responsible for the observed time shift. In this report we shall attempt to explain our observations along similar lines with special consideration of the geometry and the propagation path.

Data Collection and Processing

The data were collected in late January and early February, 1981 at Ascension Island (7.95°S, 14.42°W, 30°S dip) which is located near the southern crest of the Appleton anomaly in F-region ionization. Signals from MARISAT (15°W) were received on 1541.5 MHz (L-band) and 3945.5 MHz (C-band). The satellite was viewed at an elevation of 81° and azimuth of 356°, so the propagation path was almost straight overhead and the propagation vector was within a few degrees of the magnetic meridian plane. The receiving antennas for both L and C-band were co-located prime focus feeds illuminating a single 3 meter diameter parabolic dish. The signal to noise ratio as determined from strip chart recordings is -16 db at L-band and -25 db at C-band, however, the L band signal is also "contaminated" with unpredictable level changes which are due to changing traffic loads on the C to L-band transponder. A typical signal level "jump" is 2 db. The analog AGC signal was recorded on tape and later digitized using 12 bits at a rate of 34.5 Hz (.029 seconds per sampling period) and stored on magnetic tape. The receiving and data collection system was carefully checked to make certain that the time displacement between the scintillation patterns is indeed due to irregular structure in the ionosphere.

The time displacement between the diffraction patterns at the two frequencies was measured by computing the delay time τ to the peak of the cross correlation between the fluctuations of the two signals. The accuracy of the cross-correlation estimate is dependent on the signal to noise ratio on both channels, and on the extent to which the noise is correlated between the two channels. In addition, the unpredictable signal level jumps in the L band data can cause incorrect results when the peak to peak L band scintillation level is low (< 2 db peak to peak). On the basis of empirical studies we have set a threshold scintillation index S_4 of .15 at L-band, above which the effects of noise and signal level jumps are not significant. A further constraint was added to insure that the measured time shifts correspond to similar structure in the two signals; only shifts which correspond to a normalized cross-correlation of greater than .5 have been considered.

Results and Discussion

We have studied four scintillation events which occurred in the time period between 2100 and 2400 UTC on January 27 and 30, 1981 (Ascension Island local time and UTC are the same.) The time displacement between similar fades at L-band and C-band is present to varying degrees in all of the data where a significant cross-correlation (> 5) is present. In Figure 1 we present examples of data which show the time shift along with the corresponding cross-correlation functions. The C-band signal is on top in both cases. A positive shift of the cross-correlation peak means that the C-band signal is leading the L-band signal.

The temporal variation of the time displacement is shown in Figure 2 for a 34 minute segment of data, where each point represents 30 seconds of scintillation. This data actually represents two patches of scintillation activity; a brief initial patch of intense scintillation which lasted for approximately six minutes followed approximately 2 minutes later by another patch which lasted for over 90 minutes. The section of data from 2227-2229 UTC which has been omitted corresponds to the lull in scintillation activity. The mean scintillation index for the entire segment shown in Figure 2 is approximately .1 for C-band and .5 for L-band, although the C-band index went as high as .18 and L-band as high as .85. The average peak cross-correlation is .63 and the average shift is .11 seconds with an rms shift of .35 seconds. There appears to be no obvious correlation between the observed shifts and the level of scintillation activity.

One of the interesting characteristics of the data became evident when we examined the time shift observed at the "edges" of the patches of scintillation; where we use "edge" to describe the first and last few minutes of a patch of scintillation. All four of the patches we studied had a well defined onset and decay of activity which is characterized by a sharp rise or fall of scintillation index except for the second patch shown in Figure 2 which decreased gradually. The time shift observed at all four of the onsets is positive (C-band leads L-band), while the shift observed in the last minutes of activity of the three events which ceased abruptly is negative. This data is summarized in Table 1 where the time of onset and decay is presented along with the approximate number of minutes that the time shift was positive (negative) at the beginning (end) of an event.

Table 1

Date	Time of Onset	# of minutes for positive shift	Time of Decay	# of minutes for negative shift	
1/27/81	2127:30	3.5	2249:30	2	
1/27/81	2221:30	2.5	2227:00	3	see Fig. 2
1/27/81	2230:00	6.5	gradual	–	
1/30/81	2214:30	4	2254:00	4	

This feature can be seen in Figure 2 where the beginning of the plot shows a positive shift which lasts for ~2.5 minutes and then goes negative corresponding to the onset and decay of the first patch of scintillation. The shift is again positive when the scintillation resumes again at 2229.

Since the drift of the nighttime plasma is from west to east, presumably, the onset and decay of a scintillation patch correspond to the east and west edges, respectively, of the scintillation producing structure in the ionosphere. In order to explain our observations of time shifts in terms of what is known about the equatorial plasma bubbles from radar and in situ measurements, in the next section we present a simple model of refraction on the vertically extended edges or "walls" of plasma bubbles.

We model the bubble wall as an extended sloping interface between the background plasma and the bubble depletion where the background refractive index is n and the refractive index inside the bubble is $n + \Delta n$. Let a ray at frequency f be incident on the wall at angle α with respect to the interface as shown in Fig. 3a. We represent the angular deviation of the ray from its initial direction by δ which is given by elementary optics:

$$\delta = \frac{1}{2} \frac{f_p^2}{f^2} \frac{\Delta N}{N} \cot \alpha \qquad (1)$$

where f_p is the background plasma frequency and $\Delta N/N$ is the fractional change in electron density across the interface. The direction of the deviation δ is such that, if the ray is incident on the interface from a region of higher refractive index (depleted region) the ray is bent toward the interface while the opposite is true for incidence from a region of lower refractive index.

The separation between two rays of different frequency at a vertical distance z from the point of refraction on the interface is given by:

$$d = z(\delta_1 - \delta_2) = \frac{z}{2} \frac{\Delta N}{N} f_p^2 \left(\frac{1}{f_1^2} - \frac{1}{f_2^2} \right) \cot \alpha \qquad (2)$$

If we assume that the bubble walls are field aligned with large north-south extent and move with a constant west to east velocity v(m/s), then the time shift τ(sec) between similar fades will be $\tau = \frac{d}{v}$. Assuming a background plasma frequency of 15 MHz, a height of refraction z = 350 km and west to east velocity v = 100 m/s, then for transmission at frequencies of 1.5 GHz and 4.0 GHz we have:

$$|\tau| = .150 \left| \frac{\Delta N}{N} \right| \cot \alpha \qquad (3)$$

Since the propagation path is almost vertical and approximately in the magnetic meridian plane, α may be taken as the approximate "tilt" of the wall with respect to vertical. The average magnitude of τ is approximately .3 seconds and since the mean fractional change in electron density must be between 0 and 1, the average tilt of the walls responsible for our observations must be in the range:

$$0 < \alpha \leq 27^\circ \qquad (4)$$

Recently, Tsunoda and Livingston (1981) reported from coordinated radar and in-situ measurements that all major bubbles observed were at least 90% depleted. If we take this value then, based on our observations, an average tilt would be $\alpha = 24^\circ$. The maximum shift observed is about 1 second which is possible if the refracting portion of the wall is within 8.5° of vertical. We note that although equation (1) was derived for an abrupt interface, it is also true for a gradual change in refractive index since Snell's Law holds for both situations.

So far we have shown that refraction at a bubble wall can produce time shifts of the same magnitude as those observed in this experiment. Next we consider the sign of the shift. In Figure 3b and 3c, we show the two possible configurations of the wall which will result in a high frequency ray preceding a lower frequency ray, assuming a west to east velocity. Note that the two configurations represent refraction on the east wall of a plasma bubble. A similar picture can be drawn for the case corresponding to the west wall of the bubble and in this case the lower frequency ray will precede the high frequency ray (for west to east drift velocity). Thus, whether the ray is incident on the bubble wall from inside or outside of the bubble, as long as the angle α is not too large, we observe the fluctuations on the higher frequency first when the rays are separated by refraction on the east wall and vice versa when the rays are separated by refraction on the west wall. In our data, the time shifts at the very beginning or end of a patch of scintillation activity was found to persist from 2-7 minutes. This corresponds to a horizontal displacement of 12 km to 42 km for the scintillation producing patch, assuming a velocity of 100 m/s. For the simple situation depicted in Figure 1 with $\alpha = 24^\circ$, this would correspond to a coherent vertical extent of the bubble wall in the range

$$27 \text{ km} < h < 94 \text{ km} \qquad (5)$$

This idealized model explains the shift observed at the first and last few minutes of a scintillation patch, however the shift is found to persist throughout the patch which can last for over an hour. If we consider a typical "real life" bubble as modelled by Tsunoda and Livingston (1981) from radar and in situ measurements, it is clear that the structure associated with a single patch of scintillation activity can consist of multiple vertically elongated wedgelike structures which extend from the bottomside to above the peak of the F-layer, with possible stronger structure beyond but near the west wall of the depletion. These wedges are often found to tilt to the west, so a nearly vertical ray may pass in and out of the depleted region several times undergoing refraction each time. Thus, refraction on the boundaries of plasma depletions can also explain the shift observed in the middle of a patch although we cannot predict the sign of the displacement.

From a slightly different viewpoint, we have studied the shifts observed in the middle of the scintillation patch by considering the simple deterministic model used by Wernik et al. (1980). Computations based on this model have revealed the importance of steep, vertically extended horizontal gradients, which are known to be present inside the bubbles during their early development, in producing enhanced GHz scintillation levels. We have taken a portion of the in situ profile shown in Figure 2 of Wernik et al. (1980) which corresponds to the segment between 2 and 5 km from the bubble center, and contains four distinct irregularities with sharp gradients. The parabolic equation has been solved for a wave propagating through a phase changing screen with phase variation proportional to the electron content fluctuations given by the chosen segment of in situ data. In Figure 4a the amplitude patterns at a distance of 350 km from the screen for L-band and C-band signals respectively. A characteristic pattern caused by the diffraction on the sharp edges of the two outermost irregularities (at approximately 3.75 and 4.6 km from the center of the bubble) is evident. Similar patterns have been observed in the Ascension Island scintillation data; in some cases, a distinct diffraction pattern is seen several times in succession within only a few minutes.

The cross-correlation between the amplitude at the two frequencies was computed separately for the sections between 2 and 3.6 km and 3.6 and 5.25 km from the center of the bubble and is shown in Figure 4b. In one case the cross-correlation maximum is at + 40 m and in the other it is at − 20 m. These displacements correspond to time shifts of + .4 and − 2 seconds if the diffracting structure moves with a velocity of 100 m/s.

Conclusions

In this note, we have presented equatorial ionospheric scintillation data observed at L-band (1541.5 MHz) and C-band (3945.5 MHz) along a near vertical propagation path in the magnetic meridian plane which showed time shifts of up to one second between similar fades of the two signals. Simple model computations have indicated that these time shifts may be caused by systematic propagation effects such as refraction in a medium with structures that are consistent with the vertically extended plasma bubbles. Indeed, the sign of the observed time shift and its duration during the first and the last few minutes of a scintillation patch have further enabled us to estimate that the walls of the plasma bubble may have coherent vertical dimensions of a few tens of kilometers.

This preliminary study of the time shift aspect of the equatorial GHz scintillation phenomenon has reconfirmed the close relationship between equatorial plasma bubbles and GHz scintillation. More importantly it indicates that systematic propagation effects in addition to random scattering play important roles in producing the observed scintillating signal signature.

Acknowledgment. The data presented were collected in a joint effort by AFGL, COMSAT Laboratories and University of Illinois. The digitized data tapes and test tape were provided by the AFGL group. We would like to thank J. A. Klobuchar and H. E. Whitney for helpful discussions and suggestions. Discussions with C. L. Rino are also acknowledged with pleasure. The work was supported in part by AFGL under contract F19628-78-C-0195.

Proceedings of the IEEE, 70, p 360, 1982.

Basu, A., J. P. McClure, S. Basu, W. B. Hanson, "Aarons' Coordinated Study of Equatorial Scintillation and In Situ and Radar Observations of the Nighttime F-Region Irregularities," *J. Geophys. Res.*, 85, p 5119, 1980.

Cole, T. W. and C. B. Slee, "Spectra of Interplanetary Scintillation," *Nature*, 285, p 93, 8 May 1980.

McClure, J. P., W. B. Hanson, and J. H. Hoffman, "Plasma Bubbles and Irregularities in the Equatorial Ionosphere," *J. Geophys. Res.*, 82, p 2650, 1979.

Rickett, B. J. and K. R. Lang, "Two-station Observations of the Interstellar Scintillation from Pulsars," *Astrophys. J.*, 185, p 945, 1973.

Shishov, V. I., "Effect of refraction on scintillation characteristics and average pulse shape of pulsars," *Astron. Zh.*, 50, p 941, 1973.

Tsunoda, R. T., [illegible] Livingston, "Equatorial Plasma Bubbles, Vertically Stimulated Wedges from the Bottomside F-Layer," Technical Report #DNA-TR-81-03, SRI International, 1 April 19[illegible].

Wernik, A. W., C. H. Liu, K. C. Yeh, "Model Computations of Radio Wave Scintillations Caused by Equatorial Ionospheric Bubbles," *Radio Sci.*, 15, p 559, 1980.

Wild, J. P. and J. A. Roberts, "The spectrum of radio star scintillations and the nature of irregularities in the ionosphere," *JATP*, 8, p 55, 1955.

Woodman, R. F. and C. LaHoz, "Radar Observations of F-Region Equatorial Irregularities," *J. Geophys. Res.*, 81, p 5447, 1976.

Yeh, K. C., H. Soicher, C. H. Liu, "Observations of Equatorial Ionospheric Bubbles by the Radio Propagation Method," *J. Geophys. Res.*, 84, p 6589, 1979.

Figure 1a, 1b (top, middle) — Segments of data (30 seconds each) showing the time shift between similar fades. C band is on top in both cases.

Figure 1c (bottom) — Normalized cross correlation functions for the data shown in Figs. 1a, 1b. A peak displaced to the right means the C band signal is leading the L-band signal.

Figure 2 — Temporal variation of the time shift of the cross correlation peak for a 34 minute segment of data. Each point represents 30 seconds of scintillation data.

Figure 3a (left) — Geometry of refraction at a vertically extended gradient with incidence angle α showing the deviation δ from the initial ray direction.

Figure 3b (center, right) — Two configurations of an ionization wall which will cause the high frequency (C-band) ray to precede the low frequency (L-band) ray when observed at a single station on the ground. The velocity is assumed to be from W-E.

Figure 4a (top) — The signal amplitude at a distance of 350 km from a phase changing screen which has phase fluctuations in proportion to electron density fluctuations given by in situ data. C-band is on top. The in situ data is a section of that reproduced in Figure 2 of Wernik et al. (1980).

Figure 4b (bottom) — Cross correlation functions for the first and last half of the data shown in Fig. 5a.

5545 Ionospheric Disturbances

SYSTEMATIC REFRACTION CAUSED BY EQUATORIAL PLASMA BUBBLES OBSERVED IN MICROWAVE SCINTILLATIONS

S. Franke, Department of Electrical Engineering, University of Illinois, Urbana-Champaign, Illinois, 61801; J. Austen, A. W. Wernik*, and C. H. Liu

Equatorial ionospheric scintillation data at 1541.5 MHz (L-band) and 945.5 MHz (C-band) showing time shifts of up to one second between similar sides of the two signals are presented. Simple model computations show that systematic refractive effects due to equatorial plasma bubbles in the particular propagation geometry may explain the observed data. Implications on equatorial ionospheric irregularities and scintillation theory are discussed. (Scintillation, refraction, plasma bubbles)

5560

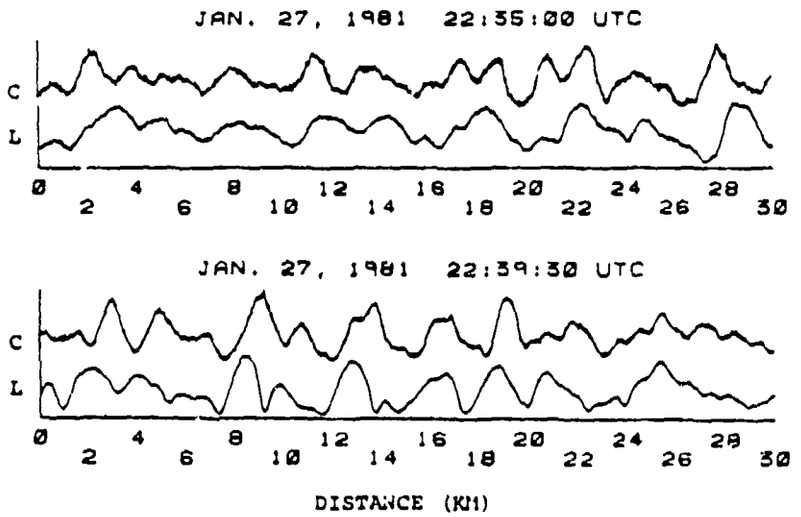
JAN. 27, 1981 22:55:00 UTC
C
L
0 2 4 6 8 10 12 14 16 18 20 22 24 26 28 30
JAN. 27, 1981 22:59:30 UTC
C
L
0 2 4 6 8 10 12 14 16 18 20 22 24 26 28 30
DISTANCE (KM)

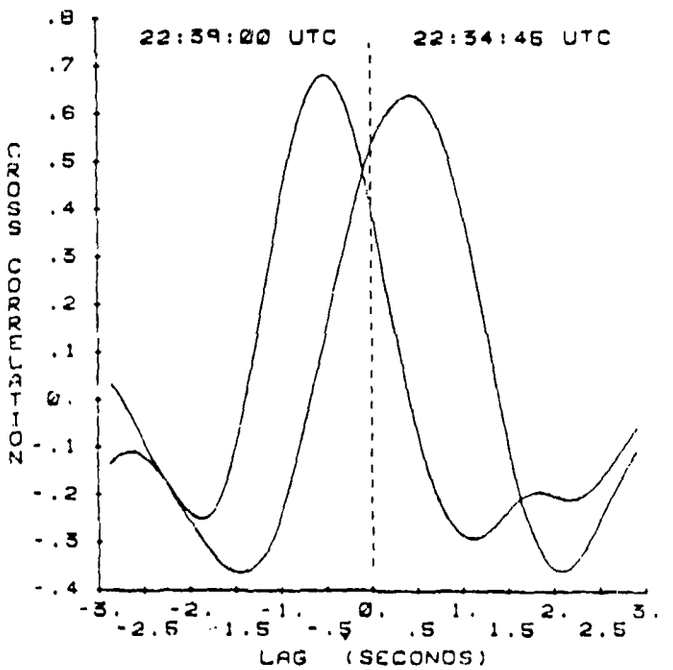
22:59:00 UTC
22:54:45 UTC
CROSS CORRELATION
.8
.7
.6
.5
.4
.3
.2
.1
0.
-.1
-.2
-.3
-.4
-3. -2. -1. 0. 1. 2. 3.
-2.5 -1.5 -.5 .5 1.5 2.5
LAG (SECONDS)

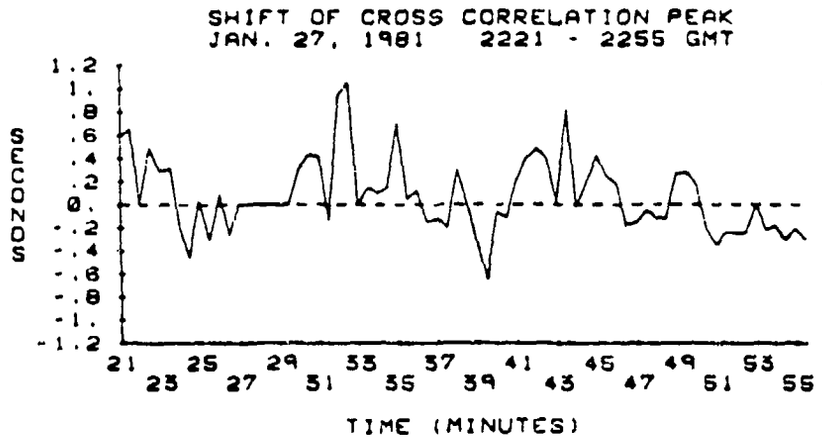
SHIFT OF CROSS CORRELATION PEAK
JAN. 27, 1981 2221 - 2255 GMT
SECONDS
1.2
1.
.8
.6
.4
.2
0.
-.2
-.4
-.6
-.8
-1.
-1.2
21 23 25 27 29 31 33 35 37 39 41 43 45 47 49 51 53 55
TIME (MINUTES)

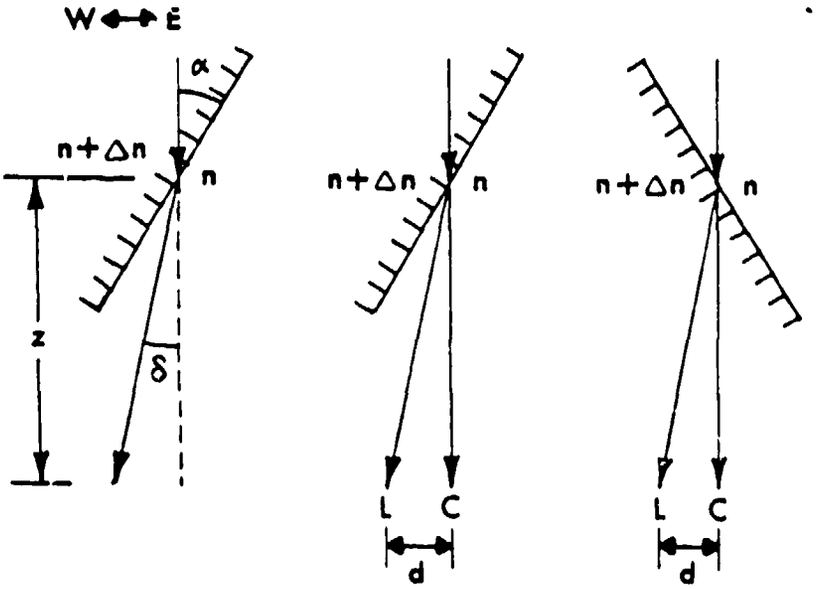
W
E
α
n+Δn
n
z
δ
n+Δn
n
L
C
d
n+Δn
n
L
C
d

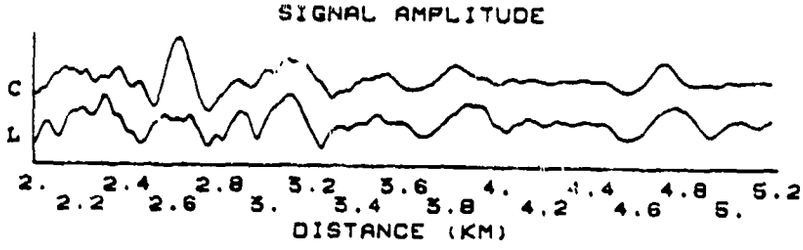
SIGNAL AMPLITUDE
C
L
2.
2.2
2.4
2.6
2.8
3.
3.2
3.4
3.6
3.8
4.
4.2
4.4
4.6
4.8
5.
5.2
DISTANCE (KM)

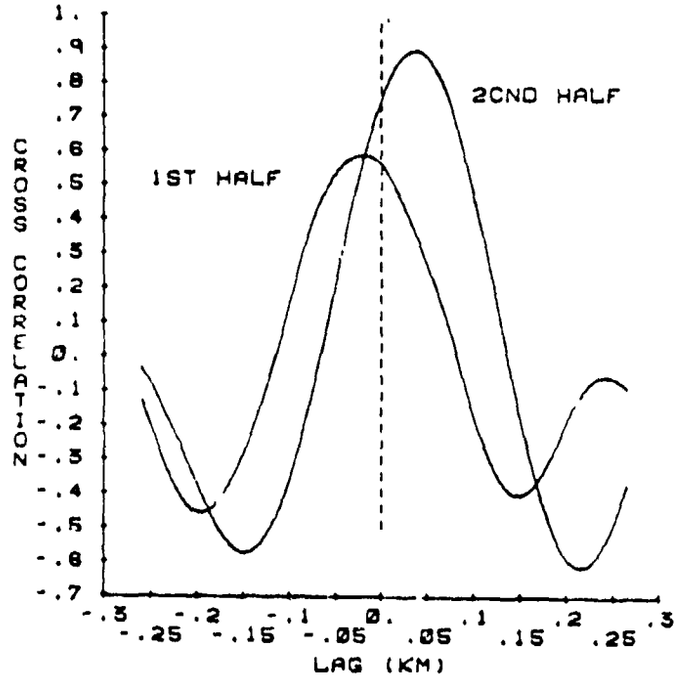
1.
.9
.8
.7
.6
.5
.4
.3
.2
.1
0.
-.1
-.2
-.3
-.4
-.5
-.6
-.7
CROSS CORRELATION
1ST HALF
2CND HALF
-.3
-.25
-.2
-.15
-.1
-.05
0.
.05
.1
.15
.2
.25
.3
LAG (KM)